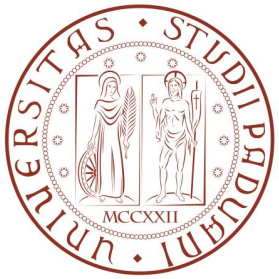

Università degli Studi di Padova

Dipartimento di Fisica e Astronomia "Galileo Galilei"

Master Degree in Astrophysics and Cosmology

Final Dissertation

The impact of bars on quenching galaxies across cosmic times: constraints from a nearby spatially resolved analysis

Supervisor:
Prof. Giulia Rodighiero

Co-Supervisor:
Dr. Laura Bisigello
Dr. Andrea Enia

Candidate:
Letizia Scaloni

Academic Year 2021-2022

To my family,
for always being by my side.

Abstract

Bars are a common feature of disk galaxies in the local Universe and it is also believed that they play a crucial role in the secular evolution of the host galaxies and in the dynamical (re)distribution of gas.
Therefore it is of significant relevance to further investigate the impact of these elongated structures on the quenching phase of galactic star formation and, actually, this is the aim of my thesis.
In particular, I perform a spatially resolved analysis on sub-galactic scales for a sample of nearby barred galaxies, exploiting photometric information over about 20 bands (from the UV to the far-IR) from the publicly available DustPedia database. This work is specifically focused on the spatially resolved relation between stellar mass and star formation rate (i.e. the Main Sequence, MS), in order to understand whether the presence of the bar affects the typical log-linear trend, at least in the inner regions.
Besides this, I take advantage of the IllustrisTNG50 simulation to extract an evolutionary prospectus of the galactic star formation (i.e. Star Formation History, SFH) and then of the spatially resolved MS relation for a sample of simulated disk galaxies that have undergone the onset of a bar structure. From these results, I finally try to discuss how the quenching of SFR due to the presence of bars can influence the decreasing evolutionary trend of the Universe's star formation rate density.
The main results of thesis work are: (i) the presence of an anti-correlation track in the spatially resolved Main Sequence of barred galaxies from DustPedia (which is also quite well reproduced by simulated galaxies from IllustrisTNG), (ii) the fact that the time evolution of the total SFR of simulated, more massive, barred galaxies goes as $\sim (1+z)^{2.03}$ in the redshift range $0 \leq z \leq 2$.

Contents

Chapter 1

Introduction

This first chapter is devoted to the presentation of the scenario in which this thesis is developed. In the context of extragalactic astronomy, this work is limited to the study of a few objects in the local Universe, exploiting both observational and simulated data.
As a first step I give an overview of the main properties of galaxies, which are the building blocks of the Universe. I describe their main structural components and how they are morphologically classified. I also trace the characteristics of the interstellar medium, emphasizing its fundamental role in the process of star formation and briefly mentioning the problem of dust extinction. In addition to this, I highlight the importance of the scaling relations that exist between the main structural parameters of galaxies, focusing in particular onto the so-called Star Forming Main Sequence, which will be the one investigated in this thesis work. The sample of objects that I am going to analyze is made of barred galaxies and in particular I am going to further investigate the influence that bars might have on the evolution of their host galaxies. Therefore, after this general presentation, I provide a description of the peculiarities of these type of galaxies. Finally I shortly point out also the importance of spatially resolved studies in the actual astrophysical research, since this will be precisely the approach to be used in the data analysis phase.

1.1 Characteristics and main components of galaxies

Galaxies are the fundamental building blocks of the visible Universe, they tend to realize a hierarchy of structures giving rise to the so-called Large Scale Structure of the Universe. This structure is well recognizable in our vicinity and up to scales of the order of hundreds of Mpc, it refers to the observable matter and light distribution. Galaxies organize into groups, clusters and superclusters that are separated by very large voids. As a result the Universe appears like a collection of huge voids and more dense regions, where the latter are produced by filaments of galaxies and gas, with superclusters constituting occasional nodes in that structure. This cellular and filamentous appearance of the Universe is such that it is also referred to as the *Cosmic Web*. However, looking at what happens on progressively larger scales (of the order of thousands of Mpc), one notices that the above structures are repeated in a rather regular manner so as to make the appearance of the Universe progressively more isotropic and homogeneous (evidences of this fact have been provided by the study of the radio-galaxies distribution and of the cosmic background radiation in X and in the microwaves). From this perspective, it is evident how galaxies are the fundamental elements that trace the visible Universe, so the study of their evolution is crucial for a better understanding of the Universe as a whole.
Galaxies are gravitationally bound systems consisting of stars, gas, dust and dark matter

(about which, to date, there is very limited knowledge, although cosmological observations indicate that it represents about the 80% of the gravitating matter in the Universe). These objects are separated from each other by distances of a few Mpc. Moreover galaxies are usually tens of kpc in size and they typically have a recurring structure, where the main components may be more or less prominent according to the various morphological types (see paragraph 1.1.1).
As a first step, it is important to distinguish the spheroidal or bulge component. It is located at the center of galaxies and it appears as a region of approximately spherical/elliptical shape in which the distribution of stars is more concentrated and therefore in which there is a greater luminosity. What is remarkable is that in elliptical galaxies this component dominates and it determines almost the whole galactic structure (gas and dust presence is scarse). Furthermore the bulge is important in lenticular galaxies too, while in the spiral ones it has a smaller size and it is grafted onto what is the dominant component here: the disk. In many lenticular and spiral galaxies it is also noticeable that, from the central spheroid, an elongated structure consisting of stars may develop: the bar. The prominence of the latter component becomes another key parameter in classifying the objects that host it. Finally, it is thought that many bulges may host a supermassive black hole, which cannot be directly observed because it is an extremely compact object with a so intense gravitational field that neither matter nor electromagnetic radiation escapes.
As mentioned above, another relevant component is the disk, which is more diffuse and extended than the bulge. It is preponderant in spiral galaxies but can also be clearly identified in lenticular ones and it contains both stars and gas/dust. This component appears as a flattened structure that is supported by the rotation of the galaxy itself. Due to the presence of an angular momentum, the primordial gas that has not collapsed into stars during the galactic halo formation phase (another galactic component) redistributes into this flattened structure along the horizontal plane of symmetry of the galaxy. Then another stellar population starts to form from this remnant primordial gas (partially reprocessed and enriched in metals) and these stars are the ones that typically characterize the so-called thick disk of galaxies, which may not always be present. The considerable thickness of this disk is probably due to the merging effect and interactions between galaxies, which can enable a component of the stellar orbital motion to develop in the direction that is orthogonal to the disk plane. In addition to an eventual thick disk, there may also be a thin disk, where the residual (cooler) gas and dust concentrate and thus where the rate of star formation is very high. Indeed this is the region where the youngest and bluest stars are found. In the case of spiral galaxies these young stars appear to thicken in correspondence to the spiral arms. This thin disk of gas (mostly made of neutral, molecular or ionized hydrogen) and dust can extend as much as, or even much more than, the stellar body so it is often used as the main tracer to determine the mass distribution of galaxies that host it.
Finally, the galactic halo is a roughly spherical component that surrounds the internal galactic body and that can have an extension that goes even beyond the main visible component of galaxies. The halo consists of very old stars (mainly organized in globular clusters), gas but also dark matter. Observations suggest that the halo is the first galactic environment to form, but there is still no unambiguous explanation for the characteristics found in halo stars. Actually apart from being the oldest and very metallic-poor (they are extreme population II stars), these stars also show chaotic orbital motions with strong radial components and almost no angular momentum. Two justifications can be given for this fact:

1. galactic formation occurs by *monolithic collapse*, in this case halo stars are formed during the gravitational collapse phase of the primordial gas, which has strong radial motions;

2. galaxy formation occurs by *hierarchical clustering* through merging, according to this second scenario, halo stars, after their formation, undergo a considerable dynamical

turbulence (as a consequence of gravitational collisions and mergers between galaxies), which makes their orbital motions disordered.
Currently this is the most widely accepted model for galaxy formation.

So far I have discussed the main structural components of galaxies in which stars, gas and dust are essentially organized, but the presence of dark matter, which has already been mentioned in the case of the galactic halo, is really important too. Dark matter constitutes one of the main cosmological enigmas that are studied nowadays, its existence is proven by gravitational effects that occur in baryonic matter interaction. An experimental evidence for the presence of a dark matter halo in galaxies is obtained from the study of the rotation curve of these objects. What happens is that the rotational velocity of the regions outside the galaxy bulge shows a flat trend which is in contrast with what the Keplerian law would predict. Indeed, according to the latter, as one probes regions farther and farther away from the galactic center, beyond the extent of the stellar body, there should be a velocity decrease that goes as $r^{-1/2}$, because at some point the stellar mass distribution decays. From the fact that instead the observed velocity turns out to remain constant, it has been deduced that the mass distribution of galaxies does not decrease as one would have expected. In other words, as one moves away toward the outer regions, the baryonic matter density decays but this decrease is balanced by an increase in dark matter density, which helps to maintain an overall gravitating matter density such that the rotation curve turns out to be flat.

1.1.1 Morphological classification

Understanding physical mechanisms that are involved in the processes of galaxy formation and evolution is certainly one of the main research topics in astrophysics. However, as a first step, it is necessary to analyze the morphological properties that characterize the visual and structural aspect of these objects. Actually galaxy morphology is correlated with many of their global properties, such as: stellar populations, angular momentum, star formation rate, gas and dust content. As a consequence it is important to be able to divide galaxies into well-defined groups making use of specific criteria and this leads to the development of various classification systems.
The reference scheme for almost all the traditional visual morphological classifications is provided by the Hubble classification. Hubble distinguishes galaxies into four families:

- elliptical galaxies (E)
- normal (S0) and barred (SB0) lenticular galaxies
- normal (S) and barred (SB) spiral galaxies
- irregular galaxies (Irr)

He schematically places them in the so-called tuning fork diagram (see Figure 1.1). It can be seen that the tuning fork structure is occupied by ellipticals, lenticulars and spirals, while irregular galaxies are placed in a separate position with respect to the rest of the diagram.
Objects belonging to the class of elliptical galaxies manifest a rather regular symmetry. They have a circular/elliptical and compact shape, with a stellar density that uniformly decreases going towards the external regions. Their structure shows little evidence of gas and dust and it basically coincides only with the spheroidal component (bulge). The objects of this family are also identified through their apparent flattening (i.e. ellipticity). Indeed they are depicted by the letter E followed by a number n (En), with n=0, 1, ..., 7, which is defined as $n = 10(1 - b/a)$, where b and a are respectively the minor and major axes of the ellipse describing the apparent shape of these galaxies. Therefore, elliptical galaxies are divided into eight groups: from E0, those with a circular apparent shape, to E7, which are the most

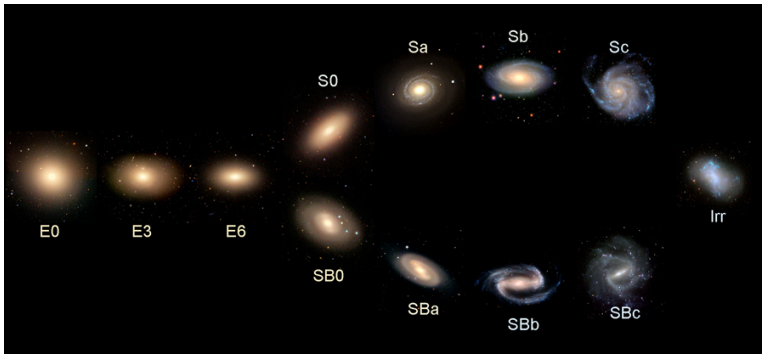

Figure 1.1: Schematic representation of the tuning fork diagram that characterizes the morphological classification of Edwin Hubble.

flattened. Anyway it has to be noticed that what has been said so far is related just to the apparent shape of galaxies. When the intrinsic three-dimensional shape of these objects is considered, they can be divided into oblate, prolate or triaxial ellipsoids. Members of this class typically show a very bright nuclear region and a luminosity profile that then gradually decreases until it completely drops out. Elliptical galaxies are mostly made of old stars (population II stars): metal-poor and rather cool (they are usually red giants) stars, they give a reddish aspect to their host galaxies.
Lenticular galaxies get this name because their apparent shape resembles that of a biconvex lens, if they are observed in an edge-on configuration. Unlike ellipticals, that have a single spheroidal component, lenticular galaxies show two bright components: a central bulge and a disk. This family of objects is divided into two sub-classes: normal lenticulars (S0) and barred lenticulars (SB0). Each of them can be further split into three groups: $S0_1$, $S0_2$, $S0_3$ and $SB0_1$, $SB0_2$, $SB0_3$ depending, respectively, on the prominence either of the dust in the disk or of the bar. These objects have no spiral structures in the disk and they usually contain low amounts of interstellar medium, so they are characterized by a low star formation activity, hence they consist mainly of old stars.
Galaxies belonging to the class of normal spirals are characterized by a structure showing a flat and relatively thin disk, within which spiral arms, wrapped around a bright central region, can be revealed. The bulge contains old stars of population II, while in the thin disk, characterized by the presence of large clouds of gas and dust and thus by a high rate of star formation, there are young and hot stars (of population I) that provide a bluer aspect to the regions outside the bulge. For this class of objects, the main discriminating criteria are three: the prominence of the nuclear region with respect to the disk, the spiral arms winding around the nucleus and the disk resolution in stars, dust nodes and HII regions. Based on these three pieces of information, one can arbitrarily recognize as many morphological sub-groups within the class. Each of these groups is indicated by placing another letter next to the S, which can be a, b, or c, according to the following criteria:

- Sa $\rightarrow$ very big bulge and very tightly wrapped arms lacking resolved structures.
- Sb $\rightarrow$ moderately extended bulge and mildly wrapped arms, without many resolved structures.
- Sc $\rightarrow$ little-extended bulge and broad arms that are not attached to the nucleus, with highly resolved condensations of stars, HII regions, and dust nodes.

Barred spiral galaxies are quite similar to normal spirals, except for the presence of an elongated structure that is grafted onto the core and from the ends of which the arms appear to depart: the bar. The morphological classification of barred spiral galaxies follows the same

criteria as the ones used for normal spirals, discussed above. The main difference lies in the acronym that is used to denote them, which is SB instead of S. Hubble refers to unbarred galaxies as "normal" because he observes more galaxies without bar than barred objects, but what has been found later is that, in the local Universe, about 70% of spiral galaxies are barred. Bars are mostly made up of old stars, that emit mainly in the red, so these elongated structures turn out to be well recognizable at infrared wavelengths. This is why in the blue-sensitive images available to Hubble the bar is usually absent or barely visible, so to make him believe barred galaxies were only a small percentage and not the majority.
Finally, galaxies that do not belong to any of the previous families are classified by Hubble as irregular. These objects show basically no symmetry and no clear structural component. They appear as a variable number of resolved stars arising from the dark sky background. The irregular aspect of these galaxies can be caused by various phenomena, such as mergers between galaxies or deformations due to the gravitational effects generated by the presence of a close more massive galaxy. These irregular galaxies are typically very rich in gas and dust, as a consequence they mainly host young stars (population I), which make these objects predominantly blue. The Magellanic Clouds are perfect examples of irregular galaxies. Hubble distinguishes two types of irregulars: type I irregular galaxies (Irr I), which are strongly star-resolved objects, and type II irregular galaxies (Irr II), which show very chaotic and disturbed structures with dark spots and filaments due to dust. This Hubble classification system has undergone a clear evolution over time: it has been reformulated several times with the aim of making it objective and reproducible as much as possible, but this remains the cornerstone structure for the morphological classification of galaxies.

1.1.2 ISM and star formation

The interstellar space is by no means empty, in fact it contains rarefied gas, dust grains, electrons in relativistic motion, protons and other atomic nuclei. These various forms of matter are not uniformly distributed, they show significant differences in density, temperature and ionization state. We refer to them by the generic term "interstellar medium" or, more briefly, ISM. One of the main differences between galaxies belonging to the various morphological classes identified by Hubble concerns precisely the amount and distribution of their ISM, so an accurate study of this component is a fundamental prerequisite in order to have a comprehensive view of galaxy characteristics. The interstellar medium is made of raw materials from which new stars are formed, and when stars die, the material that is produced (enriched by stellar nucleosynthesis) is poured back into the interstellar medium and often through violent mechanisms (e.g. supernova explosions). The cycle of events that describes the process of star formation plays a key role in the evolution of galaxies. It starts from clouds of molecular gas and dust and it ends with the release of the products of stellar evolution into the ISM and with the subsequent birth of new stars from this processed and metal-enriched material. This process is sketched in Figure 1.2.
Going deeper in the ISM composition, it can be seen that it is dominated by hydrogen, but it also has smaller amounts of helium and minor traces of metals (this term is typically used to indicate elements heavier than helium). The most abundant heavy elements are: carbon, nitrogen, oxygen and silicon. They, including helium, are the products of thermonuclear reactions that are triggered within stars (p-p chain, CNO cycle) and, as mentioned above, they enrich the interstellar medium during the final evolutionary stages of a star, when major events of mass-loss from the envelope occur through strong stellar winds, eventually leading to a supernova explosion (for the most massive stars). The elements that characterize the composition of the ISM can be either singularly detected or found in the form of radicals (e.g. OH^-, CN^-) or molecules (e.g. H_2, CO, CS, NH_3, HCN, H_2O).
Moreover about 99% of the interstellar medium is in gaseous form, while the remaining 1% is in solid state, condensed into dust grains. The gaseous component of the ISM can be either an

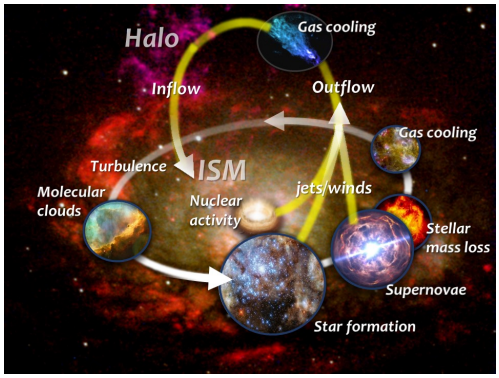

Figure 1.2: Representation of the cycle of events that characterize the galactic components interactions.

almost completely ionized plasma (HII regions), or it can be in neutral atomic form (mainly clouds of HI, also referred to as Cold Neutral Medium), or in molecular form (clouds of H_2, with small amounts of other molecules). In particular it is from these molecular clouds of H_2 that stars originate. Actually these are the densest and coldest regions of the interstellar medium and when they are crossed by shock waves produced by other events (such as supernova explosions), particularly overdense regions are generated, at least locally, and this can trigger a gravitational collapse of the cloud, even though its stability is usually ensured by pressure due to the thermal motion of the gas particles, by rotation, and sometimes also by the presence of magnetic fields. When gravitational collapse occurs[1], a series of subsequent steps lead to star formation: cloud fragmentation, protostar core formation, disk accretion made of material from the surrounding envelope, dissociation of H_2 molecule and ionization of H and He as the temperature increases, and finally formation of the pre-main sequence star (once hydrostatic equilibrium is restored).
For what concerns the dust component [Galliano et al., 2018], it is produced by stellar evolution processes. Indeed these particles are formed in the atmospheres of the most evolved stars or in supernova remnants and then they are ejected into the interstellar medium. The size of dust grains varies within a range of 0.3-300nm and are mainly composed of heavy elements, in particular they have a core that can be made of Si, C, O, Mg, Fe and polycyclic aromatic hydrocarbons (PAHs) and that is wrapped into an organic and/or icy mantle (that is why traces of H_2O can be revealed in the ISM).
Although dust is just a small component of the ISM, it has a remarkable importance in multiple physical processes occurring in the interstellar medium itself. For example dust grains act as catalysts in numerous chemical reactions, including the formation of molecules (particularly H_2), indeed they absorb the energy produced by collisions between atoms (located on the surface of these dust grains) that form the molecule in question. Besides that, dust particles are also able to absorb energy both from the collisions between themselves and gas particles and from the incident UV radiation, in this way they heat up and consequently re-emit in the IR keeping the surrounding medium cold. This process is of particular relevance in preventing the photo-dissociation of molecules in the ISM. From an observational point of view, the fact that the dust absorbs part of the incident radiation and re-emits it in the IR constitutes an important effect in revealing its presence in galaxies. Actually it can be seen that the luminous flux from the stellar continuum is extremely modified (reduced) in the wavelength range from the UV to the near-infrared. This happens because of the absorption by dust grains that are present in the interstellar medium interposed between the

[1]To determine which conditions are able to trigger the gravitational collapse of a molecular cloud, one can use the Jeans criterion. The latter gives the critical value for the mass of the cloud beyond which gravity exceeds the thermal pressure of the gas, allowing the collapse to start.

observer and the light source. In addition to that, a significant dust-emission in the mid and far-infrared region is detected, so this is a further and fundamental evidence of its presence. The following table (Table 1.1) shows the main characteristics of the various components of the interstellar medium discussed so far.

Component	Density (cm^{-3})	Temperature (K)	Tracer
HI clouds	5-20	50-100	HI 21cm line
H_2 clouds	>100	10-20	CO (rotational trans.), HCN
HII regions	10-10^3	10^4	Hα, [OII], [NII], radio continuum
dust		20-200	IR emission, extinction

Table 1.1: Properties of the main components of the interstellar medium: the density is expressed in terms of hydrogen atoms per cm^3 for the HI and H_2 clouds, while the electron density is given for the HII regions (here the gas is in the plasma phase); the temperature is in Kelvin degrees; finally it is indicated which tracer is used to study each component.

Dust extinction

As already mentioned earlier, the presence of dust in a galaxy can be revealed by means of two main observational effects: its emission in the MIR-FIR and the depletion of the specific intensity of a light source in the UV-NIR region of the spectrum. The combination of these two effects greatly alters the observed spectrum of the sources, as a consequence the information obtained from a single observation (e.g. in optical regime) is usually incomplete, since dust mostly hides the presence of young or forming stars (which emit mainly in the UV) by absorbing or scattering most of their emitted radiation. It is important to note that the modification of the luminous flux of a source in the UV-NIR, which is called interstellar extinction, is produced by absorption but also by photon scattering due to dust grains. Actually the latter can either absorb (and then heat up and emit in IR) or deflect (scatter) photons in directions other than that of the observer's line of sight. The term *extinction* refers precisely to the amount of light that is lost (and thus that cannot be detected by the observer) along a single line of sight due to absorption or scattering of photons emitted by the source. This definition, however, should not be confused with that of *attenuation*, by which we denote the total amount of light that is lost within a certain number of lines of sight. This includes not only the contribution of absorption and scattering along each individual line of sight, but also the contribution given by the possible variations in column density (or optical depth) along different lines of sight and the one produced by unobscured stars. In general, the effects of the complex geometry of stars and dust distribution in galaxies are included in the attenuation term [Salim and Narayanan, 2020].
To overcome the problem of altering the information that is obtained from observations affected by the presence of dust, it is necessary to combine the results of several observations (of the same source) made in different photometric bands. For example, one can observe the same galaxy both in optical and in IR, millimeter, etc., in this way the information about regions of star formation, which is lost due to dust absorption in optical, can be recovered through observations at higher wavelengths (where the dust typically re-emit). In this way one can trace the history and formation processes of the galaxy. An important feature of dust extinction is that it is not constant at all wavelengths, actually this effect is greater at shorter wavelengths.

1.2 Scaling Relations

The existence of correlations between the main structural parameters of galaxies has been known since the second half of the last century, when the first large data sets with measurements made on local galaxies began to become available. Indeed numerous trends have been empirically found between important integrated physical properties of galaxies, such as: stellar mass, luminosity, rotational velocity, star formation rate, amount of gas, etc.. To date, such scaling relations between the various galactic parameters are recognized as a fundamental tool for the study of galaxy formation and evolution. Moreover, with the increasing capabilities of the observational instruments that were built in recent years, it has been possible to greatly expand the database of measurements related to local galaxies but also the ones related to objects at higher redshifts. Thanks to these surveys and to future observational projects, there will be very important information and increasingly tight constraints on how the mass of galaxies is assembled, then we will be able to better figure out the co-evolution of galactic components, the role of dark matter and dark energy, the frequency of merger/interaction events between galaxies, and the feedback effects caused by supernovae explosions or violent emissions from active galactic nuclei (AGN). According to the current model of galaxy formation and evolution, galaxies appear to build their stellar mass by secular processes and, in particular, through the accretion of cold molecular gas. Actually stars are formed in dense H_2 clouds by the interaction of different physical mechanisms (as mentioned in paragraph 1.1.2). Despite its complexity, this interaction results in two important log-linear relations between different physical quantities: one between the stellar mass ($M_\star$) and the global star formation rate (SFR) and the other between the gas mass surface density ($\Sigma_{\rm gas}$) and the SFR surface density ($\Sigma_{\rm SFR}$). These are respectively the Star Forming Main Sequence (SFMS) and the Kennicutt-Schmidt (KS) relations. The former is the one that will be investigated in this thesis work, specifically for a sample of local barred spiral galaxies.

1.2.1 Star Forming Main Sequence

During the secular evolution of a galaxy, its SFR appears to be regulated by a simple empirical log-linear relation: the more massive the galaxy is, the higher its SFR is. Many literature works hint that this law, usually named as Main Sequence (MS) of star-forming galaxies (SFG) is valid, with a relatively constant scatter of $\sigma \sim 0.2$–0.3dex, for local as well as for distant galaxies (up to $z \sim 6$), for a wide range of stellar masses and considering different SFR tracers [Brinchmann et al., 2004, Noeske et al., 2007, Elbaz et al., 2007, Rodighiero et al., 2014]. In Figure 1.3 I report the Main Sequence relation computed at $z \sim 2$ using different SFR indicators [Rodighiero et al., 2014].

Galaxies appear to oscillate around the MS relation as a results of multiple events of central compaction of gas followed by inside-out gas depletion, thus related with the flows of cold gas in galaxies [Tacchella et al., 2016]. The existence of such a relation provides a powerful tool to study formation and evolution of galaxies. In particular it represents a practical way to disentangle between star-forming and quenched galaxies, setting a suitable upper-limit below which a galaxy of a given stellar mass can be considered as quenched. Actually a galaxy is dubbed as "active", by the point of view of the star formation, when its SFR is consistent or higher than that predicted by the Main Sequence. On the contrary a galaxy is considered as "passive" (or equivalently "quiescent") when the SFR is very low or absent. This is a common case among red elliptical galaxies. Furthermore a special class of SFG is represented by the so-called "starbursts", which show SFRs even ten times, or higher than that of the MS. These rare objects represent a very peculiar and still not well known phase of galaxy evolution. Their role in the star formation rate density (SFRD), at the peak of the cosmic star formation ($z \sim 2$) [Madau and Dickinson, 2014], turns out to be secondary [Rodighiero et al., 2011].

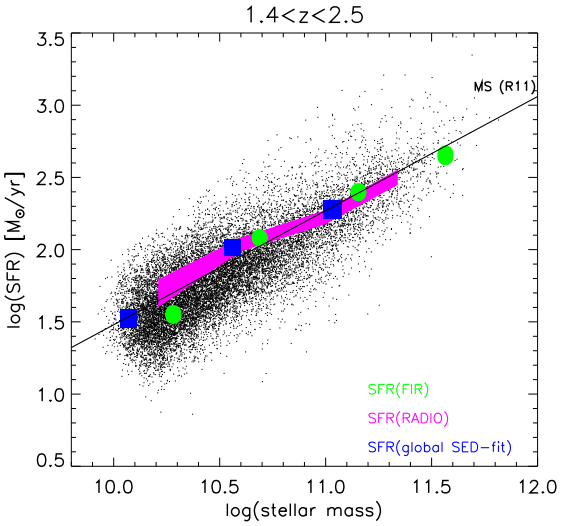

Figure 1.3: Main Sequence of star-forming galaxies as obtained at z∼2, using different SFR indicators. Black points represent SFR values computed using the UV emission as SFR indicator [Rodighiero et al., 2014]. The magenta region corresponds to SFRs from stacked radio data [Karim et al., 2011]. The green data points refer to stacked far-IR based SFRs (*sBzK* selection). The blue squares result from a global SED fit applied to *sBzK* selected data [Magdis et al., 2012]. This plot is taken from [Rodighiero et al., 2014].

More recently, thanks to the advent of the Integral Field Spectroscopy (IFS[2]), it has been discovered that the integrated MS relation takes place also locally, at sub-galactic scales (of size comparable to molecular clouds). This implies that the star formation process is originated by physical mechanisms acting on such sub-kpc scales [Cano-Díaz et al., 2016]. There is a general consensus on the existence of such a spatially resolved MS (observed only at low redshift), but its slope, intercept and dispersion are subjected to significant variations among different literature works, according to the selected sample of galaxies, SFR tracers, dust extinction correction and fitting procedure [Abdurro'uf and Akiyama, 2017, Popesso et al., 2019, Enia et al., 2020]. See Figure 1.4.
For example, exploiting pixel-by-pixel Spectral Energy Distribution (SED) fitting procedure, it has been found that the spatially resolved MS (on kpc-scales) in a sample of local galaxies can have slopes varying from 0.3 to 0.99 depending on the considered range of $\Sigma_\star$ [Abdurro'uf and Akiyama, 2017]. Moreover their scatter variations can be ascribed to different large scale properties (i.e. morphology, existence of a bar).The former aspect reminds to the typical bending of the observed integrated MS relation [Popesso et al., 2019, Popesso et al., 2022]. Indeed it is known that the relation exhibits a curvature towards the high stellar masses, this is true at all redshifts and it also evolves with Universe age. In particular it has been argued that the progressive MS bending as a function of the Universe age is caused by the lower availability of cold gas in halos entering the hot accretion phase, in addition to black hole feedback.
To get spatially resolved properties, a SED fitting procedure is typically used, since it allows to go deeper than spectroscopic measurements based on Hα emission lines. Indeed, the latter

[2]Integral Field Spectroscopy: It is a spectroscopic technique that allows us to obtain spectra from a very large two-dimensional field, which is divided into a rectangular (or square) array of points; from each of them a spectrum is obtained with a standard spectroscope. A variety of methods can be used to do this, for example: optical fibers (that carry light from the focal plane to the slit of a spectroscope) or an array of lenses (which redirect light in different directions according to a grid organized in such a way that the spectra relative to each lens do not overlap). The advantages of this spectroscopic technique are: high sensitivity and high spatial resolution.

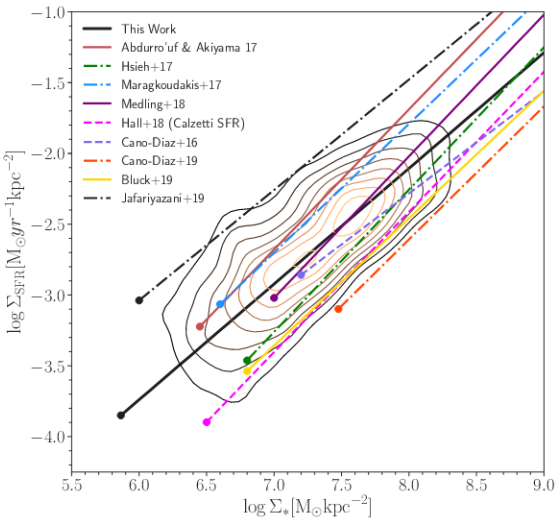

Figure 1.4: Comparison of spatially resolved MS relations from different literature works. Each relation, converted to a Chabrier IMF [Chabrier, 2003] and re-scaled to z = 0, starts from the sensitivity limit reported in the respective parent study. [Enia et al., 2020]

depend critically on corrections for dust extinction, so combining measurements in the UV with those in the IR one can minimize the uncertainties related to the presence of dust since, by doing so, one can reveal both direct emission from the galactic stellar component and the one initially absorbed by dust and then re-emitted in the IR.
In this context the treatment of SFR indicators has a relevant impact, because they are referred to different physical mechanisms and are sensitive to timescales that can vary from a few - 5 or 10 Myr for H_α emission lines and UV bands - to hundreds of Myr - for 24µm, IR and FIR bands [Calzetti et al., 2010]. Consequently, the effects of different observational tracers have to be taken into account especially when comparing observational results with theoretical works.
The basic goal is to identify emission that probes newly or recently formed stars, while avoiding as much as possible contributions from evolved stellar populations.

UV emission

This kind of emission is due to young, massive ($M \simeq 10 M_\odot$) stars and it encompasses a wavelength range between 1250Å-2500Å. The advantages of using this emission are that: it is directly correlated to the emission of population I stars and it can be applied to a large number of active galaxies over a wide range of redshifts. The disadvantage of this indicator is its great sensitivity to dust absorption and metal content in galaxies. Because of this, the SFR can be determined only after correcting for the absorption effects. It is obtained from the specific UV luminosity using a direct correlation of the kind (see Equation 2.1):
$SFR_{UV} = K_{UV} \cdot L_{UV,\nu}$.

IR emission

Infrared radiation can be decomposed into two contributions, the first in the NIR (near-infrared) regime and the second in the FIR (far-infrared) regime. The light in the NIR is mainly dominated by stars with Sun-like mass, so in order to use it as a tracer there is a need for calibration to take place assuming a given IMF, SFH[3], spatial diffusion, and dust optical depth. The most widely used calibration is that of [Kennicutt, 1998b] (see Equation 2.2),

[3]Star Formation History.

which assumes an optically thick and compact interstellar dust component that is heated by the emission of young stars for a period of ∼100Myr. The FIR radiation is dominated mainly by the re-emission from dust of UV light at wavelengths between 10-300µm, so this emission is highly sensitive to the young stellar population and this makes it an excellent tracer for SFR. An additional advantage of this indicator is that in the far-infrared regime absorption from dust can be neglected.

1.3 Galaxy color bimodality and quenching mechanisms

Galaxies and their evolution across cosmic time have always intrigued astronomers. In the first half of the last century, Edwin Hubble classified galaxies according to their morphology (as more deeply explained in paragraph 1.1.1, [Hubble, 1926]). Two major classes can be distinguished: Early Type Galaxies (ETGs) – characterized by elliptical shapes – and Late Type Galaxies (LTGs) – which include galaxies that are made of a central bulge and spiral arms. Moreover the Morphology-Density (MD) relation (found later, [Dressler, 1980]) states that ETGs and LTGs are not uniformly distributed in space. Namely, the former dominates high density environments, while LTGs are mainly found in low density fields. The fact that galaxy properties depend on the environment was solidly confirmed in the last decades due to the observations provided by wide galaxy surveys such as the Sloan Digital Sky Survey (SDSS), Cosmic Evolution Survey (COSMOS) and the PRIsm MUlti-Object Survey (PRIMUS).
The color–magnitude diagram (CMD) is the reference diagnostic tool for understanding the physical properties of stars and stellar populations of any age, chemical composition, and size going from simple star clusters to galaxies and, in recent times, the galaxy content of clusters of galaxies. A bimodal distribution is pointed out in galaxy color [Baldry et al., 2004, Pandey and Sarkar, 2020] and star formation rate as well [Trussler et al., 2020]. As a result galaxies can be divided into three different populations: (1) Blue Cloud (BC) – filled mainly by late-type (90% LTG vs 10% ETG), blue, star forming galaxies; (2) Red Sequence (RS) – dominated by early-type (70% ETG vs 30% LTG), red galaxies with low (if any) star formation; and (3) an intermediate region called the Green Valley (GV) – containing galaxies partially quenched with intermediate morphologies. An example of CMD for a sample of galaxies in the Coma Supercluster (CS) is shown in Figure 1.5, [Gavazzi et al., 2010].
Additionally, an important caveat is that red LTGs are expected at all masses, whereas blue ETGs are mainly found at the low mass end. Finally, the galaxy's path and the related timescales through the GV depends critically on the quenching mechanism [Woo et al., 2017]. Actually astronomers now think that disk galaxies form first, then they evolve into elliptical galaxies through galaxy mergers that are able to destroy their flat structure. As a consequence, the green valley is considered as a region where blue cloud star-forming galaxies are aging into red sequence quenched galaxies.
For what has been said so far, it can be grasped that there are two main populations of galaxies: those that are actively forming new stars (blue cloud) and those that, on the other hand, are in a quiescent phase (red sequence). At this point one can ask how a galaxy can stop forming stars and become quiescent: will it be because it runs out of its gas reservoirs from which stars originate? If so, what could be the cause of gas depletion in the ISM?
According to the current model of the formation and evolution of galaxies, they continue to increase their gas content through the gravitational collapse of gas filaments, present in the so-called Cosmic Web. Actually, the star formation in galaxies is usually fueled by the inflow of hot gas from the circumgalactic medium, which is then cooled via internal interactions in the so-called "cold-disk", which eventually gravitationally collapses to form new stars [Cimatti et al., 2019]. How is it that, at some point, this gas can no longer reach the galaxies thus causing them to quench?
These are the questions at the center of the main debates in the field of modern astrophysics,

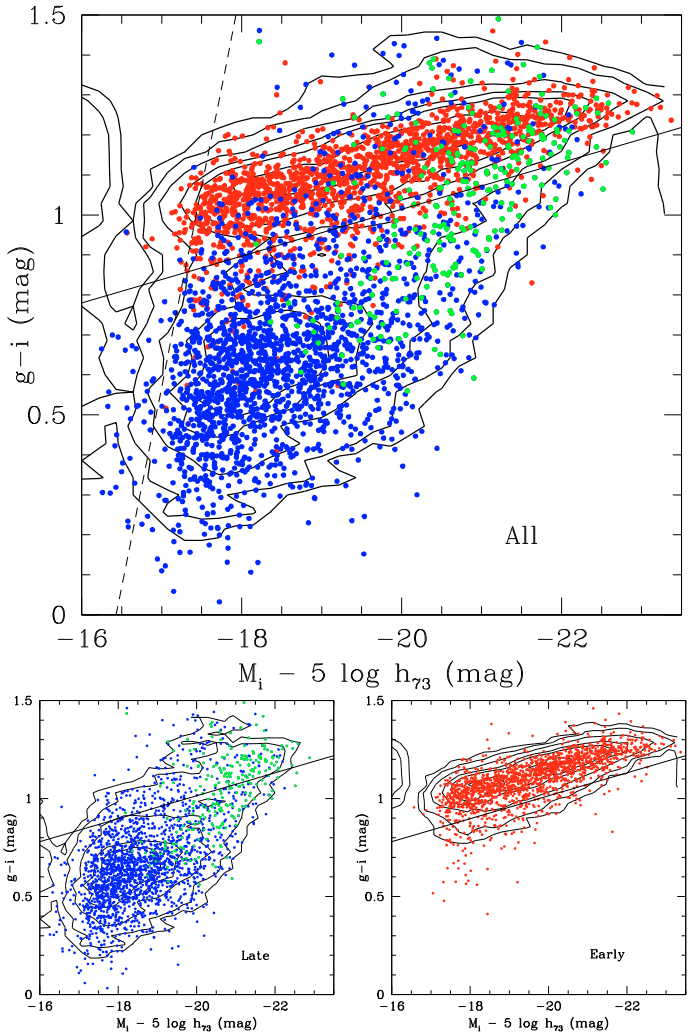

Figure 1.5: g-i color versus i-band absolute magnitude relation of all galaxies in the CS. They are color-coded according to Hubble type: red = early-type galaxies; blue = disk galaxies; green = bulge galaxies. The top panel shows all galaxies, the bottom left one presents late-type objects, finally the bottom right plot has only early type galaxies. Contours of equal density are given. The continuum line represents the empirical separation between the red-sequence and the remaining galaxies. [Gavazzi et al., 2010]

and there are various hypotheses that have been formulated regarding them.
Quenching may be related to stopping the hot gas from cooling, thus the galaxy will passively evolve and form only a negligible amount of stars from the current reservoir of cold gas available in the disk ([Ilbert et al., 2015], "slow quenching"). When in dense environments, a second way to quench star formation is to remove all the galaxy's gas component (including the cold disk) in a short time-scale ([Tacchella et al., 2022], "rapid-quenching"). On the other hand, in isolated galaxies, star formation quenching is mostly driven by internal processes. For example, low-mass galaxies may be subjected to the effects of the so-called supernova feedback. Indeed the final fate of massive stars that populate galaxies can be a supernova explosion, which causes the gas to be swept out of the galaxy and confined into a surrounding halo, so that the production of new stars stops. However, this hypothesis could be contradicted by the fact that the gas confined outside the galaxy should still, at some point, gravitationally fall back on the galaxy itself, and then cool down to become the fuel for star-forming activity again. Another possible explanation lies in the effects produced

by Active Galatic Nuclei (AGN) feedback. Indeed, supermassive black holes, hosted by the cores of many galaxies, can periodically produce particularly energetic outflows in the form of stellar winds, which can both sweep away the gas and heat it up, thus preventing the onset of further star formation (for which cold, dense gaseous environments are necessary) [Bongiorno et al., 2016]. Star formation depends also on gravitational instabilities; in fact, it may be halted by a transition from a stellar disk to a spheroid ([Martig et al., 2009], "morphological quenching"). Another aspect to be taken into consideration is the fact that also bars in spiral galaxies may have a fundamental role in the galaxy evolution. It may either drive gas inflows, which enhance central star formation, or quench the SF activity due to the gas funneling towards the galaxy outskirts ("bar-driven evolution"). Peculiarities of barred galaxies and their star formation activity evolution are better addressed in Section 1.4.
In the local Universe most of the galaxies live in groups/clusters. Even before crossing the virial radius, infalling galaxies can stop accreting new gas ([Balogh et al., 2000], "starvation"). In addition, infalling galaxies can lose gas, stars and even dark matter via gravitational tides ([Read et al., 2006], "tidal mass loss"). Within the virial radius, the hot gas in the intracluster medium (ICM) exerts pressure on galaxies moving within the cluster and may remove gas via Ram Pressure Stripping [Abadi et al., 1999]. For these reasons clusters provide a suitable environment for both direct and indirect galaxy interactions, especially in its core. Direct encounters may lead to galaxy mergers and cause a starburst event over a short time scale, thus quickly exhausting a galaxy's gas supply, whereas repeated indirect encounters may leave interacting galaxies with disturbed morphologies.
As can be easily perceived, the balance between internal and environmental processes driving galaxy evolution results in a complex non-linearity. The main mechanism driving galaxy evolution and the related time scales are yet not fully understood. Different works indicate that the main quenching mechanism is dependent on galaxy and host halo mass. Therefore, the complex relation between galaxy properties and quenching mechanisms translates into a variety of paths for galaxy's transition from the BC to RS. Consequently, it is not straightforward to reliably define the BC, GV and RS regions, for which different works adopt different parameter spaces and methodologies. Although it is known that galaxy morphology correlates with their properties, it is still necessary to further investigate the transition from BC to RS from a morphological perspective. Furthermore, recent works discuss the possibility of dense environments inducing morphological variations prior to SFR changes [Martig et al., 2009, Kelkar et al., 2019].

1.4 Barred galaxies

As already briefly anticipated, in this thesis work I focus on studying a sample of barred galaxies, so I devote this section to collecting the main characteristics of this type of galaxies. Galactic bars are central, rectangular-shaped and non-axisymmetric internal morphological structures present in at least a 25% to 30% of all galaxies and in around half to more than two thirds of all spiral galaxies, considering galaxies with $M_\star \gtrsim 10^{9\div10}$ $M_\odot$ in the local Universe [Aguerri et al., 2009, Nair and Abraham, 2010, Masters et al., 2011]. Bars form mainly when the stellar orbits of disk galaxies deviate from a circular path due to instabilities. Detecting these structures is of fundamental importance if one wants to trace back the formation and evolution of galaxies where bars are able to transport materials (not only gas) between the disk and the bulge of the host galaxies.
Actually the formation of the bar structure throughout the Universe depends on many aspects, i.e. environment, colour, mass and gas content of a galaxy, and it is involved in the evolutionary processes. It is believed that bars play a crucial role in the secular evolution of disk galaxies since they are able to redistribute gas, stars, dark matter and even angular momentum of the host galaxies [Athanassoula and Misiriotis, 2002, Debattista et al., 2006].

Bars can efficiently funnel gas towards both the central and the outer regions of galaxies eventually triggering starbursts events or fueling active galactic nuclei. As a consequence the presence of a bar can be responsible for the onset of a fast star formation rate phase [Spinoso et al., 2016], accompanied with a subsequent rapid consumption of gas in galaxies [Fraser-McKelvie et al., 2020]. Hence the star formation of a galaxy may have different evolutionary paths according to the presence or absence of the bar structure and so it could provide crucial information about galaxy assembly history.
Bars form quickly once a dynamically cool disk has settled, then the formation of bars in disk galaxies is a tracer of the dynamical maturity of the population. Understanding the time of their formation and how they affect their host galaxies is key to get a comprehensive view of the late-stage evolution of galaxies themselves. However, tracing the actual time of bar formation is a challenging task. Different studies have attempted to time when bar forms for various samples galaxies and using different approaches. In quite recent studies, some observers have been able to determine the fraction of barred galaxies up to $z = 1$ and they obtained that this tends to decline at increasing redshift. In particular it was found that the barred galaxies fraction goes from 65% at $z \sim 0.2$ to 20% at $z \sim 0.8$ [Melvin et al., 2014], so this can suggest a possible epoch at which the bars observed in nearby galaxies have formed. Such a result draws a picture in which the evolution of massive disk galaxies begins to be affected by slow (secular) internal processes at $z \sim 1$.
Therefore incidence of bars in disks decreases from the local Universe up to $z \sim 1$, then across the redshift range $0.5 < z < 2$ the fraction of bars is about 10-11% and it does not significantly evolve. See Figure 1.6.

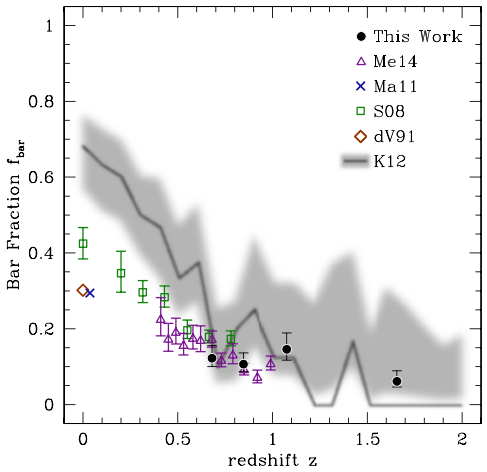

Figure 1.6: Fraction of disk galaxies that have a strong bar feature versus redshift, according to what various literature works have found. [Simmons et al., 2014]

Observational studies in local Universe have pointed out that bars are typically found in massive, red and gas poor galaxies rather than in blue, star forming and gas rich ones [Gavazzi, 2015, Consolandi et al., 2017]. Resolved observations have also found that gas distribution show holes in disk regions, presumably where the bar has swept up and funnelled gas both inwards and outwards within its region of influence. All of these effects are generally more prominent in strongly-barred galaxies and they can favour the onset of a premature quenching phase. For example, a sample of strongly barred galaxies in the SDSS turns out to have a star formation activity that is, on average, lower than that of unbarred galaxies [Kim et al., 2017]. Also more recently, from a sample of Galaxy Zoo DECaLS[4] disk galaxies, it has been confirmed the fact that strong bar fraction is typically higher in quiescent galaxies

[4]Dark Energy Camera Legacy Survey.

than in star forming ones, while the weak bar fraction is similar [Géron et al., 2021]. Moreover, strong bars facilitate the quenching process in star forming galaxies, since lower gas masses and shorter depletion timescales are present in these galaxies compared to unbarred objects. Additionally a recent statistical study of the Star Formation Efficiency (SFE) on galactic structures found out that the ratio of SFE in bars to that in the disk is systematically lower than unity, which means that the star formation in the bar is systematically suppressed [Maeda et al., 2022]. Another hint of lower SFE in bar environment comes from a spatially resolved analysis performed on a sample of PHANGS[5] galaxies, for which the relation between the surface densities of stellar mass, molecular gas mass and star formation rate has been studied [Pessa et al., 2022].
However, the long-term relevance of bar driven quenching is still unclear, because bar structures could be dissolved through time. Besides that, there are also other mechanisms, as already said, that can quench star formation in galaxies. [George et al., 2019].
Although what has been discussed so far clearly suggests to us that bars are responsible for the different evolutionary pathways that can occur in the galaxies that host them (or at least turn out to be involved in that), it is not obvious that the observed differences between barred and unbarred galaxies are not driven by some other related factors. For example, the stellar mass of a barred galaxy turns out to be correlated with bar length, but also with star formation activity and color. Another thing that is not entirely obvious is why barred galaxies turn out to be redder; this fact could be due either to the presence of older stellar populations (thus to a lower star formation rate, as mentioned above) or richer in metals, or to the contribution of reddening from dust, or a combination of these factors. Thus, bar effects cannot yet be fully determined, it is important to be able to distinguish them from other external influences. To quantify the effects of bars on their host galaxies, it is necessary to compare barred galaxies with unbarred galaxies, once the mass and morphology of these objects are fixed.
Thanks to the MaNGA[6] survey, detailed spectroscopic information has been added, making it possible to use advanced population synthesis techniques to study not only current stellar populations but also the entire star formation history of galaxies. Consequently, many recent studies are devoted to reconstructing the SFH of galaxy samples in order to expand the knowledge of galaxy formation and evolution and to discover possible correlations with the presence of the bar.
In this regard, I mention a recent study [Fraser-McKelvie et al., 2020] in which the stellar populations and SFHs of a sample of 245 barred galaxies selected from the MaNGA survey were determined and compared with an appropriately chosen sample of unbarred galaxies. Once the sample of barred galaxies has been selected and once their main characteristics has been known, the sample of their unbarred counterparts is chosen so that they have the stellar mass and the main morphological parameters as close as possible to those of the previously selected barred galaxies. In this way, since these parameters (mass and morphology) are in good agreement between the two samples, any observed trends between the properties of the barred and unbarred galaxies certainly are not due to external influences provoked by possible differences in stellar mass or morphology. What was found, comparing the SFH trends of these two samples of galaxies, is that the barred ones show a peak in star formation activity at earlier epochs than what it is observed for the unbarred galaxies, moreover the latter show a second, less intense peak within the last 0.1Gyr and this is consistent with the current star formation activity of these objects (see Figure 1.7). The fact that in barred galaxies the SFR peak occurs at more remote cosmic epochs means that these objects build their present mass earlier than unbarred galaxies do. From this one concludes that the older, metal-rich stellar population found in barred galaxies were formed in a remote star-forming episode, followed

[5]Physics at High Angular resolution in Nearby Galaxies.
[6]Mapping Nearby Galaxies at APO.

by low activity that persists until the present epoch.
Therefore it can be inferred that barred galaxies develop most of their star formation at early times and stabilize in a more quiescent state earlier than unbarred galaxies with equivalent mass and morphology properties. From this, therefore, one deduces that there is a close link between the presence of the bar and the early cessation of star formation in these galaxies, but what is not yet clear is whether the bar is the cause or the effect of this transition from active to quiescent galaxy in such remote epochs. In fact, one can think of a scenario in which the bar promotes a more rapid cessation of star formation, and this explains the fact that from observations the barred galaxies are redder than those without the bar. Another possible explanation is that bars are more difficult to form and evolve in galaxies with gas-rich disks and thus with high star formation, in which case the fact that barred galaxies are observed would imply that they first should have reached a quiescent state to favor bar development. This second view, however, does not explain why there are still a considerable number of bars in gas-rich disks. As long as no method is developed with the purpose of dating, observationally, the epoch of bar formation, it still remains outstanding what is the real cause-and-effect link between the presence of the bar and the reduced star formation rate.

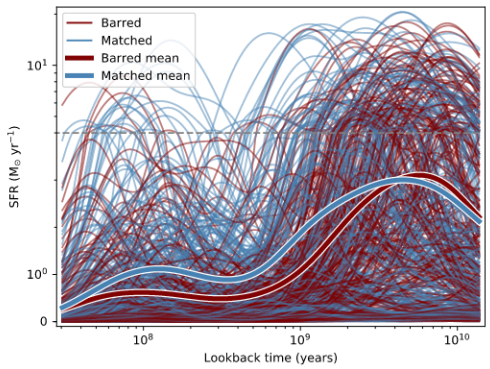

Figure 1.7: This plot shows the SFHs of the selected barred galaxies (brown curves) and those of their unbarred counterparts (blue curves). The bold curves are the average SFHs of both samples. To give a better view of the trends, a linear scale was used along the y-axis for SFR<4$M_\odot yr^{-1}$ and a logarithmic one for SFR>4$M_\odot yr^{-1}$. [Fraser-McKelvie et al., 2020]

Barred galaxies properties and related issues have been recently explored in a fully cosmological context through both high-resolution zoom-in simulations and statistical hydrodynamic ones [Zhao et al., 2020, Rosas-Guevara et al., 2020, Rosas-Guevara et al., 2022].
From zoom-in simulations it was pointed out that simulated galaxies form a strong bar after $z \sim 1$ [Spinoso et al., 2016] and that the star formation activity of strongly barred galaxies appears to be enhanced in the past and low in recent epochs [Carles et al., 2016]. Through cosmological hydrodynamic simulations, in particular IllustrisTNG50, it has been noticed that bar structures were born at $z \sim 0.7$ and they usually make the galactic disks become more compact than those of unbarred galaxies [Izquierdo-Villalba et al., 2022]. Moreover it is necessary to remark the fact that in IllustrisTNG50 simulation the implementation of bar formation mechanism is based just on the random development of dynamical conditions that triggers instabilities in stellar particles motions: e.g. intaraction with a close neighbor (external trigger), secular growth of the disk.

1.5 Cosmological simulations

The fundamental challenge in the attempt of understanding how galaxies form and evolve is that it occurs over such long timescales. Through whatever observational data and advanced telescope technology, we cannot in any case observe a galaxy through the billions of years of its evolution to see how it builds its bulge and disk, what drives changes in its star formation activity, or how it responds to interactions with other galaxies or changes in accretion rate. Various methods have been designed to trace galaxies across cosmic time, but they can only tell us about the statistical evolution of a population; they can give us a description of the buildup of a group of similar mass galaxies through time but cannot tell us how it happened. Another approach to this problem is to simulate galaxy formation rather than observe it. Simulating a Universe in a box allows us to track galaxies through time in order to see how they grow and to determine the key physical processes driving that growth. Cosmological hydrodynamical simulations evolve a box of dark matter, gas, stars and supermassive black holes through time using gravity and hydrodynamics. Refinement of these simulations has made us aware of the plethora of physical processes involved in galaxy formation and evolution processes. However, it is only in the last decade that magneto-hydrodynamical simulations have begun to produce galaxies with realistic morphologies.
Generally, these simulations can be divided in two types: cosmological volumes focusing on population statistics at the expense of resolution, and zoom-in simulations focusing on individual galaxies at the expense of population statistics. With gradual improvements in physical models, computational methods, and spatial resolution, it has become possible to simulate a cosmological volume with enough resolution to study the structural evolution of galaxies (thousands of galaxies at sub-kpc resolution). TNG50 is the highest resolution simulation of the IllustrisTNG project, covering a 50 Mpc box with an average spatial resolution of about 100pc [Pillepich et al., 2019]. Studying the structural evolution of galaxies and its relation to the regulation of star formation requires both the spatial resolution and the population statistics afforded by TNG50.

1.6 Spatially resolved studies

Before going on with the data analysis procedure, it is necessary to underline the importance of these spatially resolved studies that have gradually made room into the field of modern astrophysical research in recent years. As already mentioned, in this research field the formation and evolution of galaxies constitute one of the key problems to be studied, and in particular the focus is on understanding how galaxies go from being active in star formation to being quiescent or extinct. Thanks to the recent large surveys that have been conducted on large samples of galaxies at different redshifts (such as the Sloan Digital Sky Survey - SDSS), important statistical studies have been conducted, since data about millions of galaxies (even at different cosmic epochs) have begun to become available. As previously said about scaling relations (in Section 1.2), through these statistical studies, important empirical relations (initially involving integrated properties) were found among the main structural parameters of galaxies (e.g. Star Forming Main Sequence).
From the need to look for an explanation of how a galaxy can stop forming stars and become quiescent, the astrophysical research has been driven towards the so-called spatially resolved studies. Until a few years ago, the available instruments were only able to do integrated studies, since galaxies were observed just as point-like sources (not resolved). Thus one could only have integrated measurements on the entire galactic structure, such as the total amount of mass and star formation, the total mass of gas, etc.. From these kinds of studies one could only derive average trends between the integrated quantities of the various measured parameters, and this was not enough to deduce what physical processes may actually occurs

within galaxies causing their extinction. Therefore, the construction of new and powerful instruments and the introduction of IFS have enabled the diffusion of these spatially resolved studies, at least for galaxies in the local Universe. Nowadays this research technique is widely used. The goal of such spatially resolved studies is therefore to expand the knowledge of galactic evolution. In particular, they will undergo a major breakthrough as soon as they will be conducted on objects at more distant cosmic epochs as well. So far, thanks to these studies, it has been seen that many correlations, that are valid at the integral level (such as MS or KS), are also respected locally, on sub-kpc scales, and this suggests that the processes governing star formation are triggered locally.

1.7 Thesis outline

The main purpose of this thesis project is to further explore if the bar structure, which is a common feature in disk galaxies of the local Universe, has a role in the inside-out quenching of galaxies that host them. In particular, I carry out this study first performing a spatially resolved analysis based on both observational data, from the DustPedia database, and simulated ones, from the IllustrisTNG simulation. Then, once having constrained the main spatially resolved properties ($M_\star$ and SFR) of a sample of barred galaxies in the local Universe and having verified that they are quite well reproduced by simulated galaxies from IllustrisTNG, I take advantage of the fact that such cosmological simulation makes possible to extract an evolutionary trend of the analyzed galaxies. Therefore, I especially focus onto the time evolution of the total SFR of (simulated) barred galaxies with respect to the one of unbarred sources, with the aim of pointing out possible differences. In the end I compare the quenching of SFR due to the presence of bars (derived for the selected sample of galaxies) with the decreasing evolutionary trend of the Universe's star formation rate density [Madau and Dickinson, 2014].
Below I provide a brief content summary of each Chapter:

- Chapter 2 reports the description of the main steps that are performed in order to download, process and analyze observational data from DustPedia, with the aim of (i) retrieving the stellar mass and star formation rate spatially resolved distributions, (ii) exploring the relation between these two main quantities (i.e. spatially resolved Star Forming Main Sequence).

- Chapter 3 describes the whole procedure that is needed to (i) perform a spatially resolved analysis for a sample of barred and unbarred galaxies from IllustrisTNG simulation, (ii) retrieve the time evolution of their total SFR and of their spatially resolved MS.

- Chapter 4 is devoted to the discussion of the bar quenching issue, showing a comparison between the SFR decline found in simulated barred galaxies of Sample 2 (Chapter 3) and the Universe's star formation rate density evolution [Madau and Dickinson, 2014]. Besides this, it presents some final remarks about the main results of this work and some possible future perspectives in order to further investigate peculiarities of barred galaxies.

Chapter 2

DustPedia data analysis

As already anticipated, in the first part of this thesis I further investigate the spatially resolved Main Sequence relation of a sample of barred spiral galaxies in the local Universe, taking advantage of the publicly available DustPedia database [3].
This chapter is devoted to the description of the main steps that are performed in order to download, process and analyze observational data from DustPedia, with the aim of (i) retrieving the stellar mass and star formation rate spatially resolved distributions, (ii) exploring the relation between these two main quantities.

2.1 DustPedia project

DustPedia is a research project that was born to enable a much better characterization of the cosmic dust in the local Universe, particularly focusing on how it influences physical processes in the ISM and our observations [Davies et al., 2017, Clark et al., 2018].
The realization of this project was made possible by the legacy data from two cornerstone ESA[1] missions: Herschel[2] and Planck[3]. Actually a sample of nearby galaxies (within about 40Mpc) was constructed from the Herschel Science Archive [Pilbratt et al., 2010], in particular galaxies with an optical diameter larger than $1'$ and a WISE[4] 3.4µm signal-to-noise ratio (S/N)>5 were selected. The importance of studying galaxies in the local Universe is related to the aim of understanding the detailed processes of galaxy evolution, indeed nearby galaxies can be studied in far greater detail than those that lie at the edge of the cosmos. Besides this, the size constraint means that all the designated sources are extended in every Herschel band, even if they are not fully resolved, while the WISE flux provides the required stellar mass selection, since the best proxy for it is the near-infrared flux density.
It has to be noticed also that the Local Group galaxies of Andromeda, Triangulum, and the Magellanic Clouds were excluded from the final sample, because working with such exceptionally-extended systems would have implied fundamentally different data processing and analysis.
In the end 875 galaxies turned out to have the useful Herschel imaging coverage, at far-infrared

[1] European Space Agency.

[2] The Herschel Space Observatory was a ESA mission, active from 2009 to 2013. With its 3.5m mirror, it was the first (and the largest, until the launch of JWST in 2021) telescope that collected information about the appearance of the Universe in all the infrared and sub-millimeter wavelengths (55–672µm).

[3] Planck was a space observatory, conducted by ESA from 2009 to 2013, which mapped the anisotropies of the Cosmic Microwave Background (CMB) at microwave and infrared frequencies, with high sensitivity and small angular resolution.

[4] Wide-field Infrared Survey Explorer is a NASA infrared space telescope in the Explorers Program. It was launched in 2009 and it discovered thousands of minor planets and numerous star clusters.

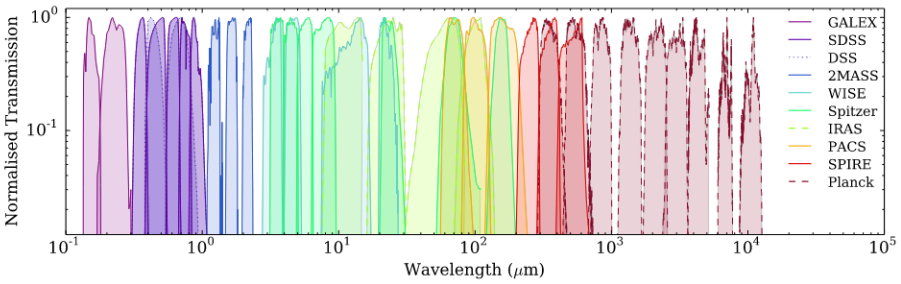

Figure 2.1: Illustration of the spectral coverage provided by the DustPedia database. This image shows the filter response functions of all available bands. [Clark et al., 2018]

and/or sub-mm wavelengths. Then these observations were combined also with data that are available at many other wavelengths from other databases, thus extending the possibility to perform studies from the ultraviolet to the microwave regime. The ancillary imaging data were gathered from other seven telescopes that observed large numbers of nearby galaxies: the GALaxy Evolution eXplorer (GALEX; [Morrissey et al., 2007]), the Sloan Digital Sky Survey (SDSS; [York et al., 2000, Eisenstein et al., 2011]), the Digitized Sky Survey (DSS), the 2 Micron All-Sky Survey (2MASS; [Skrutskie et al., 2006]), the Wide-field Infrared Survey Explorer (WISE; [Wright et al., 2010]), the Spitzer Space Telescope, ([Werner et al., 2004]) and Planck ([Planck Collaboration et al., 2011]). This resulted in just over 25,000 images, with many of the selected galaxies observed in 20 or more bands.
So the complete DustPedia data set, which is publicly available to the scientific community, contains standardised multi-wavelength imagery of all 875 galaxies in the sample, including both custom reductions and archival data, spanning over five orders of magnitude in wavelength from UV to microwave (see Figure 2.1).
In Section 2.3 I briefly report information about the various data sets used in this work.
All maps of DustPedia galaxies were produced in Flexible Image Transport System (FITS) format, with standardised file names and headers. The file name indicates: target galaxy, facility, and band in question. In cases where an error map was also available, it was stored in a separate FITS file. All galaxies are referred to by the name under which they are listed in the HyperLEDA database [1].

2.2 Sample

Based on the DustPedia data archive, I build a sample of barred spiral galaxies with the aim of extending the work already done by previous studies on normal galaxies. Indeed, it is important to conduct these spatially resolved studies also on galaxies with different morphological features (such as in this case the presence of the bar, or perhaps a dominant bulge) in order to expand current knowledge on star formation activity, which influences galactic evolution.
To properly select such barred spiral galaxies I first put some constraints on the Hubble stage index T, restricting its range between 2 and 7, and on the optical diameter D_{25}[5], considering only galaxies with $D_{25} > 4'$. The latter limitation ensures a selection of sufficiently extended galaxies so that their central regions hosting the bar can be properly investigated with enough resolution. Furthermore I focus only on sources that have a disk inclination $i < 65°$, in this way I avoid complications related to an eventually improper display of the circumnuclear regions. Besides all this, I select only spiral galaxies that show a bar structure, taking into

[5] D_{25} is the major axis of the 25-th level isophote, which is the one at which the value of the surface brightness falls below 25mag/arcsec^2 in the B band.

account their morphological classification (in addition to a visual inspection).
The final sample, used for the subsequent analysis, consists of ten objects: NGC1097, NGC1365, NGC1566, NGC3351, NGC3953, NGC4321, NGC4579, NGC4725, NGC5236, NGC5248. Distances, inclinations, sizes and integrated properties of the galaxies under consideration are presented below and summarized in Table 2.1.
All the sources are identified by their own equatorial coordinates (Right Ascension and Declination) at epoch J2000. For each galaxy, along with the morphological type, I report: luminosity distance in Mpc, inclination and R_{25} size in kpc. All these quantities are taken from the HyperLEDA database [Makarov et al., 2014] and are those adopted by the DustPedia collaboration. Moreover I show the total stellar mass and the total star formation rate, with the corresponding uncertainties, of all the selected sources. These integrated properties are expressed respectively in units of $M_\odot$ and of $M_\odot$/yr and they are taken from the results of [Nersesian et al., 2019], paying attention to properly rescale them in accordance with a Chabrier IMF [Chabrier, 2003]. Finally I also indicate the cell size, which is characteristic of each galaxy according to its distance and which is referred to the so-called *pixel-by-pixel* SED fitting procedure (in this case, with $8''$ square size, reported in kpc), that is fully explained in Section 2.4.

Galaxy Name	RA [deg]	Dec [deg]	D [Mpc]	i [°]	R_{25} [kpc]	$\log M_\star$ [$M_\odot$]	SFR [$M_\odot$/yr]	Cell size $8''$ [kpc]	Hubble Type
NGC1097	41.58	-30.27	14.72	55.0	21.82	$10.76^{+0.10}_{-0.13}$	4.13±0.66	0.57	SBb
NGC1365	53.40	-36.14	17.30	62.7	29.42	$10.69^{+0.12}_{-0.17}$	8.17±3.13	0.67	SBb
NGC1566	65.00	-54.94	6.14	47.9	6.31	$9.57^{+0.15}_{-0.23}$	0.44±0.08	0.24	SABb
NGC3351	160.99	11.70	9.91	54.6	10.17	$10.10^{+0.09}_{-0.11}$	0.68±0.15	0.38	SBb
NGC3953	178.45	52.33	12.47	62.1	10.89	$10.13^{+0.11}_{-0.14}$	0.36±0.29	0.48	SBbc
NGC4321	185.73	15.82	15.92	23.4	13.89	$10.46^{+0.09}_{-0.11}$	3.78±0.73	0.62	SABb
NGC4579	189.43	11.82	19.95	41.9	14.14	$10.88^{+0.05}_{-0.06}$	0.57±0.29	0.77	SBb
NGC4725	192.61	25.50	12.08	45.4	16.72	$10.64^{+0.07}_{-0.08}$	0.58±0.07	0.47	SABa
NGC5236	204.25	-29.87	4.90	14.1	9.38	$10.27^{+0.10}_{-0.13}$	4.20±0.69	0.19	SBc
NGC5248	204.38	8.89	11.97	56.4	6.91	$9.95^{+0.10}_{-0.13}$	1.30±0.22	0.46	SABb

Table 2.1: Main properties of the galaxy sample. Galaxy name, coordinates in J2000 system reference, distances D (in Mpc), inclinations, R_{25} sizes (in kpc) and morphological classifications (Hubble Type) are the same adopted by the DustPedia collaboration, and come from the HyperLEDA database. The values of $M_\star$ (in logarithmic scale) and SFR are obtained from [Nersesian et al., 2019]. Cell sizes are referred to the *pixel-by-pixel* SED fitting procedure (in this case, with $8''$ square size, reported in kpc).

2.3 Multi-wavelength observations

In order to analyze the sub-kpc scale relationship between the stellar mass and the star formation rate surface densities in the ten selected galaxies, I make use of observations in about 20 photometric bands.
Actually, thanks to the data derived from these multi-wavelength observations collected in the DustPedia archive, it is possible to exploit the power of such a complete multi-band photometric coverage, extending from the far UV to the far IR (i.e. from the observations conducted by the GALEX survey to those made by Herschel), in providing a reliable measure of the comprehensive SFR in galaxies, directly taking into account both the observed and dust-obscured components.
In Figure 2.2 I show, as an example, the galaxy NGC4725 as it is observed in six different bands: FUV with GALEX, g-band with SDSS, J-band with 2MASS, 4.5µm with Spitzer, 22µm with the WISE and 250µm with Herschel.
In the following paragraphs I briefly report information about the various data sets that I use in the subsequent analysis.

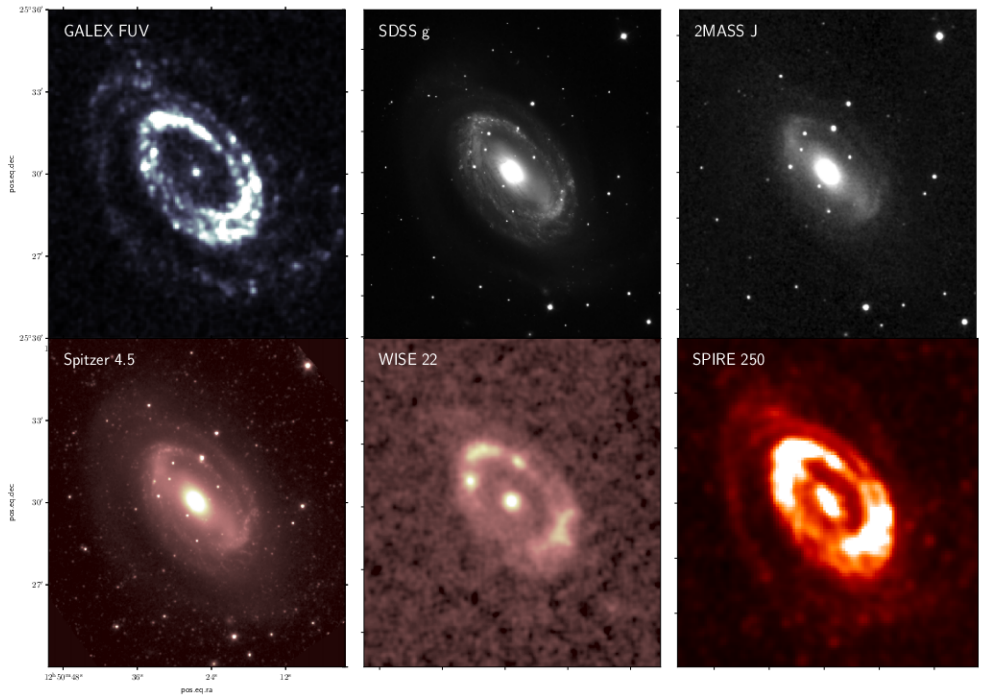

Figure 2.2: Example of the multi-wavelength imaging available for NGC4725, taken from the DustPedia database.

GALEX

GALEX samples the ultraviolet part of the electromagnetic spectrum, its data are divided in far-UV (FUV, 1516Å) and near-UV (NUV, 2267Å). These FUV and NUV data enable us to investigate the light coming from the newborn massive stars, tracing the unobscured star formation activity of galaxies. The observations in these bands are available for all the designated sources, except for NGC3953.

SDSS

The Data Release 12 of SDSS samples the optical part of the spectrum, which gives information about young stars. Five bands are used: u, g, r, i, z. The corresponding effective

wavelengths respectively are: 3351Å, 4686Å, 6166Å, 7480Å, 8932Å. Among the ten galaxies in the sample, four of them do not have these optical data: NGC1097, NGC1365, NGC1566, NGC5236.

2MASS

2MASS provides near-infrared (NIR) imaging data in three bands: J-band (1.25µm), H-band (1.65µm) and K_S-band (2.16µm). The maps related to these bands are available for the whole sample.

WISE and Spitzer

NIR and medium-infrared (MIR) observations comes from WISE and from the IRAC[6] camera on board of Spitzer. WISE collects data at 3.4µm, 4.6µm, 12µm and 22µm; while the IRAC camera performs observations at 3.56µm, 4.51µm, 5.76µm and 8µm. NIR and MIR imaging traces the old stellar component and the stellar mass distribution, along with carbonaceous and silicate materials that are typical of dust grains. These data are available for all the selected sources.

Herschel

The far-infrared (FIR) and the sub-mm portions of the spectrum are probed by the instruments on board of the Herschel Space Observatory. In the data analysis step both Herschel PACS[7] (70µm, 100µm and 160µm) and SPIRE[8] (250µm and 350µm) data are used. These wavelengths typically sample the reprocessed emission coming from dust, therefore they could constrain the dust-obscured star formation processes. Considering the sample of interest in this work, there are only two exceptions, NGC3953 and NGC5248, lacking 70µm data.

Summarizing what has been just reported, in this work I perform a spatially resolved study of ten barred galaxies, exploiting observations in 23 photometric bands that are collected in the DustPedia database. However it has to be noticed that not all of these multi-wavelength data sets are accessible for the whole sample. Actually all the 23 photometric bands are available only for NGC3351, NGC4321, NGC4579, NGC4725. While NGC5248 lacks PACS 70µm band; NGC3953 does not have GALEX FUV, NUV and PACS 70µm observations and finally 18 photometric bands are available for NGC1097, NGC1365, NGC1566, NGC5236 (since they lack all the five SDSS maps).

2.4 Methodology and SED fitting procedure

Main goal of the DustPedia data analysis is to obtain the spatially resolved distributions of the two main physical properties: stellar mass ($M_\star$) and SFR. With this purpose I carry out a SED fitting procedure, on scales varying from 0.19kpc to 0.77kpc, making use of the publicly available MAGPHYS code [da Cunha et al., 2008]. The methodology that I adopt to do the data analysis is the one that has been already used in previous literature works for a sample of normal spiral galaxies [Enia et al., 2020, Morselli et al., 2020]. I do so in order to make a consistent comparison with their results about unbarred galaxies. This procedure can be briefly summarized in three steps [Enia et al., 2020]: (i) degradation of the resolution

[6] Infrared Array Camera.
[7] Photodetector Array Camera and Spectrometer.
[8] Spectral and Photometric Imaging Receiver.

of each image to the worst PSF[9] that is available among the above 23 photometric bands, which is that of the 350µm image taken with the SPIRE instrument (24″); (ii) construction of a grid of square cells of a given size (in this case with 8″ side) and measure of the flux at each wavelength on them; (iii) derivation of the physical properties of the individual cells by performing SED fitting to the available photometric data.
I analyze each selected source considering cells of 8″ × 8″ (hence with a varying length side in physical scale from one galaxy to another, as reported in Table 2.1), which is the pixel scale of SPIRE 350 maps.

2.4.1 Pre-processing and PSF degradation

The starting point of this procedure are the different photometric observations of the galaxies, downloaded from the DustPedia archive (together with the associated errors, if available). Then the preliminary steps that are performed on each map are those related to the data reduction phase, which consists in: foreground stars removal, background estimation, flattening and subtraction, and PSF degradation, matching the maps resolution to the worst one.
Foreground stars removal is implemented taking advantage of the Comprehensive & Adaptable Aperture Photometry Routine (CAAPR) [Clark et al., 2018], which detects and removes foreground star emission, thus creating a star subtracted version of the map. Subsequently a background estimation and subtraction is performed on each of the star-subtracted maps. Finally, the stars and background subtracted maps are degraded to the PSF of SPIRE 350.

2.4.2 Photometry and SED fitting

In order to perform SED fitting, it is necessary to measure the flux in each photometric band inside the cells. With this purpose, the coordinate grid is generated using a quite customizable process, through which the user can choose the cells size (in this case cells of 8″ × 8″ are used) and the radius of the circle, centered on the galaxy center, within which the grid is built. Then the cells fluxes at the various wavelengths are measured and the ones with wavelength lower than 10µm are also corrected for Galactic extinction, thanks to the in-built module in CAAPR, based on values in the IRSA Galactic Dust Reddening and Extinction Service. Subsequently, to give an estimate of the flux errors, the error maps in the DustPedia archive are used and they are typically available for the Spitzer bands and for the far-IR photometry. In the cases in which no error map is available (i.e. the SDSS maps), it is worth to take the signal-to-noise ratio of the DustPedia Photometry in that particular band and use it to evaluate the error in each cell. The final result of this step of the analysis is a photometric catalogue, that contains the flux in every available photometric band from UV to far-IR, the corresponding errors, and the associated astrometric positions of the pixel/cell centres.
As already anticipated, to perform SED fitting I use the publicly available MAGPHYS code, which is one of the state-of-art code to model panchromatic SED. Through a Bayesian approach, it simultaneously models the observed emission in the UV-to-FIR regime by consistently assuming that the whole energy output is balanced between the one emitted at UV/optical/NIR wavelengths, that is absorbed by dust, and the one re-emitted in the FIR. Hence the previously measured fluxes (in all the grid cells) are given as an input to MAGPHYS for SED fitting. The current work, thanks to this pixel-by-pixel SED fitting procedure, probes physical scales that vary from ∼190pc for NGC5236 (which is the closest galaxy in the sample) to ∼770pc for NGC4579 (the most distant galaxy, as reported in Table 2.1).
The criterion that is adopted to establish if a fit has to be accepted or rejected is based on a χ^2 cut [Smith and Hayward, 2018], where such threshold value is fixed according to the number of photometric bands that are available for the selected objects. In particular, since

[9] Point Spread Function.

the galaxies of interest in this work are observed in a number of bands that can vary from 18 to 23 (as explained in Section 2.3), I use a conservative value for the χ^2 threshold that is 25.

2.4.3 Stellar mass and SFR estimates

Finally the output of this spatially resolved SED fitting process, performed by the MAGPHYS code, consists of a wide range of physical properties. Specifically I am interested in stellar mass ($M_\star$) and star formation rate (SFR), which are the two quantities that play a fundamental role in the characterization of the Main Sequence relation.
$M_\star$ values are directly taken from the MAGPHYS output. While SFR estimates are obtained by summing the unobscured component (SFR_{UV}) and the one that is obscured by dust absorption and then re-emitted in the IR (SFR_{IR}). The SFR_{UV} contribution is estimated using the relation [Bell and Kennicutt, 2001]:

$$SFR_{UV} = 0.88 \cdot 10^{-28} L_{UV,\nu} \tag{2.1}$$

where $L_{UV,\nu}$ is the luminosity at 150nm, expressed in erg s^{-1} Hz^{-1} and taken from the SED fit. While the SFR_{IR} component is derived from the relation [Kennicutt, 1998b]:

$$SFR_{IR} = 2.64 \cdot 10^{-44} L_{IR} \tag{2.2}$$

where L_{IR}, given in erg s^{-1} by the SED fit, is the luminosity integrated between 8µm and 1000µm (rest-frame). In both cases, the relations have been rescaled in accordance with a Chabrier IMF [Chabrier, 2003].
The SFR values are derived from the above empirical relations in order to make them less model dependent with respect to the ones obtained from the SED fit, that are more dependent on degenerate parameters like age, metallicity and extinction. This choice is also supported by what has been found for normal galaxies [Enia et al., 2020], for which the SFR computed as the sum of Equations 2.1 and 2.2 and the one given by MAGPHYS are highly consistent. Such empirical approach takes into account the contribution of two extreme stellar populations: the UV emission from young stars and the obscured young stellar component that is still hidden in the dusty molecular clouds.

2.5 Spatially resolved distributions

In this section I show the spatially resolved distributions of the stellar mass surface density $\Sigma_\star$ and of the star formation rate surface density Σ_{SFR}. In particular here I exhibit the results related only to three representative galaxies in the sample: NGC4725, NGC5236 (also known as the Southern Pinwheel Galaxy or M83), NGC3351; the others are collected in Appendix A. The RGB images of the three considered galaxies are the ones in Figure 2.3.
Each plot in Figures 2.4 and 2.5 includes also a dashed black circumference of radius equal to R_{25}. Moreover the points represented as dots are those corresponding to cells in which the SED fitting is characterized by a χ^2 greater than the threshold value (set at 25) and therefore they are rejected.

2.5.1 Stellar mass

As already said in 2.4.3, the stellar mass values of the single cells are directly obtained from the output of the MAGPHYS program used in the SED fitting procedure. Then to get the values of the corresponding surface density, which are those plotted in the following images, it is necessary to simply divide the stellar mass of each grid element by the area of the individual cell within which it is contained. As can be seen from the following Figure 2.4, the stellar mass is more concentrated in the central areas of the galaxies: a particularly

(a) (b) (c)

Figure 2.3: RGB images of NGC4725 (a), NGC5236 (b) and NGC3351 (c).

well-defined spheroidal structure in the center (the bulge) is evident and the bar appears to be grafted onto it. Indeed in all the three galaxies it is easy to glimpse the presence of an elongated structure departing from the central bulge. Thus it can be concluded that the stellar component traces the presence of the bar. From the maximum concentration of stars in the bulge, a progressive decrease in stellar mass toward the outer regions is then observed. All this confirms the exponential growth trend that stellar mass follows if one proceeds from the outskirts to the internal regions of disk galaxies.

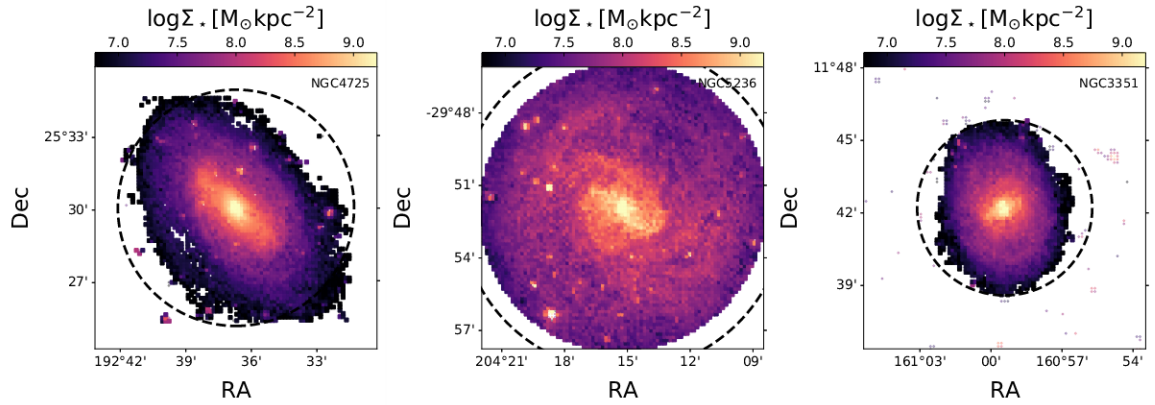

(a) (b) (c)

Figure 2.4: Spatially resolved distribution of the stellar mass surface density, expressed in logarithmic terms (log$\Sigma_\star$), in NGC4725 (a), NGC5236 (b) and NGC3351 (c).

2.5.2 Star Formation Rate

The total SFR in each grid cell is calculated as the sum of the directly observable component of star formation activity (SFR_{UV}, Eq. 2.1) and the one that is instead obscured by dust and then re-emitted in the IR (SFR_{IR}, Eq. 2.2). From the spatially resolved distributions shown below (Figure 2.5), it can be noticed that there is a common tendency for the SFR to grow towards the centre of the three galaxies, where also the mass concentration is higher (as seen above, Figure 2.4). This actually confirms the MS relation, which predicts a linear growth (in logarithmic terms) of the SFR as the stellar mass increases (see 1.2.1).
Besides that, the SFR maps of NGC4725 and NGC3351 are comprehensively characterized by lower values with respect to the one of NGC5236 and this can be pointed out also from the plots in the log$\Sigma_\star$ - logΣ_{SFR} plane (Figure 2.6) and from the total SFR values shown in Table

2.1. In these two cases (NGC4725 and NGC3351) the highest values of Σ_{SFR} seem to trace, albeit moderately, the spiral arms structures, which actually host star formation processes, since larger amounts of gas and dust are present there. Moreover, further inward than the mildly star forming region corresponding to the winding of spiral arms departing from the bar ends, it can be identified an almost annular and more quenched structure that coincides with the circumnuclear region hosting the bar. Then an increase in SFR is observed in the central spheroid of NGC3351, while in NGC4725 the bulge turns out to be less star forming. For what concerns NGC5236, it is clear that the overall SFR surface density is characterized by higher values that well identify both the bulge and the spiral arms. What specifically happens in the bar region can be better inferred from the corresponding plot in Figure 2.6.

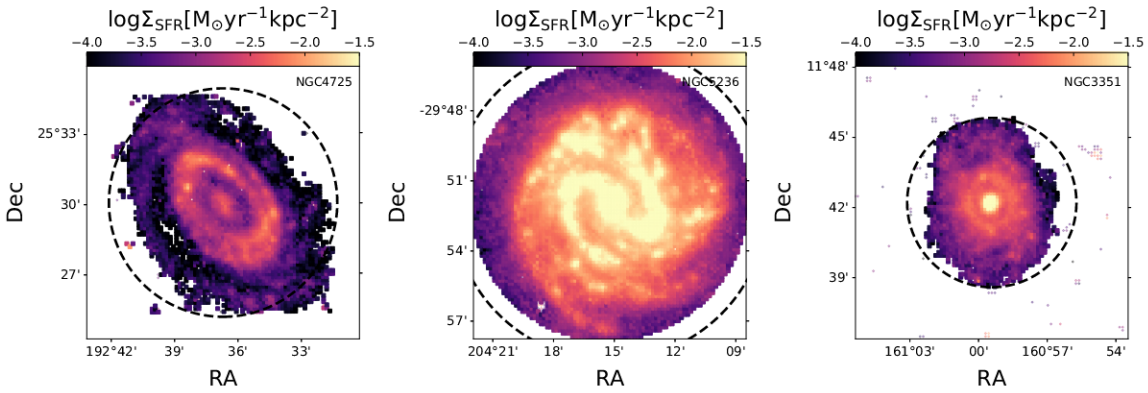

(a) (b) (c)

Figure 2.5: Spatially resolved distribution of the star formation rate surface density, expressed in logarithmic terms ($\log\Sigma_{SFR}$), in NGC4725 (a), NGC5236 (b) and NGC3351 (c).

2.6 Results

This section is devoted to the presentation of the results obtained for the spatially resolved Main Sequence relations of the sampled galaxies. Along with the plots in the $\log\Sigma_\star$ - $\log\Sigma_{SFR}$ plane for the three representative galaxies (NGC4725, NGC5236, NGC3351), I briefly describe also how the various resolved regions of each galaxy are arranged with respect to the best fit MS. The results related to the other seven objects are shown in Appendix A.

2.6.1 Spatially resolved MS

As already said the spatially resolved MS relation involves stellar mass and star formation rate and it is expressed as a linear function in the $\log\Sigma_\star$ - $\log\Sigma_{SFR}$ plane. The specific MS of each galaxy of the sample is determined by implementing the Orthogonal Distance Regression (ODR) technique, through the SCIPY package of Python.
In this way one finds a linear relation, between the logarithms of the quantities involved, of the type: $\log\Sigma_{SFR} = m \cdot \log\Sigma_\star + q$. To find the values of the slope m and of the intercept q, the χ^2 of the points distribution must be minimized; using the ODR method the χ^2 is minimized orthogonally to the best-fit line.
In Table 2.2 I display slopes and intercepts (with their corresponding uncertainties) of the fitted MS relations for all the ten barred galaxies.
The best-fit lines (magenta lines) of the three considered galaxies are shown in Figure 2.6 and, along with them, it is reported also the MS (black line) obtained for a sample of unbarred gran design spiral galaxies from DustPedia [Enia et al., 2020]. The latter is given by the

following expression:

$$log\Sigma_{\rm SFR} = 0.88 \cdot log\Sigma_{\star} + 9.05 \tag{2.3}$$

As can be seen from the three plots in Figure 2.6, the distribution of points (corresponding to the grid cells) is color coded as a function of the distance from the center (normalized to the value of R_{25}). From the application of this color code it can be seen that, indeed, going towards the center of the galaxies the stellar mass increases and, with it, so does the star formation rate according to this log-linear relation.
Furthermore, by comparing the overall trends for these three barred galaxies with the one representing the MS of normal spirals (black line, [Enia et al., 2020]), it can be said that:

- In NGC4725 and NGC3351 the points lie below the relation found for normal spiral galaxies and this shows a systematically lower star formation rate. In these two cases we also have that the slopes of the fitted MS relations are in agreement with the one of the black line, while the intercepts have smaller values.

- In NGC5236 we have a quite different trend. As already mentioned, it has SFR values that are typically larger than in the other two cases and this actually translates in the fact that the points, especially the ones corresponding to the central regions of the galaxy, are located in the upper part of the $\log\Sigma_{\star}$ - $\log\Sigma_{\rm SFR}$ plane. Moreover the slope of the fitted MS is much larger than the one found for unbarred galaxies, this means that the growth trend of the SFR going toward the galaxy center appears to be more rapid.

Subsequently, focusing on the central regions of the three galaxies, which are the ones of interest in order to better investigate the impact of the bar structure, it can be pointed out that:

- In the cases of NGC4725 and NGC5236 there is a strong feature of anti-correlation in correspondence of the circumnuclear region, hosting the bar. Actually these points turn out to be arranged in a direction approximately orthogonal to the fitted MS. From this fact it can be inferred that in the bar region, at increasing mass, the SFR decreases (more or less rapidly depending on the hosting galaxy). Moreover going towards the very centre of these two galaxies (and so probing their bulge), it is noticeable the fact that the SFR gets back to having an increasing trend as the stellar mass grows, but these very central points still appear to lie below the best-fit MS of each galaxy. This implies that the nuclear regions are less star-forming than what would be expected once their stellar mass is known.

- Also looking at NGC3351, one can catch a glimpse of the anti-correlation feature in correspondence of the bar, even though here it is less pronounced than the one in the other two galaxies. Besides that, unlike NGC4725 and NGC5236, it can be seen that the closest points to the galaxy center lie above the best-fit relation (magenta line) and this indicates that they are more star-forming than what would be predicted by the MS, given their stellar mass.

Therefore, from these three representative galaxies, it can be emphasized the fact that the bar hosting region is typically quenched or on the way to be quenched (lower values of SFR, anti-correlation feature), while the bulge can show two different behaviours: in some cases it is still active in forming stars, in some others it tends to be quiescent. The same bimodal trend related to the galactic nucleus can be pointed out also in the other seven galaxies of the sample, the results of which are summarized in Appendix A.

Galaxy Name	m±Δm	q±Δq
NGC1097	1.15 ± 0.11	-11.57 ± 0.84
NGC1365	1.01 ± 0.10	-10.17 ± 0.79
NGC1566	0.89 ± 0.09	-9.23 ± 0.71
NGC335	0.94 ± 0.07	-10.06 ± 0.53
NGC3953	0.73 ± 0.10	-8.38 ± 0.80
NGC4321	1.44 ± 0.13	-13.63 ± 0.99
NGC4579	1.77 ± 0.15	-17.18 ± 1.20
NGC4725	0.99 ± 0.05	-10.69 ± 0.39
NGC5236	2.29 ± 0.12	-20.31 ± 0.92
NGC5248	1.15 ± 0.12	-11.26 ± 0.93

Table 2.2: Slopes, Intercepts and associated uncertainties of the fitted MS relations for the ten barred galaxies selected from DustPedia. All these quantities are given as output of the ODR regression function implemented in the SCIPY package of Python.

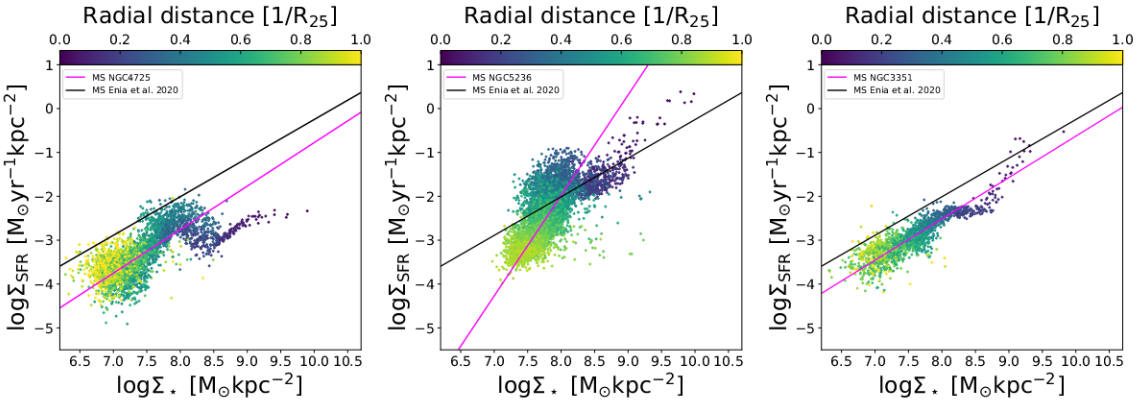

(a) (b) (c)

Figure 2.6: Spatially resolved Main Sequence relation of NGC4725 (a), NGC5236 (b) and NGC3351 (c). In each panel the magenta line is the fitted Main Sequence (through the ODR technique), while the black line is the best fit MS obtained for a sample of normal galaxies [Enia et al., 2020].

2.6.2 Distance from MS

As a final step, I reproduce the spatially resolved maps of the grid cells distribution color coded as a function of the distance from the best fit MS of each galaxy (see Figure 2.7). Also in these plots it is included a dashed black circumference of radius equal to R_{25}.
Thanks to these panels one can get, at a first glance, an idea of what is happening in each of these galaxies: the red cells correspond to regions that are less star forming than what the fitted MS would predict, while the blue ones are associated with particularly active regions. For what as been said so far about NGC4725 and NGC5236, their central parts (including both the bulge and the bar hosting region) appear to be red, and so quenched; while their spiral arms show a tendency of being active in star formation. On the contrary, NGC3351 exhibits a star-forming nucleus with a red (quiescent) annular region around it.

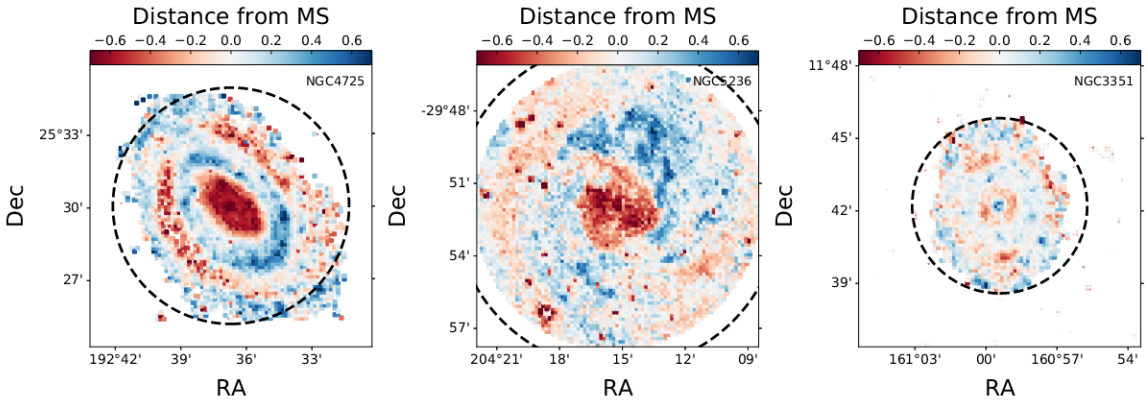

(a) (b) (c)

Figure 2.7: Cells distance from the fitted MS in NGC4725 (a), NGC5236 (b) and NGC3351 (c).

Chapter 3

IllustrisTNG data analysis

The second part of the data analysis of this work has the aim of exploring what cosmological simulations can predict about the impact of bars on their hosting galaxies.
From the previous analysis conducted on observational data related to local barred galaxies, it has been found that in correspondence to the bar structure there is a typically less star-forming region which produces the quite impressive anti-correlation track with respect to the Main Sequence. However, so far, this specific trend has been detected just at one observational epoch, z $\sim$ 0 in this case, then it is not possible to understand if the bar has effectively a fundamental role in quenching the host galaxy over time. For this reason I further investigate this issue through the IllustrisTNG simulation, in particular I take advantage of the fact that such cosmological simulation makes possible to extract an evolutionary prospectus of the galactic star formation (i.e. Star Formation History).
In this chapter I show the whole procedure that is needed to (i) perform a spatially resolved analysis for a sample of barred and unbarred galaxies from IllustrisTNG simulation, (ii) retrieve the time evolution of their total SFR and of their spatially resolved MS.

3.1 The IllustrisTNG project

The IllustrisTNG (The Next Generation, [2]) project [Nelson et al., 2019] has the purpose of enlightening the physical processes involved in galaxy formation and evolution, in order to make predictions about some of their properties supported by current or future observational surveys.
It is a successor to the original Illustris simulation and consists of three main cosmological, gravo-magneto-hydrodynamical simulations of galaxy formation with different volumes (50^3, 100^3 and 300^3 cMpc^3), each one with different spatial and mass resolutions, for a total of 18 simulations. All these simulations run with the moving-mesh AREPO code, adopting as cosmological parameters the ones from [Planck Collaboration et al., 2016]: $\Omega_\Lambda = 0.6911$, $\Omega_m = 0.3089$, $\Omega_b = 0.0486$, $\sigma_8 = 0.8159$, $h = 0.6774$ and $n_s = 0.9667$ where Ω_Λ, Ω_m, and Ω_b are the average densities of matter, dark energy, and baryonic matter in units of the critical density at z = 0, σ_8 is the square root of the linear variance, h is the Hubble parameter ($H_0 = h100$ km s^{-1}) and n_s is the scalar power-law index of the primordial perturbations power spectrum.
For the purpose of this thesis I use the TNG50 simulation, which is the one with the highest resolution power and it also evolves a large enough cosmological volume for studying statistical properties of intermediate mass galaxies. In particular the simulation realizes a 51.7cMpc box sampled by 2160^3 gas cells and the same number of dark matter particles, with a mean mass resolution of $8.5 \cdot 10^4 M_\odot$ and $4.5 \cdot 10^5 M_\odot$ respectively. The main characteristics of the

L	[Mpc]	51.7
N		$2{\cdot}2160^3$
m_{baryon}	[$M_\odot$]	$8.5{\cdot}10^4$
m_{DM}	[$M_\odot$]	$4.5{\cdot}10^5$
$\epsilon_{gas,min}$	[pc]	74
$\epsilon_{DM,\star,0}$	[kpc]	0.288
$\epsilon_{DM,\star,z}$	[kpc]	0.58 to 0.29

Table 3.1: Main features of the TNG50 simulation. From top to bottom: box side-length, number of initial resolution elements including gas cells and dark matter (DM) particles, initial mass of baryon cells and of DM particles, the minimum proper softening length allowed for gas cells, the proper softening length for the collisionless particles at z = 0, and their comoving softening length.

simulation are shown in Table 3.1.

3.1.1 Subgrid physics: star formation mechanism

In hydrodynamical simulations, like the IllustrisTNG, the process of star formation can not be treated following in detail the local physical mechanisms involved. So the algorithm that is implemented to reproduce the conversion of gas particles into stars is based on a probabilistic approach.
First of all, each gas particle is eligible for star formation only if it satisfies some criteria:

* the particle is denser than $n_H \sim 0.1$ cm^{-3};
* the particle is in an overdense region;
* the particle is part of a converging flow;
* the particle is Jeans unstable: if the temperature and pressure of one gas particle inside its surrounding sphere is not able to support the whole sphere against gravitational collapse.

Further details about these selected criteria can be found in [Stinson et al., 2006].
Once these criteria are fulfilled, stars should form according to a theoretical star formation rate given by:

$$\frac{d\rho_\star}{dt} = c_\star \frac{\rho_{gas}}{t_{form}} \tag{3.1}$$

where $\rho_\star$ and ρ_{gas} are the volume densities of star and gas particles respectively, $c_\star$ is a constant efficiency factor and t_{form} is the star formation dynamical timescale. The latter actually is a density-dependent timescale and goes like: $t_{form} = t_{dyn} \sim \rho^{-1/2}$.
Both $c_\star$ and t_{form} are enforced to empirically reproduce the Kennicutt-Schmidt (KS) relation. It was originally formulated by [Schmidt, 1959] using the gas volume density and the number of stars formed in the solar neighborhood, then it was subsequently derived by [Kennicutt, 1998a] for radially averaged surface densities in external galaxies. The KS power law ($\Sigma_{SFR} \sim \Sigma_{gas}^n$) relates the fuel of star formation to its final product: stars. In one of the earliest works, [Kennicutt, 1998a] found a super linear correlation (n = 1.4-1.5) between the total gas and the SFR surface densities.
Because of the limited resolution issue, only the global behaviour of star formation can be captured. Actually in many cases the stellar mass that should be subtracted from the gas particle mass, according to what Equation 3.1 predicts, is too small with respect to the minimum resolvable baryonic mass ($\sim 10^{4\div5}$ $M_\odot$). Such small masses would introduce spurious

numerical error in the simulation, since they would be highly affected by the presence of other higher mass particles, and so they cannot be actually formed. The way IllustrisTNG treats this issue is based on a stochastic recipe in order to establish when and where stars, of a high enough mass, should form. Indeed for a gas particle one can estimate the probability to give birth to a star as:

$$p = \frac{m_{\rm gas}}{m_\star}[1 - e^{-c_\star \Delta t / t_{\rm form}}] \tag{3.2}$$

where Δt is the timestep, $m_{\rm gas}$ is the mass of the gas particle and $m_\star$ is the mass of the potentially spawned star particle.
At this point, to establish if a certain gas particle is actually converted into a star or not, a random number r is generated between 0 and 1 and if $r < p$ a new star particle is finally formed. Otherwise the gas particle remains as it is.
The output of this process is a set of newly born star particles with a discrete distribution in terms of mass and position. Only star particles with masses above the resolution limit are present and they are located in overdense regions where gas has the highest probability of producing them.

At this point the SFR can be evaluated also in a different way with respect to the theoretical gas-based estimate (Equation 3.1), which does not take into account where it is more probable to form stars and thus it may not be properly representative of the final distribution of gas and star particles in a simulated galaxy. The computation of the SFR based on star particles should be better comparable with real data and has a minimum resolvable value ($\rm SFR_{min}$) related to the minimum baryonic resolvable mass.
From an observational point of view, the computation of SFR is obviously derived from a different approach, based on photometry (as seen also in the previous Chapter 2). There is a series of indicators which link the luminosity of a galaxy, at different wavelengths, to the rate at which stars are formed. These tracers cover the full electromagnetic spectrum: from X-ray and ultraviolet (UV) to the radio regime, via optical and infrared (IR) bands, and they can be based on both continuum and line emissions. Their calibration takes into account different timescales, ranging from a few to hundreds of million years [Donnari et al., 2019].
As a consequence, to establish a comparison between models and observational results, I need to match the computation of SFR obtained from IllustrisTNG and from observations in a compatible way. I am going to explain how to do this in Section 3.3.

3.1.2 Galaxy identification

Galaxies and their haloes are bound substructures identified by a FoF and then a Subfind algorithm and connected over time by the SubLink merger tree algorithm.

3.2 Sample

In this work I need to study spatially resolved properties of the barred galaxies that I sample from the [Rosas-Guevara et al., 2022] catalogue available in the IllustrisTNG simulation. From the same catalogue I also extract a control sample of unbarred galaxies, in order to make a comparison about the two main properties that enter into the Main Sequence relation: stellar mass and star formation rate.
A brief explanation of the parent sample is needed: Rosas-Guevara and collaborators first selected disk galaxies with a stellar mass $\geqslant 10^{10}$ $\rm M_\odot$ to ensure a proper resolution. They identified this sample by using the kinematic bulge-to-disk decomposition and computing the ratio (D/T) between the disk stellar mass and the stellar mass enclosed in $10 \times r_{50,*}$, where $r_{50,*}$ is the radius within which 50 per cent of the total stellar mass is contained. Then they

Dataset	Units	Description
SubfindID		The Subfind ID of the main progenitor of the disk galaxy sample. If untracked at this snapshot, the value is -1.
TabAmax2		The strength of the bar, i.e. the maximum of A_2.
TabRbar	[pkpc]	The size of the bar.
Bartype		Values are: 1 for barred galaxies, and 0 for unbarred galaxies.
TabMstar	[$M_\odot$]	The stellar mass of the galaxy.

Table 3.2: Properties of galaxies that are present in the catalogue [Rosas-Guevara et al., 2022].

defined disk-dominated galaxies as those ones with D/T $\geqslant$ 0.5. They also searched for disk galaxies at six discrete redshifts: z = 0,0.5,1,2,3,4. The whole sample obtained at the end was made of 1062 galaxies.
Moreover they classified the disk galaxies in the selected sample, dividing them in barred and unbarred galaxies according to the presence or absence of a clear and persistent bar structure in the disk. The identification of these non-axisymmetric structures is performed through a Fourier decomposition of the face-on stellar surface density. They considered the $A_2(R)$ parameter, defined as the ratio between the second and zero terms of the Fourier expansion, as the tracer of non-axisymmetric features. It is given by:

$$A_2(R) = \frac{|\Sigma_j m_j e^{2i\theta_j}|}{\Sigma_j m_j} \tag{3.3}$$

where m_j is the mass of the j-th particle and θ_j is the angular coordinate on the galactic plane. The strength of the bar is defined by the peak value of $A_2(R)$, $A_{2,\max}$, and when it is greater than 0.2 the galaxy is classified as barred. For further details related to the sample of galaxies and their classification see the original paper [Rosas-Guevara et al., 2022]. This catalogue contains properties about bars of the disk galaxy sample, the available fields are shown in Table 3.2.
In order to perform the spatially resolved analysis, I focus on the galaxy sample at z = 0 which contains 349 disk galaxies. Among them the percentage of barred galaxies is about 30 per cent, which is a slightly lower but comparable value with respect to the one expected from observations ($\sim$40% in optical bands) in the local Universe.
Looking at the distribution of stellar masses of these 349 galaxies, the majority of them seems to have $M_\star \lesssim 10^{10.6} M_\odot$ and these are also the ones with a lower fraction of bars. Actually, in agreement with observational results, the fraction of barred galaxies tends to increase with stellar mass.
Furthermore to get an overall view of how this sample of 349 objects is arranged in the log$M_\star$ - logSFR plane (the two main physical properties in which I am interested into) I report the plot in Figure 3.1. I emphasize the fact that this is the integrated MS relation of the parent sample [Rosas-Guevara et al., 2022], each point in this plot represents an object with a certain $M_\star$ and a certain amount of total SFR. The latter is the value that is obtained from the gas-based estimate (Equation 3.1), which is the so-called instantaneous SFR. It is explained below (Sec. 3.3) how to retrieve this information from the IllustrisTNG50 database. From this plot it is confirmed the fact that barred galaxies (red dots) are much more numerous at higher masses and, besides that, they also seem to bend the MS since they systematically show lower values of total SFR with respect to the unbarred ones (blue dots).
I report below the best-fit MS relations, found (through the least square fitting method)

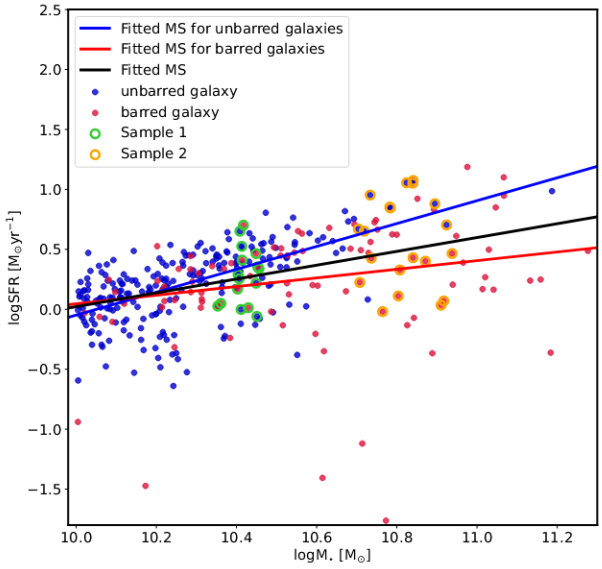

Figure 3.1: Integrated Main Sequence relation of the parent sample [Rosas-Guevara et al., 2022]. Blue points represent unbarred galaxies, while red points correspond to barred ones. The blue MS is fitted through the least squares method using only the points related to unbarred galaxies, analogously the red MS is obtained for the barred ones. Finally the black line is the best-fit MS for the whole sample. Barred and unbarred galaxies belonging to Sample 1 are highlighted with green circles, instead Sample 2 galaxies are the ones in orange.

respectively for: unbarred (U) galaxies, barred (B) galaxies and the whole sample (T).

$$(U) : logSFR = 0.95 \cdot logM_\star - 9.59 \tag{3.4}$$

$$(B) : logSFR = 0.36 \cdot logM_\star - 3.55 \tag{3.5}$$

$$(T) : logSFR = 0.58 \cdot logM_\star - 5.74 \tag{3.6}$$

For the purpose of the current work I decide to select two sub-samples of galaxies at z = 0, which seem to have interesting characteristics for the further analysis.

- Sample 1: 8 barred galaxies and 8 unbarred galaxies (control sample) in the narrow range $10^{10.35}$ $M_\odot \leqslant M_\star \leqslant 10^{10.47}$ $M_\odot$. I select objects in such range of masses because they have the right balance between: resolution (not too low total stellar mass of the galaxies), number of barred/unbarred galaxies and total number of galaxies in the bin.
- Sample 2: 10 barred galaxies and 10 unbarred galaxies (control sample) in the range $10^{10.70}$ $M_\odot \leqslant M_\star \leqslant 10^{10.94}$ $M_\odot$. I choose these other objects in such range of higher masses because they are probably more representative of the quite evident dichotomy between barred and unbarred galaxies showing up in the integrated MS plot (Figure 3.1).

3.3 Spatially resolved analysis

So far the selection phase of the two sub-samples has been described.
I show the SubfindIDs of the chosen subhalos in Sample 1 with their respective main properties (stellar mass and eventually bar size) in Table 3.3.
On the other hand, I display the SubfindIDs of the selected subhalos in Sample 2 with their

SubfindID (barred)	$M_\star$ [10^{10} $M_\odot$]	R_{bar} [kpc]	SubfindID (unbarred)	$M_\star$ [10^{10} $M_\odot$]
487743	2.61	3.20	117266	2.56
548418	2.59	2.96	589873	2.53
560082	2.84	2.24	590218	2.49
563943	2.81	2.16	591469	2.35
589655	2.53	3.20	561325	2.59
377658	2.26	3.04	450917	2.82
608386	2.30	3.92	596866	2.86
603185	2.69	1.84	428179	2.81

Table 3.3: Main properties of galaxies in Sample 1. For each subhalo it is reported the corresponding ID, the total stellar mass and the bar size (if a bar structure is present). These values are available in the catalogue produced by [Rosas-Guevara et al., 2022], as shown also in Table 3.2.

SubfindID (barred)	$M_\star$ [10^{10} $M_\odot$]	R_{bar} [kpc]	SubfindID (unbarred)	$M_\star$ [10^{10} $M_\odot$]
523889	5.45	2.48	477328	6.08
535410	6.36	4.64	480802	5.06
547844	5.10	3.92	531910	5.41
552414	5.81	2.80	537236	6.06
503437	7.43	3.92	537941	5.23
371127	8.26	4.00	117254	6.91
333425	8.13	2.00	372755	6.93
394621	6.92	5.12	479938	6.67
264887	6.42	1.60	485056	8.39
501208	8.66	1.84	502995	7.85

Table 3.4: Main properties of galaxies in Sample 2. Same format as in Table 3.3.

PartType0 (gas)		
Field	Units	Description
Coordinates	[ckpc h^{-1}]	Comoving coordinate.
Masses	[10^{10} $M_\odot$ h^{-1}]	Gas mass in this cell.
StarFormationRate	[$M_\odot$ yr^{-1}]	Instantaneous SFR of this gas cell.
Velocities	[km $\sqrt{a}$ s^{-1}]	Spatial velocity.
PartType4 (stars)		
Field	Units	Description
Coordinates	[ckpc h^{-1}]	Comoving coordinate.
Masses	[10^{10} $M_\odot$ h^{-1}]	Mass of this star cell.

Table 3.5: These are the main fields extracted from the TNG50 dataset for gas and star particles. `"Coordinates"` are expressed in *comoving kpc* over h, with h the Hubble parameter ($h = 0.6774$); `"Masses"` in units of $M_\odot$ over h multiplied by 10^{10}; `"StarFormationRate"` is considered in $M_\odot$ over year and `"Velocities"` in km/s multiplied by the square root of the scale factor $a = 1/(1+z)$ to get the proper velocities.

respective main properties (stellar mass and eventually bar size) in Table 3.4.
Thanks to the SubfindIDs I can retrieve information about all these selected subhalos from the TNG50 simulation, downloading the whole dataset of the corresponding gas (PartType0), stars (PartType4) and black holes (PartType5) particles. Among all the available fields for each type of particles, I am going to use, for the moment, only the ones needed to build up the spatially resolved Main Sequence, so considering just gaseous and stellar particles. I summarize them in Table 3.5.
Before going on with all the steps of the subsequent analysis I convert the units of measure used by the IllustrisTNG50 simulation (as specified in the Table 3.5) into physical units. I express all spatial coordinates in kpc, masses in $M_\odot$ and velocities in km/s.

3.3.1 Galactic rotation

In order to study the spatially resolved Main Sequence relation, it is necessary first to get the face-on view of all the galaxies. This is obtained by rotating the reference frame attached to each galaxy, so that the z-axis of the new rotated Cartesian reference frame becomes coincident with the rotation axis of the galaxy itself. Since the sampled galaxies are disk galaxies, I identify the rotation axis of each one computing the total angular momentum, assumed to be perpendicular to the rotating disk. The disk itself is actually made of both gas and star particles, but they have slightly different behaviours. Gas particles tend to settle down towards the median plane of the disk thanks to different mechanisms involving viscous forces, in this way they acquire nearly circular velocities with a very low dispersion along radial and vertical directions. On the other hand stellar orbits are characterized by a higher velocity dispersion and this leads them to be distributed on a more ellipsoidal structure, so they are not the most suitable tracer for the thin disk component of the galaxies.
These considerations justify the choice of considering only the gas particles for the computation of the rotation matrix which has then to be applied to all the particles of the galaxy, including stars. This is done to have a coherent and consistent view of the object. I set the centre of the galactic reference frame on the 0-th gas particle[1] (which is the most bound in the subhalo) and I rescale the gas particle velocities subtracting the subhalo peculiar velocity. At this point I would need to compute the total angular momentum of the gas particles, but

[1]For the galaxies that show an internal very gas-poor region (especially the most massive ones), the 0-th stellar particle is chosen to set the centre of the new reference frame.

another important aspect has to be taken into account. Not all the subhalo gas particles are the ones that effectively trace the thin disk of the galaxy, indeed most of them are distributed on a wide spheroidal halo (with size of the order of r $\sim$ 100 kpc) surrounding the actual region within which spiral arms are extended. It is exactly this latter the portion of galaxy to be considered. Since the value of the R_{25} radius is not available for our simulated galaxies, I decide to consider just the gas particles included within a sphere of radius 25 kpc, as a conservative estimate of the region of interest, and I compute their specific total angular momentum:

$$\vec{J}_{\rm tot} = \frac{\Sigma_i \vec{j_i}}{M_{\rm gas,25}} = \frac{\Sigma_i (\vec{r_i} \times m_i \vec{v_i})}{M_{\rm gas,25}} \tag{3.7}$$

where $\vec{r_i}$, m_i, $\vec{v_i}$, $\vec{j_i}$ are respectively coordinates, mass, velocity and angular momentum of each gas particle and $M_{\rm gas,25}$ is the total mass of gas particles within the region of radius 25 kpc.
At this point, with each component of the specific total angular momentum it is possible to evaluate the Euler angles needed to build up the rotation matrix. Finally this latter is applied to all the gas and star particles coordinates. Assuming that the line of sight rotates with the reference frame attached to each galaxy so that it is always directed along the z-axis, then plotting the new xy plane I obtain the face-on view of the galaxy itself.

3.3.2 Grid production

Once the rotation is performed, I divide the projected face-on view of each galaxy in a set of cells with an arbitrary resolution. First of all I need to face with the minimum length scale of the TNG50 simulation: 50pc/h. It is necessary to keep the cell grid resolution above a threshold value of three times 50pc/h, so 150pc/h which corresponds to about 220pc. In addition to that, it has to be enlightened that the spatially resolved MS (on sub-kpc scales) retrieved from observational studies is usually based on estimates of stellar mass and star formation rate surface densities ($\Sigma_\star$ and $\Sigma_{\rm SFR}$) within cells of about 500pc size ([Enia et al., 2020, Morselli et al., 2020]). Since this value is not below the threshold limit imposed by TNG50 resolution and since one of the goals is to extend what has been previously done with observations (Chapter 2), I decide to set the size of the grid cells to 500pc.
At this point to practically build up the grid I choose to limit the xy plane (with the galaxy face-on view) to the central region of the galaxy itself, within spatial ranges of [-15.0, 15.0] kpc on both x and y axes. Then, according to the assumed cell resolution, I divide the grid in 60 $\times$ 60 cells.
Moreover it has to be noticed that the galactic disk, including both the thin gaseous structure and the more ellipsoidal stellar distribution, has usually a limited height (of the order of hundreds of parsec). So, since I am considering face-on galaxies, I decide to constrain the galactic disk extension along the line of sight (z-axis) according to its height. To set this limitation I have to take also into account the minimum length scale of the simulation, as mentioned above, and the fact that I need a large enough number of particles (gas and stars) in order to have a good projection on the xy plane of the relevant quantities. As a consequence I select only particles within a range of [-2.0, 2.0] kpc along z-axis, which is a very conservative estimate of the galactic disk extension.
Therefore, for what has been said so far, the grid that is built starting from the centre of each galaxy lies on the mid-plane of the galactic slice with dimension: 30 $\times$ 30 $\times$ 4 $\rm kpc^3$.

3.3.3 Maps of stellar mass and SFR

In order to reproduce the spatially resolved distributions of the main quantities playing a role in the MS relation, stellar mass and star formation rate surface densities are needed.

PartType4 (stars)		
Field	Units	Description
GFM_StellarFormationTime		The exact time when this star was formed.
GFM_InitialMass	$[10^{10}$ $M_\odot$ $h^{-1}]$	Mass of this star particle when it was formed.

Table 3.6: These are the fields extracted from the TNG50 dataset to retrieve the time of birth and initial mass of star particles in a galaxy. `"GFM_StellarFormationTime "` is expressed in terms of the scale factor $a = 1/(1 + z)$ so it is adimensional; `"GFM_InitialMass"` is in units of $M_\odot$ over h multiplied by 10^{10}.

For what concerns the stellar mass, the procedure consists on summing up the mass of all the star particles, with the z-coordinate within [-2.0, 2.0] kpc, that fall into each cell of the grid just built up. Then to obtain the surface density I divide for the area of the cell itself: 0.25 kpc^2.
The treatment for the superficial density of SFR has an additional complication. The SFR reported for the single gas particle in the simulation (see the Field `"StarFormationRate"` in Table 3.5) is evaluated only on the physical properties of the gas itself through the Equation 3.1, explained in the paragraph 3.1.1. A SFR estimated in this way is then inversely proportional to a density-dependent timescale for star formation and it is proportional to the subgrid estimate of cold gas mass. Such a SFR is dubbed *instantaneous*, because it is just an initial estimation obtained simply enforcing the Kennicutt-Schmidt relation and it does not take into account the whole process of star formation. By the way to obtain a first picture of the SFR surface density, I sum up these instantaneous SFRs of the gas particles in each grid cell and then I divide for its area (analogously to what is done for the stellar mass), see Figure 3.2a. However it has to be noticed that this kind of SFR distribution may not be properly representative of the actual number and mass of stars that are forming per year in the simulation. Indeed it probably tends to overestimate SFR. So I decide to compute the SFR estimate in another way.
As anticipated in the paragraph 3.1.1, I consider stellar particles instead of gaseous ones, in order to trace the effective recently born stars. IllustrisTNG provides the instant of formation of each star particle in a galaxy and its initial mass. I can retrieve these information from the dataset fields shown in Table 3.6. Once I get the values of each of these fields, I convert the units of measure in physical ones. In this case I only need to convert the initial masses into units of $M_\odot$.
The ultimate goal is to reconstruct an estimate of SFR which is averaged over a timescale compatible with the ones used to calibrate the observational SFR indicators. As mentioned in paragraph 3.1.1, typically observational timescales are of the order of $\sim 10 \div 100$ Myr.
In this work I am dealing with SFRs evaluated in small galactic areas (0.25 kpc^2) and not with the global SFR integrated on the entire galaxy. So if I take a too short timescale over which the masses of the newly born stars are summed up, the spatially resolved values of SFR are likely to be smaller than its minimum resolvable value (SFR_{min}). In particular in galaxies regions where $\log SFR < \log SFR_{min}$ the simulation automatically gives as output: $SFR \equiv 0$, since it is unresolved. The exact value of SFR_{min} depends on the model, numerical resolution, and timescales over which the average SFR is measured. As a consequence, since the model and numerical resolution are already set by IllustrisTNG50 simulation, the choice of the proper timescale for this study has to be discussed. A possible option that can suit for my purpose is 500Myr, which is good because it respects the order of magnitude of

the observational indicators timescales, it minimizes the effects of the limited resolution and it also smooths out possible variabilities arising on smaller timescales [Sparre et al., 2015]. Once selected such a timescale, for TNG50 the minimum resolvable value for the averaged SFR is approximately $\log SFR_{min} \simeq -4.0$.
The next step is to practically build up the spatial distribution of the averaged SFR surface density. In each cell of the galactic grid I select only star particles that are born within the chosen timescale: 500Myr in lookback time, which corresponds to a scale factor of $a \simeq 0.966$ (according to the cosmological model assumed in [Planck Collaboration et al., 2016]). Then I sum up their birth masses in order to get the total stellar mass recently born in each cell and I divide it by the entire time range (500Myr) to obtain an estimate of the time-averaged SFR in units of $M_\odot/yr$. Finally I also divide this quantity by the area of the grid cell itself to get the surface density distribution of such SFR, see Figure 3.2b .
As an example, the Figure 3.2 shows both the grids of SFR surface density built following the two different approaches (instantaneous and averaged) explained so far.

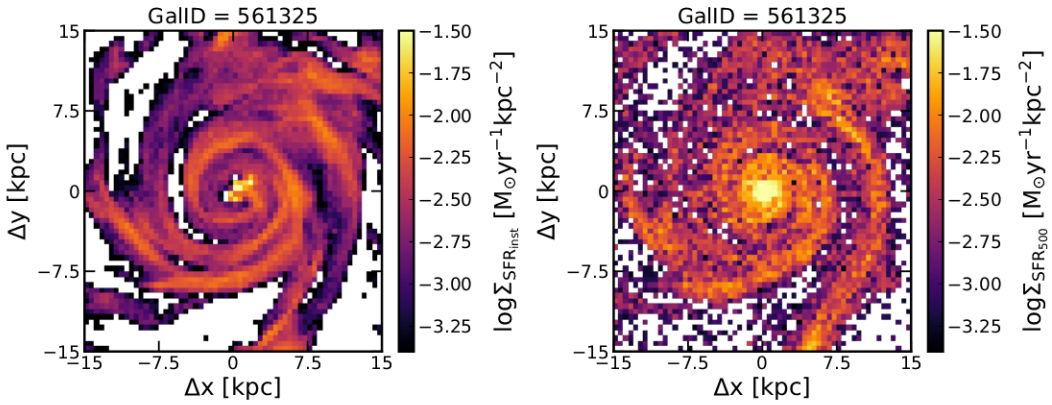

(a) Instantaneous SFR

(b) Time-averaged SFR

Figure 3.2: Spatial distributions of the instantaneous (a) and time-averaged (b) SFR surface densities of the unbarred galaxy with ID = 561325, from Sample 1. The former is based on gas particles and reproduces the Kennicutt-Schmidt relation. The latter, instead, considers star particles that are born in the last 500Myr. In both cases the values of Σ_{SFR} are reported in a logarithmic scale, as shown in the colorbar. The region that is plotted is the one within the range [-15.0, 15.0] kpc both in x and y axes.

At a first glance, it is evident that in Figure 3.2a there is a much better resolved view of SFR, with respect to the more discrete distribution in Figure 3.2b. Indeed this can be explained through the fact that the instantaneous SFR, given by IllustrisTNG50 (from Equation 3.1), is a proxy of the cold gas density distribution, once the efficiency factor $c_\star$ and the formation timescale t_{form} are set according to the KS relation. Hence it is able to map the stellar mass formed per year in a continuous way as if there would not have been a limit in resolution. It can be clearly seen that the spiral arms are well traced and actually they are the main host of star formation. However the grid shows also many blank spaces in which SFR $\equiv 0$, this is probably because in these cells gas particles are not eligible as star forming. Recalling the criteria set at the beginning of the paragraph 3.1.1, this pattern can be due to a combination of mainly two aspects: gas particles with low densities and/or found in more rarefied and hotter regions.
The grainy pattern in Figure 3.2b is related to the stochastic process of star formation. This fact is not necessarily an issue; it is actually more faithful to the observed spatial distribution of SFR, as can be seen in the ones obtained in the previous Chapter 2, where SFR is mapped through photometric data in UV and IR bands. In addition to that, at any fixed radius there

are cells with more homogeneous values of time-averaged Σ_{SFR} and this will produce a less scattered plot in the $\log\Sigma_\star$ - $\log\Sigma_{SFR}$ plane. Even in this grid there are some blank spaces spread around, which may be a consequence of: unsatisfied criteria that make a gas particle eligible for star formation, the actual probability that such a gas particle forms a certain stellar mass and the lowest limit of SFR imposed by the minimum baryonic mass that can be produced (SFR_{min}).
Considering all what has been discussed so far, the best decision is to perform the further analysis employing the time-averaged SFR surface density of our sampled galaxies.

3.3.4 Spatially resolved Main Sequence

Once prepared the spatially resolved grids of the stellar mass and SFR surface densities for all the sixteen galaxies belonging to Sample 1 and for all the twenty objects in Sample 2, the spatially resolved Main Sequence relation can be plotted. This latter is determined in the $\log\Sigma_\star$ - $\log\Sigma_{SFR}$ plane, through the implementation of the ODR (Orthogonal Distance Regression) technique. As it has been done for observational data (2.6.1), what is obtained is a linear relation between the logarithm of the involved quantities, written as:
$\log\Sigma_{SFR} = m \cdot \log\Sigma_\star + q$.
Finally this MS relation can be visualized reproducing a scatter plot where each point is representative of the $\Sigma_\star$ and Σ_{SFR} values related to each cell of the galactic grid. In addition to that, these points are coloured assigning to them the corresponding radial distance of the cell from the centre (in kpc). This enables to have a clearer view of the radial distribution of stellar mass and SFR in each analyzed galaxy.

3.3.5 Results

All the steps of the data analysis explained so far are repeated for all the galaxies in our two selected samples (Sample 1 and 2, Tables 3.3 and 3.4). In this section I expose the results related to: (i) three barred and three unbarred galaxies selected from Sample 1 and (ii) five barred and five unbarred galaxies selected from Sample 2. Plots related to all the other galaxies of the two samples can be found in Appendix B.
For each of galaxies I display the spatially resolved maps of $\Sigma_\star$ and Σ_{SFR} and the corresponding MS relation computed from them. It has to be noted that in the $\log\Sigma_\star$ - $\log\Sigma_{SFR}$ plane of all MS representations I plot the best log-linear relation fit obtained from the ODR regression and also the MS obtained for a sample of unbarred gran design spiral galaxies from DustPedia [Enia et al., 2020]. This latter, displayed as the black line in all the following figures, is expressed as Equation 2.3.

RESULTS: BARRED GALAXIES

This paragraph is devoted to the presentation of the results related to the case of barred galaxies. Figure 3.3 displays three examples from Sample 1 (lower masses), while Figure 3.4 shows five examples from Sample 2 (higher masses).

Spatially resolved distributions: stellar mass and SFR

Sample 1
The first and second sets of images (Figure 3.3a and Figure 3.3b) are the maps of stellar mass and of time-averaged SFR surface densities.
Stellar mass is more concentrated towards central areas of the galaxies, where the typical values of the mass surface density are around $10^{8\div9}$ $M_\odot kpc^{-2}$. Indeed a particularly defined spheroidal structure in the center (the bulge) is clearly evident and the bar appears grafted

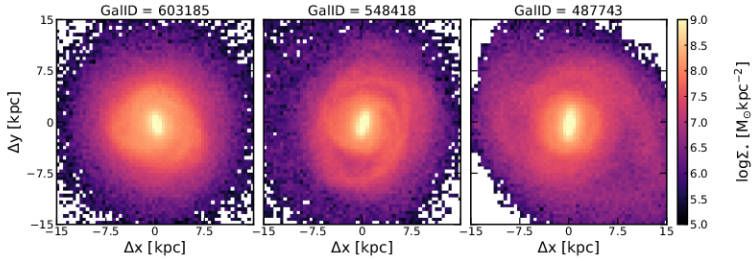

(a) Stellar mass surface density distribution

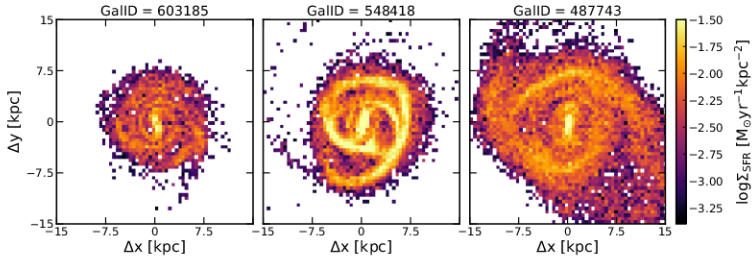

(b) Time-averaged SFR surface density distribution

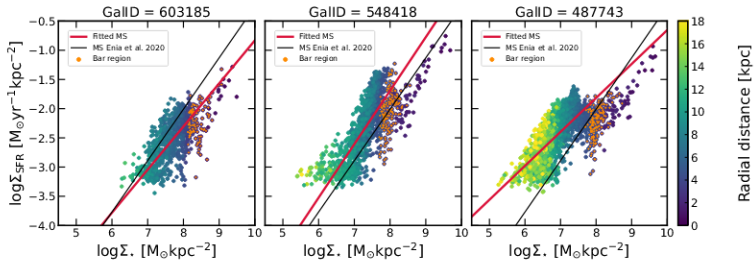

(c) Spatially resolved MS relation

Figure 3.3: Sample 1. Results related to three barred galaxies with IDs = 603185, 548418, 487743 from left to right. The main quantities $\Sigma_\star$ and $\Sigma_{\rm SFR}$ are expressed in a logarithmic scale, while in panel (c) the radial color code of data points is linear. In plots showing the spatially resolved MS, red and thicker lines are the best fit trends obtained from the ODR regression method, while black lines represent the MS relation expressed by the Equation 2.3 [Enia et al., 2020]. Orange dots correspond to the values of $\Sigma_\star$ and $\Sigma_{\rm SFR}$ in cells located in the bar region of each galaxy.

onto it. Actually, it is possible, in all these three galaxies, to glimpse the presence of an elongated structure that departs from the central bulge. It can therefore be concluded that the stellar component well traces the presence of the bar. From the maximum concentration of stars in the bulge, a progressive decrease in stellar mass towards the outermost regions is then observed. All this confirms the trend of exponential growth that the stellar mass follows if one proceeds from outside towards the inner part of disk galaxies. It is also possible to perceive the presence of spiral arms even though their surface mass density is lower than the one that characterizes the bulge region, hence they are less resolved. For what concerns the spatial extension of the stellar component, in Figure 3.3a it can be noticed that it is well within the limits that have been chosen for the xy plane ([-15.0, 15.0] kpc). Actually it is possible to recognize the outermost and less dense regions of the galaxies (darker cells) corresponding to the limits of their stellar disk. In addition it can be pointed out the fact that the rotation step of our analysis has succeeded in making them appear face-on, apart from some asymmetries (in particular concerning galaxies with IDs = 548418, 487743) that may be due to some external interactions or an ongoing process of disk particles redistribution, probably caused by the bar itself.

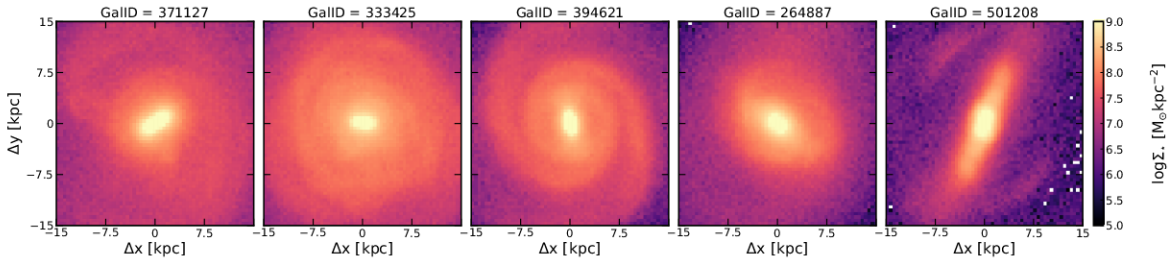

(a) Stellar mass surface density distribution

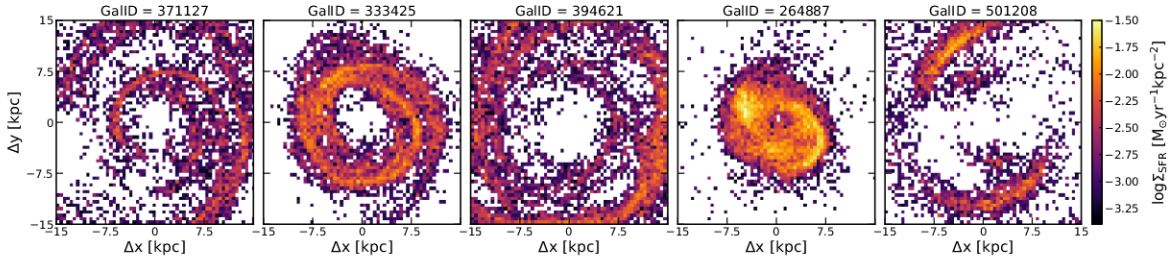

(b) Time-averaged SFR surface density distribution

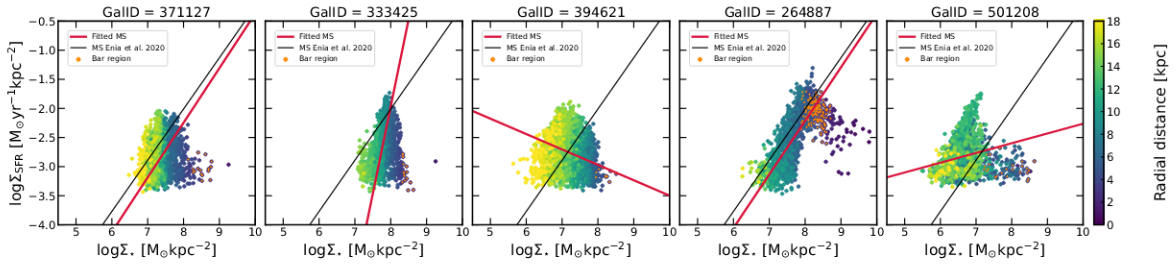

(c) Spatially resolved MS relation

Figure 3.4: Sample 2. Results related to five barred galaxies with IDs = 371127, 333425, 394621, 264887, 501208 from left to right. Same format as in Figure 3.3.

From the spatially resolved distributions of SFR shown below (Figure 3.3b), it is observed that it tends to have a slight increase going from the outer regions of the galaxies towards the inner ones. In particular it seems to trace the structures of the spiral arms, which actually host the star formation processes since it is in these regions that gas and dust are more concentrated. In fact spiral arms of the galaxy with ID = 548418 stand out with respect to the less star forming surroundings; this means that the galaxy is going through an active phase of star formation. In each of these three cases the SFR distribution points out the winding of the spiral arms that branch off from the edges of the bar structure. This feature is less evident in GalID = 603185, which has an overall more quiescent behaviour (its evolutionary path will be discussed in slightly more detail in paragraph 3.4.2). As already mentioned, an increase in the SFR is observed in the central structure, which is not spheroidal but elongated in the direction of the bar. This behaviour is especially prominent in GalID = 548148. On one side the presence of such higher star forming region in the centre is in a agreement with the expected relationship between stellar mass and SFR (Main Sequence), which states that the greater is the concentration of mass the more stars are produced. On the other side the elongation of this central active structure may be a signature of the gas redistribution process carried out by the bar itself, which is able to make the gas flow through it.
Another important aspect which arises from the visualization of these SFR maps is the fact that the region involved in star formation processes is usually extended within a limited radius and seems to have a sharp cut-off at the edges. Actually in these outer regions there is SFR $\equiv 0$, either because gas is very sparse and not star forming or because the newly born

stellar mass is below the minimum resolvable baryonic mass (which sets the limit SFR_{min} discussed in the previous sections).

Sample 2
Looking at the maps in Figures 3.4a and 3.4b, it can be said that most of the considerations previously done for the three barred galaxies from Sample 1 are valid also in these cases, however some differences have to be pointed out.
For example the stellar mass distribution is again more concentrated towards the centre, as it is expected in general for disk galaxies, and a well defined elongated structure comes out from the central region. Spiral arms are quite well traced too (e.g. GalID = 394621). Since these are more massive galaxies, it is reasonable the fact that the stellar disk turns out to be more extended than the one in the three less massive galaxies (Figure 3.3a). The galactic rotation step of the analysis appears to have been successfully executed, except for GalID = 501208, which probably has some peculiarities.
For what concerns the time-averaged SFR spatially resolved distributions, they are quite different with respect to the ones in Figure 3.3b. Actually in this case they trace the spiral arms winding but the central regions turn out to be almost completely quenched (except for GalID = 264887). These maps (Figure 3.4b) have a lot of cells in which the time-averaged SFR is basically zero, this probably means that in the last 500Myr not enough stars have been born (to overcome the minimum resolvable baryonic mass). This situation is quite common in more massive galaxies (also in some unbarred objects, see Figure B.4b): they typically have SFR maps with very sparse patterns, mimicking an almost quiescent phase (star formation is active only in very limited regions, e.g. spiral arms). Such feature can be attributed to a very rarefied distribution of gas particles in the disk, so that star formation cannot be triggered.
A possible explanation of this may lay on the implementation of some local processes that are responsible for the dissipation of gas. Since the main region that is experiencing a running out of gas is the central one, a mechanism that may act on such small scales is the AGN feedback, which is able to throw gas particles away during its phase of activity (disc accretion). Naturally also in smaller galaxies the eventual presence of massive black holes at the centre has similar effects but with a lower impact. Anyway it has always to be taken into account the fact that, in the simulation, this treatment follows an approximated approach and an effective comparison with observations is not completely feasible. Another hypothetical phenomenon that may play a role in this scenario is the feedback caused by Supernovae explosions, which may sweep away the gas and confine it in an outer halo. This would lead to the interruption of star formation activity, at least for a temporary phase. In addition to what has been said so far, also the influence of the bar structure is of particular relevance. Indeed, among the most massive galaxies (Sample 2), barred ones show a lower and less spatially extended quantity of gas, and then of SFR. Actually this seems to be in accordance with the initial assumption of the fact that the bar is highly involved in gas re-distribution processes.

Spatially resolved Main Sequence relation

Sample 1
The third set of images (Figure 3.3c) summarizes the spatially resolved trends of the MS relation corresponding to the analyzed galaxies. In all of these three cases data points are quite well distributed along a generally increasing trend, traced by the best fit red line evaluated through the ODR regression technique. The slopes of these three best fit lines are in agreement with the slope of the observed MS relation (Equation 2.3), in particular they tend to have a slightly lower value. Focusing on Figure 3.3c, evidently data points manifest also some discrepancies from the log-linear expected behaviour especially for what concerns the innermost regions of the galaxies, marked with darker colours. These are also the regions

that host the bar structures. In order to highlight these latter (excluding the very central part of the galaxy) I take the bar radius of each object and I select the points corresponding to the cells that belong to an annular region nearly centered on the bar radius itself. These points are then coloured in orange. It can be seen that in all the three cases most of these bar region points are below the red best fit line and are distributed along an almost vertical shaped pattern. This may be partly due to the intrinsic scatter of the points and partly to the presence of the bar itself that has the tendency to make SFR decrease in its surroundings. Moreover, looking more in detail at the single figures of panel (c), it can be found out that:

* In GalID = 603185 the SFR distribution appears to be limited in radius, hence the spatially resolved MS is computed on data points included within such a restricted region, as can be seen from the color-code (maximum radius of about 10 kpc). Even though there is this feature of central compactness, an increasing radial progression in SFR is observed going from higher to smaller radii. Points representing cells located within the bar radius tend to be slightly less star forming with respect to the predicted behaviour encoded by the red line. Generally speaking this galaxy seems to be in a more quiescent phase with respect to the other two and this can be perceived both by the darker aspect of the SFR map in panel (b) and by the lower extension of points in the MS towards the central more massive part.

* In GalID = 548418 the outer regions are again characterized by null SFR and the maximum radii reached are of the order of 12 kpc with some sparse points at larger radii. In this case the central points are well below the fitted MS but are representative of higher mass densities reaching a star formation maximum value of $\log\Sigma_{\rm SFR} \lesssim$ -0.5.

* In GalID = 487743 the log-linear growth of SFR surface density is smoother with respect to the previous cases. Points with higher radii are not symmetrically distributed around the red line and this fact is linked to a larger scatter both in stellar mass and in star formation. Indeed, as already mentioned, this galaxy does not appear perfectly circular within the considered spatial range. For what concerns the central points, they gradually cross the red line from higher to lower values of SFR, actually the overall distribution of points tends to bend in correspondence of the bar region (orange points). It then resumes the growth towards the central massive part, reaching values of $\log\Sigma_{\rm SFR} \lesssim$ -1.0.

Sample 2
Figure 3.4c shows rather irregular and diversified situations in the case of these five more massive galaxies. It has to be emphasized the fact that, because of the lack of SFR data in the central regions (which are the ones of interest in this analysis), it is difficult to handle and study the corresponding behaviour of these barred massive galaxies. Orange data points (the ones associated to the bar hosting region) and dark violet ones (the ones that sample the bulge) are almost absent in all the $\log\Sigma_\star$ - $\log\Sigma_{\rm SFR}$ planes of these galaxies, except for GalID = 264887. The latter is actually the only one that presents a more compact and still star-forming disk (Figure 3.4b). In this case the fitted MS has a trend which is very similar to the observed one [Enia et al., 2020] and it can also be recognized the anti-correlation track, associated to the bar structure, that has been found also in observational data and in the less massive galaxies of Sample 1.
For what concerns the other four galaxies, the only common feature that can be pointed out (and that has been already mentioned) is the globally quenched central region. In the majority of these cases the fitted MS can not even have a physical interpretation since the ODR technique failed to properly match the growth trend from outer to inner regions (because of the lack and scatter of data).

RESULTS: UNBARRED GALAXIES

In this paragraph I show of the results related to the case of unbarred galaxies. Figure 3.5 displays three examples from Sample 1 (lower masses), while Figure 3.6 shows five examples from Sample 2 (higher masses).

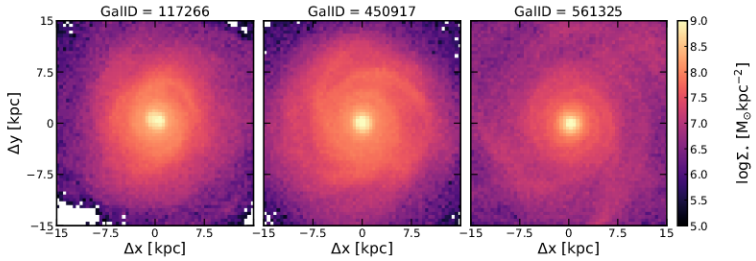

(a) Stellar mass surface density distribution

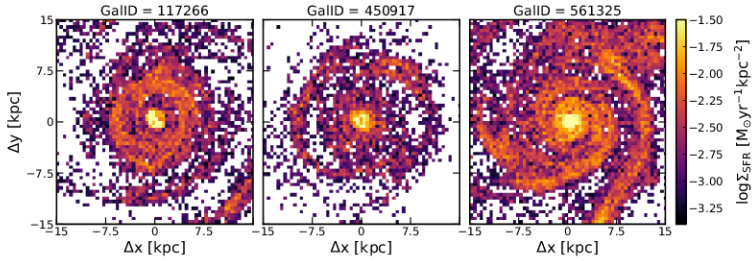

(b) Time-averaged SFR surface density distribution

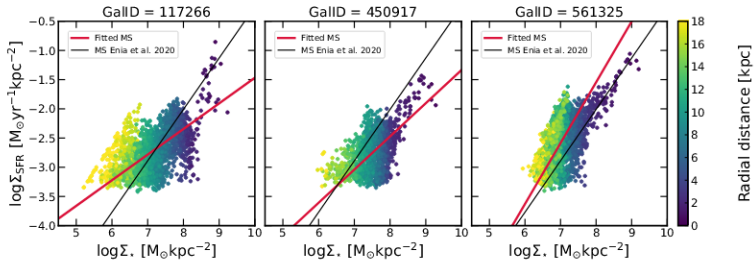

(c) Spatially resolved MS relation

Figure 3.5: Sample 1. Results related to three unbarred galaxies with IDs = 117266, 450917, 561325 from left to right. The main quantities $\Sigma_\star$ and $\Sigma_{\rm SFR}$ are expressed in a logarithmic scale, while in panel (c) the radial color code of data points is linear. In plots showing the spatially resolved MS, red and thicker lines are the best fit trends obtained from the ODR regression method, while black lines represent the MS relation expressed by the Equation 2.3 [Enia et al., 2020].

Spatially resolved distributions: stellar mass and SFR

Sample 1

The first and second sets of images (Figure 3.5a and Figure 3.5b) are the maps of stellar mass and of time-averaged SFR surface densities.

The description of these maps is analogous to what has been already done for the three barred galaxies (Sample 1) in the previous section. There is again an higher concentration of mass in the central regions with respect to the outskirts which are characterized by the thinner disk structure and spiral arms. These are not clearly evident, actually they are even less prominent than the ones in barred galaxies just described. However the winding of these spiral arms is at least perceptible and they finally converge towards the central bulge which

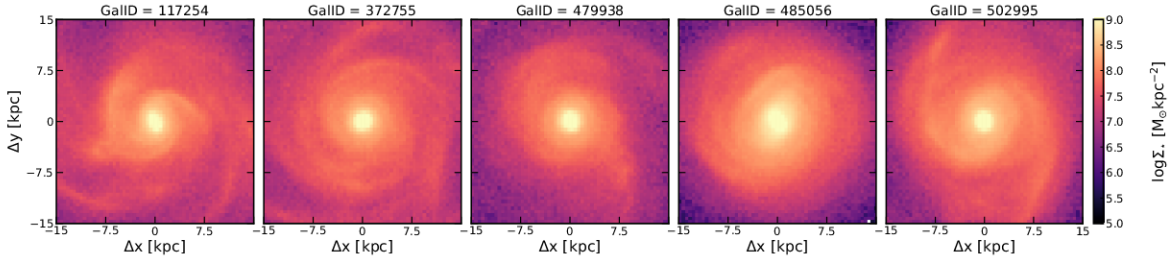

(a) Stellar mass surface density distribution

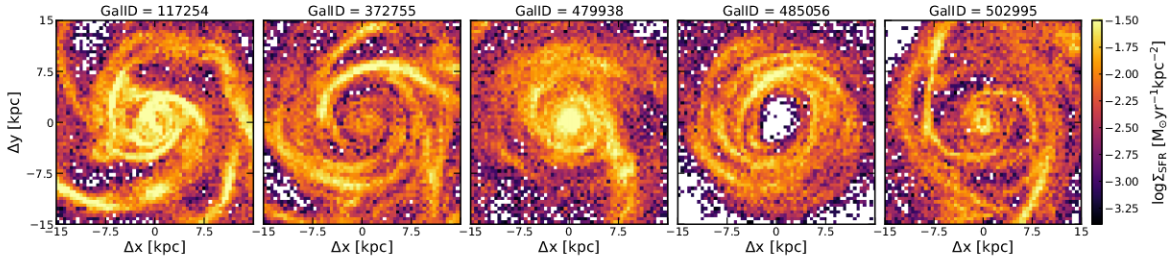

(b) Time-averaged SFR surface density distribution

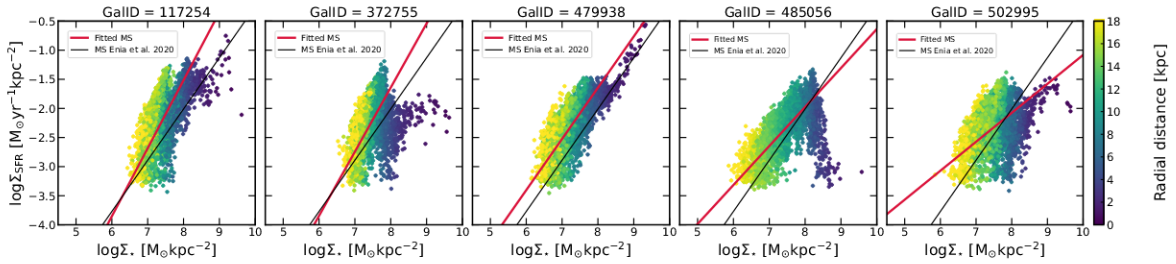

(c) Spatially resolved MS relation

Figure 3.6: Sample 2. Results related to five unbarred galaxies with IDs = 117254, 372755, 479938, 485056, 502995 from left to right. Same format as in Figure 3.5.

in this case is clearly spheroidal. A quite relevant difference with respect to the stellar mass distribution of barred galaxies is its spatial extension. Unbarred galaxies host a wider disk, indeed surface density maps cover all the considered portion of xy plane and seem to push their limits even beyond. This feature can be pointed out thanks to the fact that the limits in the range of $\Sigma_\star$ are the same as in the maps in Figure 3.3a.
Speaking about the time-averaged SFR surface density, the first thing to underline is the fragmented aspect of the maps. For these three unbarred galaxies a common feature is the strong activity of the bulge followed by a lower but evident star formation in spiral arms. The distributions in Figure 3.5b appear to be more spread out with respect to the typical compactness of the star forming disc in barred galaxies, they are however more rarefied and tend to have blank spaces also between spiral arms.

Sample 2
For what concerns the maps of stellar mass of these five more massive unbarred galaxies (Figure 3.6a), it can be noticed that they have almost the same characteristics as the ones just discussed: (i) growth of stellar mass concentration towards the centre, (ii) well defined winding of spiral arms branching off the bulge, (iii) wider disk.
On the contrary, the SFR spatially resolved distributions (Figure 3.6b) exhibit a distinct pattern with the respect to the fragmented maps of the three less massive galaxies (Figure 3.5b). Indeed these galaxies have generally higher values of SFR that emphasize the star formation activity mostly occuring in the spiral arms. In some cases also the nuclear region

appears to be active (e.g. GalID = 117254 and GalID = 479938). There is only one case that is characterized by a quenched central region: GalID = 485056. The situation is substantially different for the results related to the other five massive unbarred galaxies (Figure B.4b): here we have very different behaviours going from one galaxy to another, some of them display a compact highly star-forming disk, while some others have rarefied SFR distributions which seem to remark an ongoing quenching phase.

Spatially resolved Main Sequence relation

Sample 1
The third set of images (Figure 3.5c) collects the spatially resolved trends of the MS relation corresponding to the three analyzed galaxies. In all of these cases data points have an overall increasing trend, fitted by the red line computed through the ODR regression method. The slopes of these three best fit lines are not perfectly matching the slope of the observed MS relation (Equation 2.3), but they have comparable and tendentially lower values. Focusing on single cases shown in Figure 3.5c, it is possible to see that, in particular in GalID = 117266 and GalID = 450917, data points are intrinsically more scattered in the SFR direction. This comes as a consequence of what has been already said about the SFR surface density, in particular the part which deals with their strong fragmentation.
The points associated to the innermost regions of the galaxies are usually arranged above the fitted MS prediction, reproducing the strong star formation process which occurs in the bulge. Only the GalID = 561325 seems to partly diverge from this common trend, indeed in this case the central region is less star forming than expectations but it has to be said also that points are tightly correlated in a sharper log-linear relation. Data points at higher radii are generally placed above the best fit line and do not completely match the overall trend because of their significant scatter.

Sample 2
In Figure 3.6c there are the spatially resolved MS relations relative to the five considered galaxies. Analogously to what has been just said about the three less massive galaxies (Figure 3.5c), also in these cases the fitted data points show an overall increasing trend of the averaged SFR, with a slope that is comparable to one in Equation 2.3, with the exception of GalID = 502995 which seems to have a slower growth of the SFR as the stellar mass increases. Excluding the case of GalID = 485056, that presents an almost completely not star-forming nuclear region, the other plots in the $\log\Sigma_\star$ - $\log\Sigma_{\rm SFR}$ plane do not suffer the lack of SFR data (as previously seen for the barred galaxies in Sample 2). Therefore these MS relations are able to probe even the central regions, which manifest a star formation activity that is quite in agreement with the predicted trend (red fitted line), taking into account, however, that also other than bar quenching mechanisms may act in these internal regions (e.g. AGN and stellar feedback).

So far I have exploited a high-resolution hydrodynamical simulation (IllustrisTNG50) to perform a spatially resolved study of a sample of simulated galaxies at z = 0. In particular the first aim of studying the spatially resolved Main Sequence relation in a sample of barred galaxies, and in a corresponding control sample of unbarred galaxies (taken in two different mass ranges) has been achieved. Compatibly to its resolution issues and to the implementation of its subgrid physics mechanisms, the TNG simulation seems to be able to give a prediction of the bar structure role that is compatible with observations.
At this point it is interesting to retrieve the time evolution of the selected galaxies, in order to get a constraint on the bar role across cosmic time.

3.4 Time evolution of galaxies

In this section I go deep in the study of the galactic star formation properties along their evolutionary path. The purpose is (i) to retrieve the mean (integrated) Star Formation History for barred and unbarred galaxies, (ii) to analyze how the spatially resolved MS relation changes in time and which are the differences between what happens in a galaxy that forms a bar structure and another which does not.
In order to perform the spatially resolved analysis I select two galaxies from Sample 1, one barred and one unbarred, and I do the same for other two galaxies belonging to Sample 2. In particular I choose GalID = 603185 (Sample 1, Figure 3.3) and GalID (Sample 2, Figure B.2) = 523889 because, among the studied barred galaxies, they are the ones that better collect most of the characteristics of these kind of objects: the usual compactness of the star forming disc, the most homogeneous pattern of the SFR surface density (resembling what can be observed in the real Universe), the SFR decrement in the surroundings of the bar structure and the good match of the fitted MS with an increasing log-linear trend. About the choice of GalID = 117266 (Sample 1, Figure 3.5) and GalID = 479938 (Sample 2, Figure 3.6), as the representative unbarred galaxies, I can say that these objects seem to be a good compromise between what should be the expected MS trend and the ones I obtain studying the two sub-samples of unbarred galaxies. Indeed from a general comparison among all of them, it emerges that these ones have a more continuous distribution in the central region, which is the one of interest in order to understand possible differences with barred galaxies. From all of them I retrieve the IDs of their main progenitor branch through the SubLink algorithm implemented in the IllustrisTNG simulation.

SubLink

The SubLink algorithm constructs merger trees at the subhalo level. A unique descendant is assigned to each subhalo in three steps:

1) First of all descendant candidates are identified for each subhalo as those subhalos in the following snapshot that have common particles with the subhalo in question.

2) Second, each of the descendant candidates is given a score based on a merit function that takes into account the binding energy rank of each particle.

3) Third, the unique descendant of the subhalo in question is the descendant candidate with the highest score.

Once all descendant connections have been made, the main progenitor of each subhalo is defined as the one with the "most massive history" behind it. Thanks to that, it is possible to have access to information about the past history of each galaxy.

3.4.1 Main Progenitor Branch characteristics: integrated SFH

As a first step I want to visualize the time evolution of the SFR of all the galaxies in the two samples. To do so I need to select some fields from the dataset given as output of the SubLink procedure. In particular I list them in the following Table 3.7, these fields are referred to each subhalo identified in the main progenitor branches of all the galaxies.
Before going on with the further steps to retrieve the (instantaneous) SFR time evolution I convert the units of measure used by IllustrisTNG simulation into physical units.
Then I have ID and total (instantaneous) SFR of each main progenitor subhalo for all the snapshots available in the TNG50 simulation. These latter are 99 and they correspond to 99 redshift steps (from z = 0 to z = 20.05). For some galaxy it can happen that the needed information is not available at exactly all the 99 steps, in these cases the typically very limited

Field	Units	Description
SubfindID		Index of this subhalo in the Subfind group catalog.
SnapNum		The snapshot in which this subhalo is found.
SubhaloSFR	$[M_\odot\ yr^{-1}]$	Sum of the individual star formation rates of all gas cells in this subhalo.

Table 3.7: These are the main fields extracted from the `"sublink_mpb_GalID.hdf5"` file for each subhalo identified in the main progenitor branches of the two galaxies. `"SubhaloSFR"` is in units of $M_\odot$ over year.

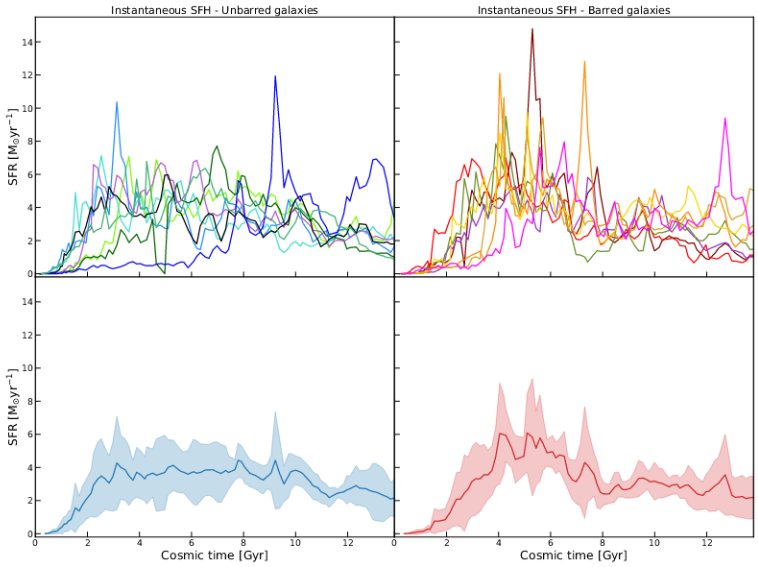

Figure 3.7: Sample 1. Evolution of the total (instantaneous) SFR as a function of cosmic time. In the upper panels the SFH is shown for all the galaxies (8 barred on the right and 8 unbarred on the left). The lower panels instead collect the mean SFH of barred galaxies (right) and the one of unbarred galaxies (left). Along with the mean trend, it is reported also a shaded area which represents the standard deviation from the mean value.

sample of snapshots that cannot be used are simply discarded. At this point I can reconstruct the SFR evolution of all the selected galaxies, starting from their origin up to the actual status. I show the evolutionary progress of galaxies belonging to Sample 1 in Figure3.7, dividing them between barred and unbarred galaxies (upper panels) and computing the mean SFH trend for these two kind of objects (lower panels). In the same way I display the integrated SFHs of objects in Sample 2 in Figure3.8, deriving also in this case the corresponding mean paths for barred and unbarred galaxies.
From Figure 3.7, it can be pointed out that the mean trend of the SFH in barred galaxies is not so different from the one in unbarred objects. Actually, after an initial phase in which the star formation activity is triggered (rapid increase of SFR), both the mean SFHs seem to settle down to an almost constant value of SFR in the last 8Gyr. The only difference that can be glimpsed out is the fact that in the mean SFH of barred galaxies a not so much pronounced peak in star formation appears between about 4 and 6 Gyr from the Big Bang. This probably corresponds to the phase of bar formation, during which this structure tends to trigger starburst events redistributing gas, stars etc.. Once the bar is seemingly fully established, the SFR starts to decrease (even if here the decrement is not so emphasized) as a

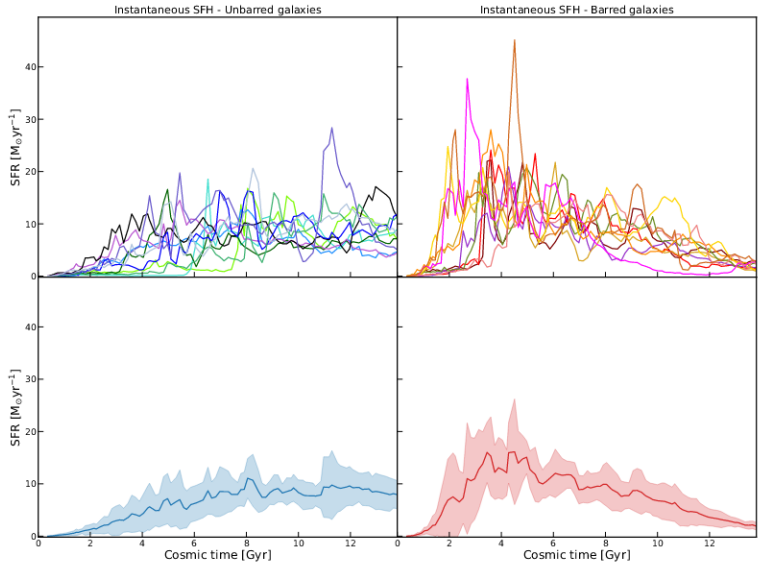

Figure 3.8: Sample 2. Evolution of the total (instantaneous) SFR as a function of cosmic time. Same format as in Figure 3.7.

consequence of the fast gas consumption, until it settles down to present values of SFR that are typically SFR $\sim 2M_{\odot}yr^{-1}$. The fact that these two situations are not so distinct one from the other is actually confirmed also by the plot in Figure 3.1, which refers to the actual (at z=0) integrated properties of the galaxies. Indeed one can notice that the green selected objects show values of SFR that are interchangeable between barred and unbarred galaxies. Actually the more evident dichotomy between barred and normal objects stands out at higher masses (where barred sources are also more numerous): galaxies that host a bar are systematically less star-forming (below MS) than unbarred ones (above MS), at z=0. This is clearly seen also in the final ends (present epoch) of the mean SFHs of galaxies belonging to Sample 2 (Figure 3.8). Besides that, in this case, also the two evolutionary progressions of the SFR values (one for unbarred massive galaxies on the left and one for barred objects on the right) have completely different characteristics. The mean SFH of barred galaxies shows a fast growth at early epochs that reaches a maximum of about $15M_{\odot}yr^{-1}$ at $\sim$4Gyr from the Big Bang. Afterwards a decline phase of SFR begins, until it stabilizes into the actual value of SFR $\sim 2M_{\odot}yr^{-1}$. On the other hand the total SFR of the unbarred massive galaxies shows a different time evolution: it has a slower phase of growth at early epochs and then succeeds in settling down to an almost constant value in recent times.
In order to further investigate the impact of bars on their host galaxies over time, it is more useful to exploit data from this latter sample of more massive galaxies, where the distinction between the two behaviours seems to be more pronounced. See Section 4.1.

3.4.2 Spatially resolved MS evolution

After a global overlook at the SFR time evolution in barred and unbarred galaxies, it is possible to give a qualitative description of the evolution in time of the spatially resolved Main Sequence relation.
As already anticipated, I perform this analysis on GalID = 603185 and GalID = 117266 from Sample 1 and on GalID = 523889 and GalID = 479938 from Sample 2.

Sample 1

For what concerns the two galaxies belonging to Sample 1, I select five significant time-steps across the whole history. In particular I choose: z = 0.1, 0.35, 0.82, 1.11, 1.25. I select these specific instants to probe the phases during which bar formation processes are probably going on (z = 0.82, 1.11, 1.25) and to study the more recent aspect of these galaxies (z = 0.1, 0.35). For all of these redshifts one retrieves the corresponding subhalo IDs, used to get access to the needed information to perform the spatially resolved analysis for these progenitors as already done for all the selected galaxies at z = 0 (see Table 3.5 and 3.6). The only difference in the implementation of the (already explained) analysis of these galaxies is the fact that the region used to evaluate the total angular momentum of gas particles needed to rotate the galaxies is restricted to a lower radius of 15kpc. This is because less evolved galactic disks are generally less extended. Finally I obtain five maps of stellar mass and SFR surface densities and five corresponding plots of spatially resolved MS relations for the selected main progenitors of GalID = 603185 and GalID = 117266. The relative results that we are going to describe in this section are collected in the three sets of images in Figure B.5 and Figure B.7 respectively (Appendix B).
Going into more detail of the case of the barred galaxy evolution (Figure B.5), it is possible to point out some interesting aspects:

1. The disk structure has almost reached its final extension already at z = 1.25. Looking at the stellar mass distribution, one can notice just a slight increase in the disc dimension going towards more recent epochs. This fact is not properly correlated in a proportional way with the net mass growth occurring during the earlier times. Indeed the increase of the stellar mass takes place mostly within a limited region around the galactic centre, without a consequent extension of the disc. This consideration comes out from the higher values of mass surface density progressively observed in the first set of plots (lighter and lighter colour of the central cells at decreasing redshift).

2. Such increase in the central mass assembly comes as a consequence of the star formation evolution. At the first considered step, one observes high values of $\Sigma_{\rm SFR}$ concentrated on spiral arms which are probably undergoing a phase of instability, given their irregular conformation. The peak of SFR is probably reached at z = 1.11, indeed there is a particularly active central region, from which a bar structure arises at subsequent epochs. After that, SF settles down to lower and lower values assuming a more stable configuration, up to the final stages where there are just a few very central cells with higher values of $\Sigma_{\rm SFR}$.

3. Following the evolution in time, the onset of the bar structure can be clearly perceived. In the initial phases there is just a small spheroidal bulge, then, after the epoch characterized by the peak of star formation, an elongated structure becoming more and more massive starts to be grafted on this. Such feature is well traced by the stellar mass, as expected, and also by SFR surface density, especially in its first stages of composition.

4. From both sets of mass and SFR maps, it is also possible to reconstruct how spiral arms evolve. After a more turbulent framework at higher redshift, they gradually tend to be wrapped in a more tight configuration branching off the edges of the central bar structure.

5. Spatially resolved MS plots come out from the combination of all the characteristics pointed out so far about the two main quantities involved ($M_\star$, SFR). It can be seen that at earlier epochs points are more tightly distributed around the best fit line obtained from the ODR procedure and they reach high values of $\Sigma_{\rm SFR}$ in the central massive region: $\log\Sigma_{\rm SFR} \gtrsim 0$. At these stages data points and their fitting line are well above the

observed MS relation evaluated for local unbarred spirals (black line [Enia et al., 2020]), mimicking the strongly active phase that the galaxy is passing through. Starting from the panel at z = 0.82, it can be noticed a sinking of points in the region corresponding to the newly formed bar structure. Then the overall distribution tends to go down to lower values of star formation and actually the fitted MS relation moves downwards and crosses the black line with a final lower slope. At these stages points also seem to assume a less linear trend with an increased dispersion around such smaller values of Σ_{SFR}.

For what concerns the unbarred galaxy evolution (Figure B.7) similar considerations can be made:

1. An interesting feature that stands out from the stellar mass maps is that in this case we have a net change in the extension of the disc through the evolution epochs. This is more consistent with the progressive overall mass assembly of the galaxy. Indeed the growth of the stellar mass surface density has the effect of widening the dimension of the galaxy feeding the disc structure. The central spheroid seems instead to maintain almost the same size and stellar mass.

2. Star formation maps have a divergent evolution with respect to the ones of the barred galaxy, where the star forming disc tends to assume a more and more compact structure going on in time. On the contrary, in this unbarred galaxy, at earlier times star formation processes are almost concentrated in a limited central region and are highly efficient. As time proceeds, such mechanisms start to be less strong and involve wider regions, until the phase during which the activity is mostly located along spiral arms. These latter are actually well traced by SFR maps, where it is evident that their winding becomes less tight going towards a lower redshift.

3. For what concerns spatially resolved MS plots, it can be seen that they follow a similar evolution with respect to the MS of the barred spiral. Indeed, at z = 1.25 and 1.11, points are closely concentrated along the best fit line (red). Then they start to assume lower SFR values and, as time passes, the slope of their fitting line becomes progressively smaller and finally crosses the observed MS relation (black line [Enia et al., 2020]). At these ultimate stages points are very scattered around the expected trend mainly because of the fragmented pattern of the SFR maps. In addition to that, from the radial color-coding of the points, it is clear the fact that star formation mechanisms are involving more the outer regions at the expense of the central ones, which instead turn out to be more quenched (darker points are below the red line).

Sample 2

To perform the spatially resolved study of the two galaxies taken from Sample 2 over time, I decide to increase the time-steps sampling in order to have a better view of their time evolution. This choice is based on the fact that, as already pointed out, more massive galaxies tend to have distinct evolutionary paths depending on whether they host a bar or not.
In this case I choose: z = 0.02, 0.07, 0.13, 0.21, 0.27, 0.38, 0.55, 0.73, 1.11, 2.00. The data analysis procedure is done following exactly the same steps as before (Sample 1) and the results related to these two objects (GalID = 523889 and GalID = 479938) are presented in Figure B.6 and Figure B.8.
The qualitative description of the various maps of stellar mass and SFR and of the evolution of the spatially resolved MS follows basically what has been said so far for the two galaxies in Sample 1.
In the case of GalID = 523889 the onset of a bar structure seems to occur at about z=0.73,

when a peak of SFR is reached (mostly in the nuclear region) and after which its star formation activity gradually decreases, until it turns out to be confined just in the outer regions of the galaxy (leaving an almost quenched central region). This trend is confirmed also by the distribution of points in the $\log\Sigma_{\star}$ - $\log\Sigma_{\rm SFR}$ plane: in the panels following the one at z=0.73 there is beginning to be a growing glimpse of a SFR decrease at the bar and bulge regions, this is very reminiscent of the anti-correlation feature identified in the barred galaxies from DustPedia.
Looking at the unbarred GalID = 479938, the star formation processes appear to be confined within a limited central area at earlier epochs and then they start acting on wider and wider regions of the disk going towards more recent epochs (spiral arms are well traced). The central bulge turns out to be particularly active in forming stars throughout all the time evolution, as it can be noticed also from the narrow distributions of the central points along (or near to) the fitted MS relation in the various time steps. The fact that the points associated to the circumnuclear region appear to be less star forming than what would be predicted at some specific epochs can be explained probably through the onset of transient quenching mechanisms like stellar feeedback, gas outflows from AGN etc..

Chapter 4

Discussions and Conclusions

In this final chapter of the thesis I go deep into the discussion of the bar quenching issue, establishing a comparison between the SFR decline found in simulated barred galaxies of Sample 2 (Chapter 3) and the Universe's star formation rate density evolution [Madau and Dickinson, 2014].
Besides this, I present some final remarks about the main results of this work and some possible future perspectives in order to further investigate peculiarities of barred galaxies.

4.1 Bar quenching

The Universe's cosmic star formation rate density (SFRD) peaked approximately 3.5Gyr after the Big Bang, at redshift $z \sim 1.9$, and then declined exponentially at later times [Madau and Dickinson, 2014]. The decreasing trend, which occurs in the range $0 \leq z \lesssim 2$, is parametrized by the relation:

$$\psi(z) \propto (1+z)^{2.7} \tag{4.1}$$

where ψ(z) is the best fitting function of the SFRD, in units of $M_{\odot}yr^{-1}Mpc^{-3}$. See Figure 4.1.
Such a decline is due to the combination of different mechanisms that act as quenching factors for the global SFR of a galaxy, for example: gas reservoirs depletion, decreasing number of interaction events among galaxies because of Universe expansion, AGN and stellar feedback, etc. (some other possible quenching mechanisms have been discussed in Section 1.3). What has to be remarked is also the fact that the major contribution (∼90%) to this SFRD is given by disk galaxies [Rodighiero et al., 2011] that evolve through secular processes (thus with a constant disk perturbation associated with a fairly stable rotation).
In particular, in this thesis work, I investigate how the quenching contribution given by the presence of bars affects the decreasing trend of the SFRD. As such, I put together observational constraints obtained from the DustPedia data analysis (Chapter 2), where an anti-correlation track in correspondence to the bar region has been revealed, with integrated SFHs and spatially resolved outputs derived from the analysis performed on IllustrisTNG data (Chapter 3), which turned out to be mainly consistent with observational ones, focusing especially on Sample 2 galaxies. Actually, as already pointed out in paragraph 3.4.1, the latter show a sharper difference between the evolution of SFR in barred galaxies and that of unbarred ones, thus highlighting the evidence of bar quenching.
To proceed with this treatment about bar quenching impact, I first produce a unique plot in which I display both the mean SFH of barred galaxies in Sample 2 and the mean SFH of unbarred ones (as found in paragraph 3.4.1), but with different units than in the previous

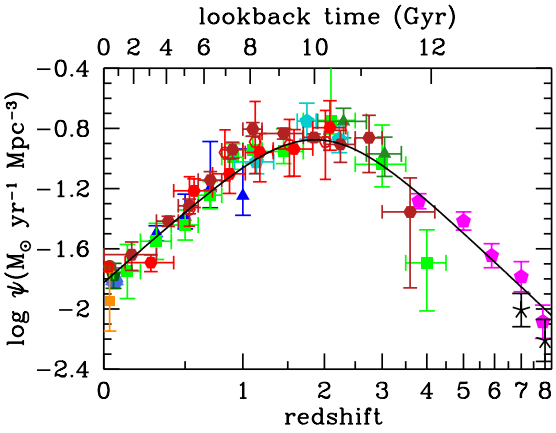

Figure 4.1: History of cosmic star formation in FUV+IR rest-frame measurements. Coloured symbols represent data, while the solid black curve is the best-fit SFRD. [Madau and Dickinson, 2014]

plot (Figure 3.8). Here (Figure 4.2) the trend of the SFR, in logarithmic scale, is depicted as a function of log(1+z), instead of cosmic time. This is done in order to retrieve a functional form that describes the SFR evolution of barred galaxies, in the interesting range $0 \leq z \leq 2$, in terms of $(1+z)^{\alpha}$, as it is already available for the SFRD [Madau and Dickinson, 2014]. This α-exponent is determined applying a linear fit of data in such log(SFR) - log(1+z) plane, being restricted within the range of redshift $0 \leq z \leq 2$, where the most of bar quenching seems to act. Indeed, it is exactly in this region that the sharp decline of SFR in barred galaxies shows up, while the SFH of unbarred objects appears to settle down to an almost constant (and higher) value. It is remarkable the fact that the SFR decrement in the evolution of barred galaxies occurs exactly in correspondence of the SFRD decline, thus in the range $0 \leq z \leq 2$.
The performed linear fit indicates that the decreasing trend of the SFR values in barred galaxies goes as:

$$SFR(z) \propto (1+z)^{2.03} \tag{4.2}$$

At this stage, a direct strict comparison between this fitted trend and the one found with observational data [Madau and Dickinson, 2014] cannot be properly established. This is due to the fact that, here, I am considering the SFR evolution of a typical (simulated) barred galaxy, while, in our Universe, they derived the SFRD, so the latter is rescaled in volume units too. In fact, this just introduces an offset in log(SFRD) values, so it can be neglected, since what is interesting is the slope of the SFR decline.
Net of what has been just pointed out, it can be noticed that the rate of the Universe's SFRD decline in the range $0 \leq z \lesssim 2$ (Equation 4.1) is comparable (slightly faster) to the one obtained through the fitting of the mean SFH of a sample of barred galaxies (Equation 4.2). This is confirmed also by the fact that, looking at the red curve (mean SFH of barred galaxies) in Figure 4.2 and at the best-fit SFRD in Figure 4.1, there is a factor $\sim$10 of SFR decline in both cases.
In the end, this discussion suggests that the role of bar quenching can be interpreted as one of the mechanisms that contribute to the global decline of SFRD (in Figure 4.1). However quantifying its impact is a challenging task, since it would be necessary to take into account the fact that not all galaxies host a bar structure and also that bars are transient phenomena during galaxy evolution.

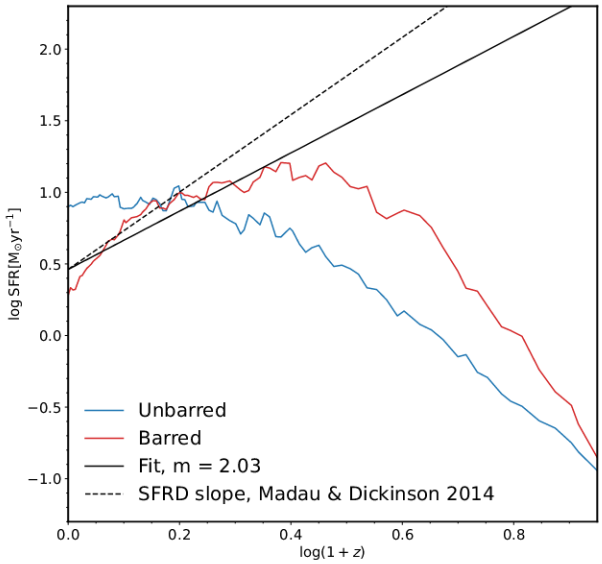

Figure 4.2: Mean SFH for barred galaxies (red curve) and unbarred ones (blue curve), belonging to Sample 2. Here the SFR is plotted in logarithmic units as a function of log(1+z). The black solid line represents the best linear fit performed on the SFR evolution of barred galaxies in $0 \leq z \leq 2$. It is reported also a black dashed line that is characterized by the same slope as the SFRD decline found in [Madau and Dickinson, 2014] and by an upwards shifted intercept, in order to provide an immediate visual comparison with the fit of our simulated data.

4.2 Final remarks

In this section I briefly summarize the main results of this thesis work.
From the first part of the data analysis, carried out exploiting the DustPedia dataset, I get that, statistically, all the ten selected barred galaxies show up an anti-correlation track in their spatially resolved MS that corresponds to the circumgalactic region hosting the bar. In addition, a bimodal trend in the bulge SFR is observed: in some cases bulges turn out to be almost quenched, while in some others the nuclear region is still active in forming stars. This traces the tendency that the bar has in either sweeping out the gas from the central regions, or funneling it towards the centre maybe also feeding the AGN. As a consequence this sort of quenching track and this bimodal behaviour of the nucleus may give some hints on the evolutionary stage of the bar structure.
The spatially resolved outputs related to IllustrisTNG data have a good agreement with observational ones, actually the decrement of SFR in the bar region is usually detected also in this case, even though a larger variety of situations comes out. Indeed, sometimes quenched central regions are present in unbarred galaxies too (this can be observed also in some sporadic normal galaxies from DustPedia, e.g. NGC0628), therefore there are probably other mechanisms that quench the star formation activity, like the AGN feedback.
From integrated properties of the parent sample [Rosas-Guevara et al., 2022], it has been pointed out that barred, less star-forming galaxies are more numerous at higher masses, thus bending the integrated Main Sequence (Figure 3.1). A further aspect that can be checked is if there is consistency between integrated properties of galaxies from IllustrisTNG and the ones of observed objects, in the log$M_\star$ - logSFR plane. This is displayed in Figure 4.3, where all the data points related to the IllustrisTNG parent sample are reported with shaded colors, while observed galaxies are denoted with a star-shape marker. In particular, as observational data, I plot: (i) the integrated properties of the DustPedia barred galaxies (employed in this work) with $M_\star > 10^{10} M_\odot$, in order to probe just the range of masses of IllustrisTNG

data; (ii) the integrated properties of the DustPedia normal galaxies from [Enia et al., 2020] with $M_\star > 10^{10} M_\odot$ (according to [Nersesian et al., 2019] results). Although the sample of observed galaxies is very limited, it can be easily seen that the integrated MS from simulated data is consistent with total SFR values of observed objects. Indeed, the latter have a similar distribution scatter with respect to the simulated ones and they trace also the fact that galaxies with the lowest values of SFR are barred. Along with the best-fit MS relations obtained for unbarred (blue line), barred (red line) and the whole simulated sample of galaxies (black solid line), I also display the SFMS relation (black dashed line) for observational data computed by [Renzini and Peng, 2015]: $\log(SFR) = (0.76 \pm 0.01)\log(M_\star/M_\odot)$ - 7.64 ± 0.02 .

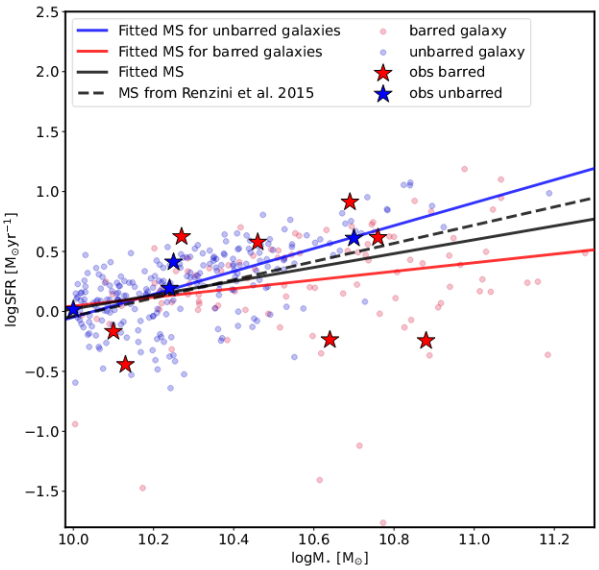

Figure 4.3: Same format as in Figure 3.1, but here observational data points are added (star-shape markers): red stars represent some of the barred galaxies analyzed in this work (Chapter 2), while blue stars portray some of the normal spiral galaxies of a literature work [Enia et al., 2020]. The black dashed line is the SFMS obtained by [Renzini and Peng, 2015].

Finally, thanks to the time evolution procedure performed with the IllustrisTNG simulation data, it has been confirmed the fact that the bar structure contributes to the SFR decline of its host galaxy. In particular the SFR of barred galaxies evolves as described by Equation 4.2, in the redshift range of interest. On the other side unbarred galaxies maintain an almost constant value of SFR in $0 \leq z \leq 2$.

4.3 Future perspectives

Starting from the aforementioned results of this thesis work, there are several aspects that could be further explored in some eventual future follow-up works.
For example, it would be interesting to study if the fact that the anti-correlation track corresponding to the bar region shows different slopes in different barred galaxies can be an indicator of the evolutionary stage of the bar itself, thus of the quenching phase that the host galaxy is undergoing in the inside-out quenching scenario [Tacchella et al., 2016].
Moreover one could study more in detail if this feature arises also because of other quenching mechanisms, e.g AGN feedback (like bars, they are transient events during the galaxy lifetime). Therefore, one could analyze a sample of galaxies hosting AGN in order to verify if such a central depletion in SFR is observed too.
Another aspect that could be useful to be taken into account concerns the time of bar for-

mation, which can be derived exploiting the power of cosmological simulation. Indeed bars can form in different epochs and this could affect the SFH trend, which correlates with the bar strength, that in turn depends on the epoch of bar formation and on how much it has grown up.
Besides this, an additional follow-up work could consist in improving the statistics of this thesis work, thus using a larger sample of objects, in order to better constrain the trend of SFH in barred galaxies and to effectively quantify the impact of bars onto the global decline of SFRD (parametrized by [Madau and Dickinson, 2014]) within $0 \leq z \leq 2$. As already briefly mentioned in the end of Section 4.1, to do this some caveats have to be kept in mind:

* The fraction of barred galaxies (out of the total number of disk galaxies that mainly contribute to the SRFD [Madau and Dickinson, 2014]) seems to evolve with redshift. As already said in Section 1.4, it decreses up to z$\sim$1, then (for $0.5 < z < 2$) it turns out to settle down to an almost constant value of 10%. In fact these estimates, especially the ones at higher redshifts, are still uncertain, since, at high z values, bar classification suffers from band shifting, cosmological surface brightness dimming and spatial resolution.

* Bars are transient events across the whole evolution of galaxies, then one should include a sort of duty cycle for these structures.

Additionally, in the next future, it could be really intriguing to perform a spatially resolved analysis (analogously to what has been done in this work) on observational data related to galaxies at higher and higher redshifts, in order to get some more observational hints about the evolution of bars. Actually, for the time being, spatially resolved studies can be conducted in large numbers only for objects in the local Universe, while, at higher redshifts, the resolution and sensitivity of most of the nowadays available instruments allow these studies to be conducted only for small samples of galaxies. However, it is important to note that there are several worldwide projects, some already ongoing and some others in the works, which will have a revolutionary impact on the progress of astrophysical research. Among the most relevant ongoing projects, one cannot fail to mention the James Webb Space Telescope (JWST), that is the world's premier space science observatory and that has already started to provide us a huge amount of new incredible data. On the other side, the projects that are in the works, like the Square Kilometer Array (SKA) or the Extremely Large Telescope (ELT), will be completed within the next few years and will enable the construction of new instruments that will contribute to the development of increasingly innovative and high-performance research techniques. With these next-generation telescopes almost all aspects of astrophysics will be able to progress, indeed they will allow us to push further the observational limits that we have nowadays and, thanks to their extremely powerful resolutions, they will also be of crucial importance for the future of spatially resolved studies.

4.3.1 The James Webb Space Telescope

The James Webb Space Telescope (sometimes referred to as JWST or Webb, [4]) is a large space telescope for infrared astronomy in solar orbit. It will complete and extend the discoveries of the Hubble Space Telescope, indeed it has a coverage from the R-band of the visible all the way to infrared wavelengths (HST, on the other hand, essentially observed the Universe from the UV to the near IR), moreover it has a greatly improved sensitivity. The longer wavelengths that will be examined will enable Webb to look much more closely at the earliest cosmic epochs and to examine the (so far unobserved) formation of the first galaxies, as well as to look inside dust clouds, where stars and planetary systems form. The telescope is the result of an international collaboration between NASA, the European Space Agency (ESA) and the Canadian Space Agency (CSA). It has a 6.5m primary mirror and it was launched

on an Ariane 5 rocket from Kourou (French Guiana) in 2021. The JWST will study every phase of the history of our Universe, from the first bright flashes after the Big Bang, to the formation of solar systems capable of supporting life on planets like Earth, to the evolution of our Solar System. This telescope will also make possible to greatly expand the sample of spatially resolved galaxies at high redshift so as to enable increasingly meaningful statistics. Several innovative technologies have been developed for Webb, among them it is included a main mirror composed of 18 separate segments that, deploying after launch, composes a single large collecting surface. The mirrors are made of ultralight beryllium. Webb's main feature is a five-layer sunshade of the size of a tennis court, which is able to attenuate the Sun's heat and to provide stability to the considerable temperature fluctuations to which the instruments are subjected. The telescope's four instruments, cameras and spectrometers, are equipped with detectors capable of recording extremely weak signals. One instrument (NIRSpec) has innovative micro-obturators that, like small, programmable shutters, allow spectra to be selected during a simultaneous observation, ensuring up to 100 objects to be simultaneously analyzed in deep space. The JWST also has a cryogenic facility able to cool, down to a very low temperature of 7K, the mid-infrared detectors of another instrument (MIRI) so that they can properly operate. Thanks to the cutting-edge design technologies that have been employed in its construction, JWST is the largest and highest-performance telescope ever sent into the space and it will expand the pathways already opened in the Universe by the Hubble Telescope.

As already stated, thanks to JWST, spatially resolved analysis on high redshift galaxies will be feasible. Actually there are already some literature works showing that bar structures can be studied through a quantitative and spatially resolved approach even at high redshifts [Guo et al., 2022]. Look at the Figure 4.4.

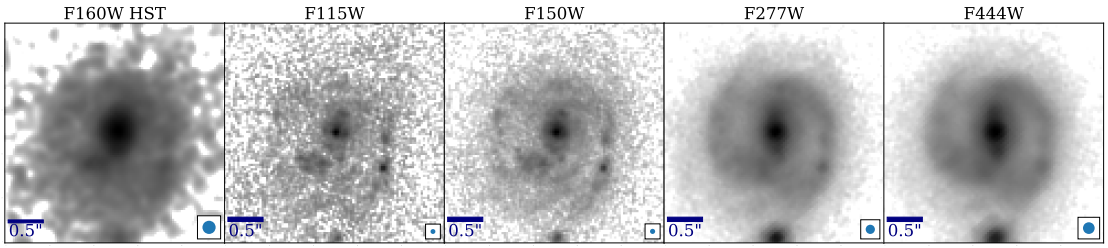

Figure 4.4: This figure depicts the effects of bandpass shift and PSF for a barred galaxy (EGS-23205) at redshift z $\sim$ 2.136. The images that are shown from left to right correspond respectively to: HST WFC3 F160W, and JWST NIRCam F115W, F150W, F277W, and F444W images. [Guo et al., 2022]

Finally, thanks to JWST data, one could also reproduce the integrated MS relation (analogous to the one obtained here for a sample of simulated barred and unbarred galaxies at z=0, Figure 3.1) at various redshift steps, reaching higher and higher values of z, for consistent samples of (real) barred and unbarred galaxies. In this way, one could test if bars are effectively able to impact on the MS tilting at the high-mass end, as it is found in Figure 3.1 for simulated galaxies at z=0. Moreover, thanks to the high redshift data, one could see also if bars eventually produce a stronger bending recently or at earlier epochs.

Appendix A

DustPedia: further results

Here I collect the main results, from the SED fitting analysis, of the other seven barred galaxies of the sample: NGC1097, NGC1365, NGC1566, NGC3953, NGC4321, NGC4579, NGC5248.

For what concerns the stellar mass spatially resolved distributions, all galaxies show a growth trend of stellar mass going from the outskirts to the internal regions, as expected. In particular a well-defined spheroidal structure stands out in the center (bulge) and the bar appears grafted onto it.

The higher values of the SFR surface densities are typically found in the spiral arms, while the bulge can turn out to be either particularly active in star formation (e.g. NGC1365) or almost quenched (e.g. NGC3953, NGC4579).

As a consequence, this already mentioned bimodality in the behaviour of the bulge can be easily pointed out also in the $\log\Sigma_\star$ - $\log\Sigma_{\rm SFR}$ plane, according to the distribution of the very central points with respect to the fitted Main Sequence relation. Besides that, the typical quenched feature, corresponding to the bar hosting region, is basically visible in all the selected galaxies, even if the slopes of such anti-correlating trend can be very different from one case to another. For example, in NGC4579 there is a strong evidence for this quenching track, while NGC1097 and NGC4321 show just a small decrement of SFR in that region.

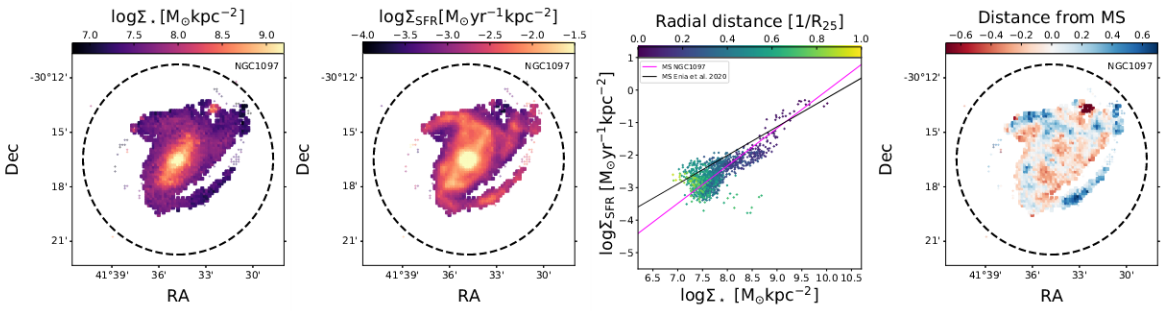

(a) (b) (c) (d)

Figure A.1: Summary plot for NGC1097. (a) Spatially resolved distribution of the stellar mass surface density. (b) Spatially resolved distribution of the star formation rate surface density. (c) Spatially resolved Main Sequence relation: the magenta line is the fitted MS (through the ODR technique), while the black line is the best fit MS obtained for a sample of normal galaxies [Enia et al., 2020]. (d) Cells distance from the fitted MS (magenta line in (c)).

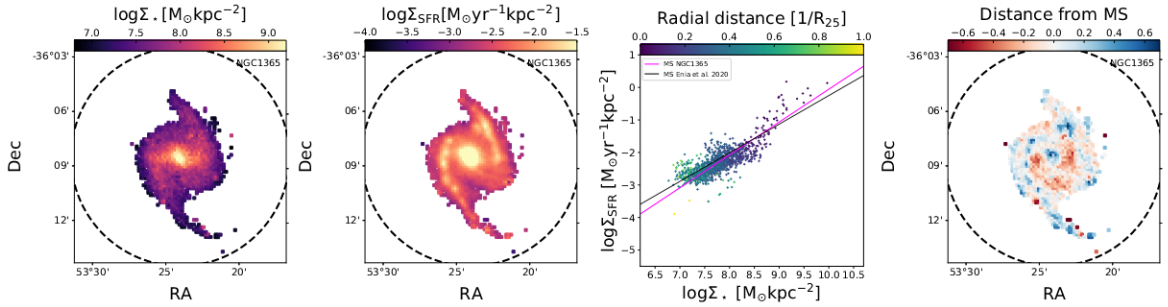

(a) (b) (c) (d)

Figure A.2: Summary plot for NGC1365. Same format as in Figure A.1.

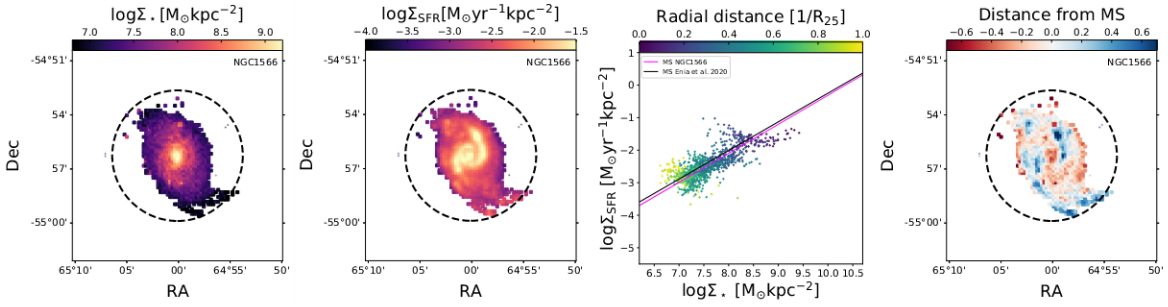

(a) (b) (c) (d)

Figure A.3: Summary plot for NGC1566. Same format as in Figure A.1.

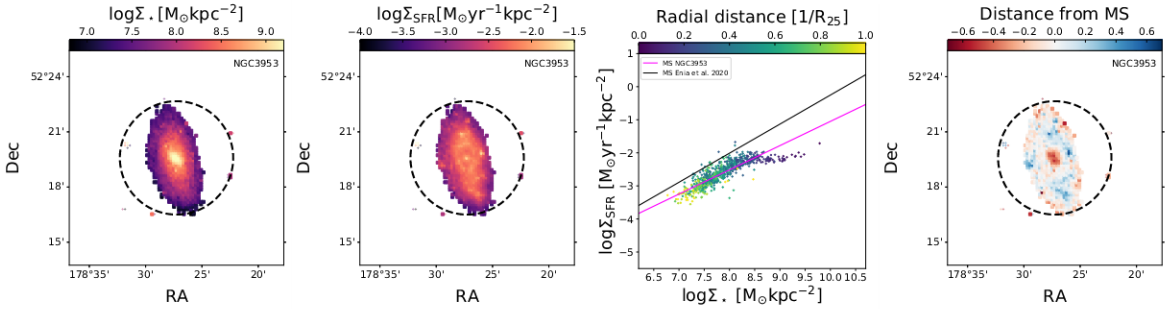

(a) (b) (c) (d)

Figure A.4: Summary plot for NGC3953. Same format as in Figure A.1.

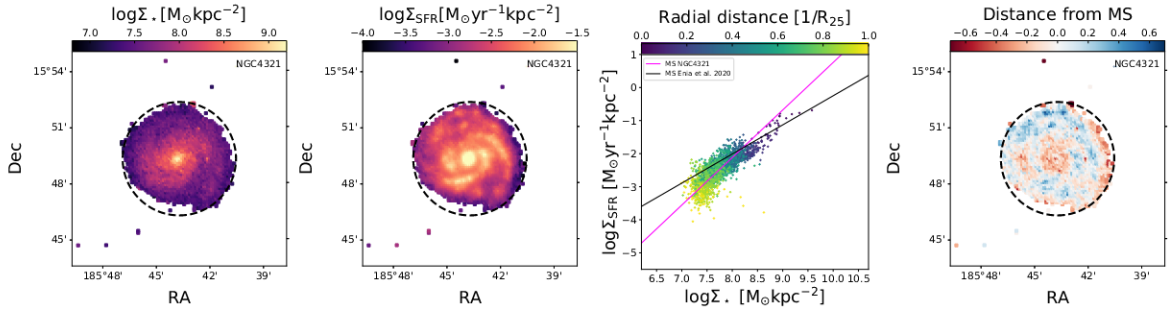

(a) (b) (c) (d)

Figure A.5: Summary plot for NGC4321. Same format as in Figure A.1.

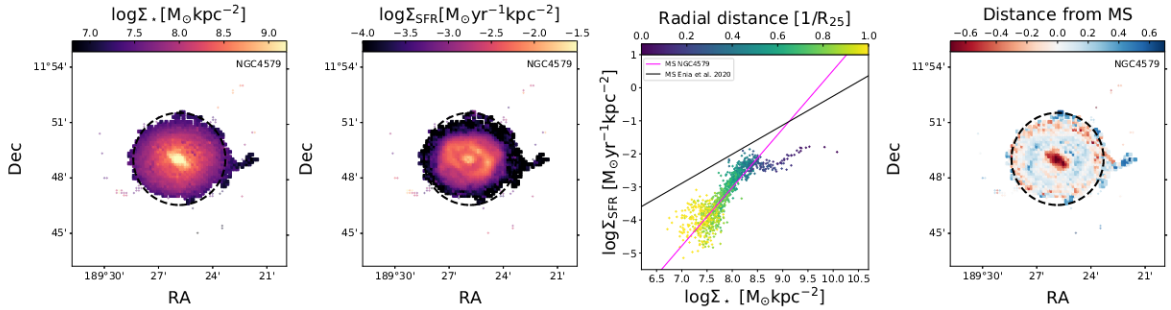

(a) (b) (c) (d)

Figure A.6: Summary plot for NGC4579. Same format as in Figure A.1.

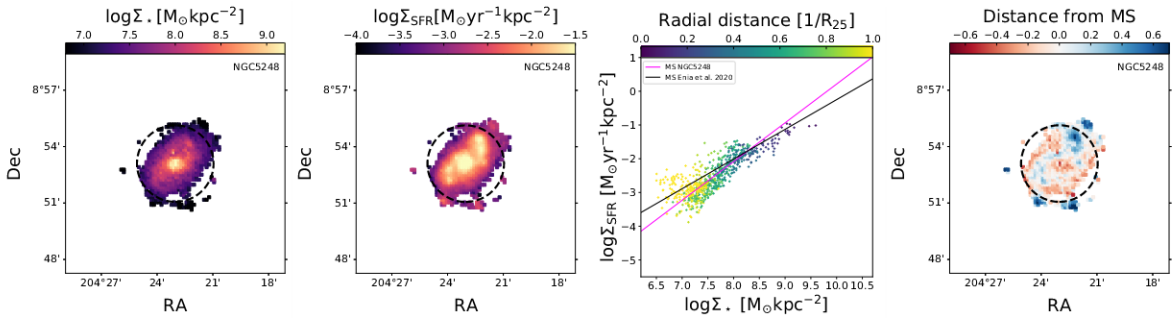

(a) (b) (c) (d)

Figure A.7: Summary plot for NGC5248. Same format as in Figure A.1.

Appendix B

IllustrisTNG: further results

In this Appendix I report the main results of the other barred and unbarred galaxies of Samples 1 and 2, from IllustrisTNG50 simulation. Afterwards I show the plots concerning the main progenitors of a barred and an unbarred galaxy belonging to Sample 1, and also of a barred and an unbarred galaxy in Sample 2. They are respectively: GalID = 603185, GalID = 523889 (barred) and GalID = 117266, GalID = 479938 (unbarred).

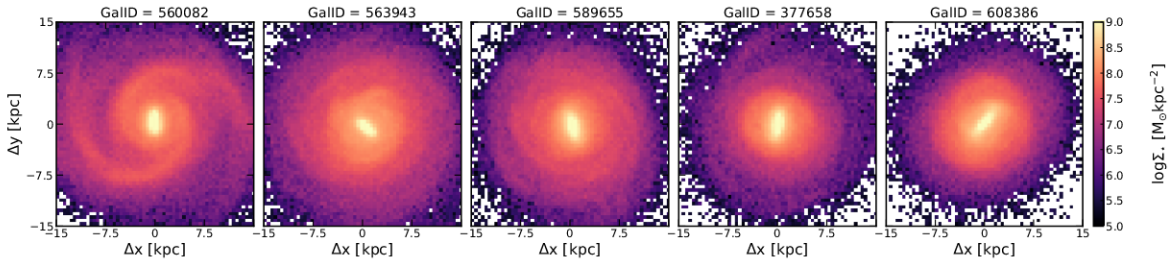

(a) Stellar mass surface density distribution

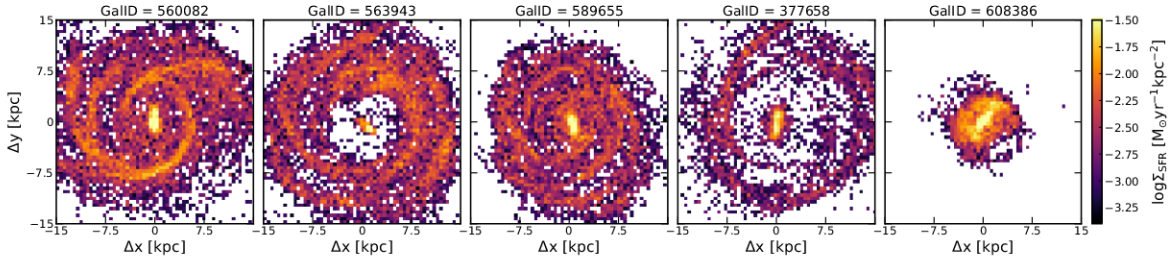

(b) Time-averaged SFR surface density distribution

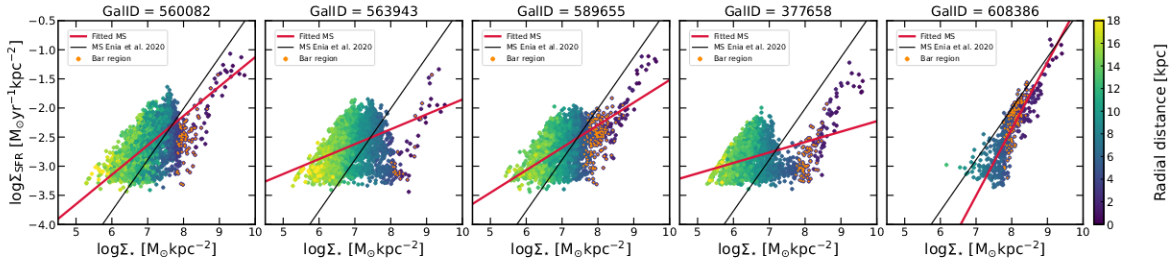

(c) Spatially resolved MS relation

Figure B.1: Sample 1. Results related to five barred galaxies with IDs = 560082, 563943, 589655, 377658, 608386 from left to right. Same format as in Figure 3.3

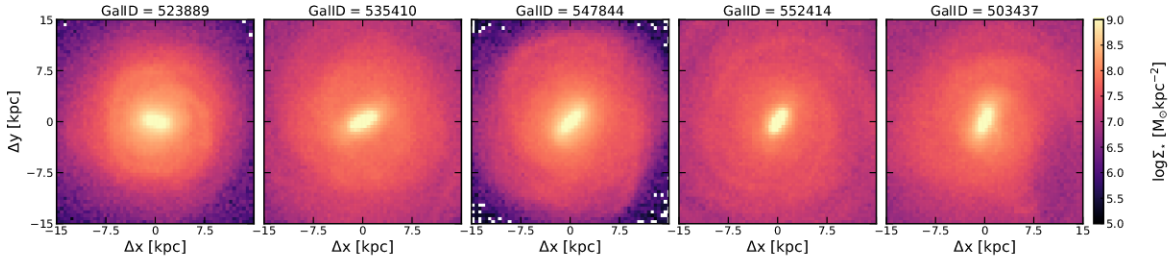

(a) Stellar mass surface density distribution

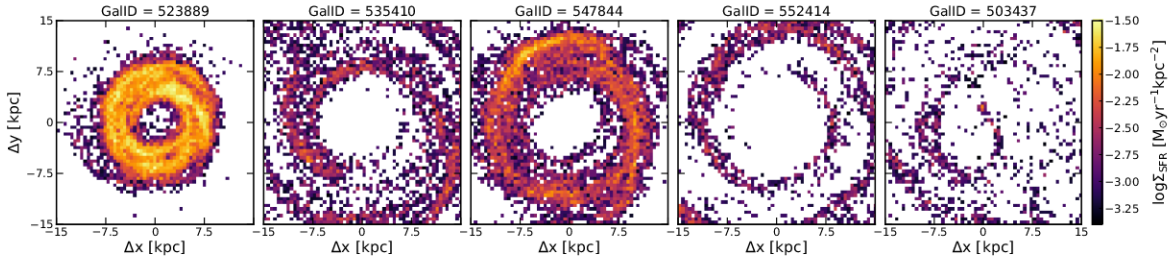

(b) Time-averaged SFR surface density distribution

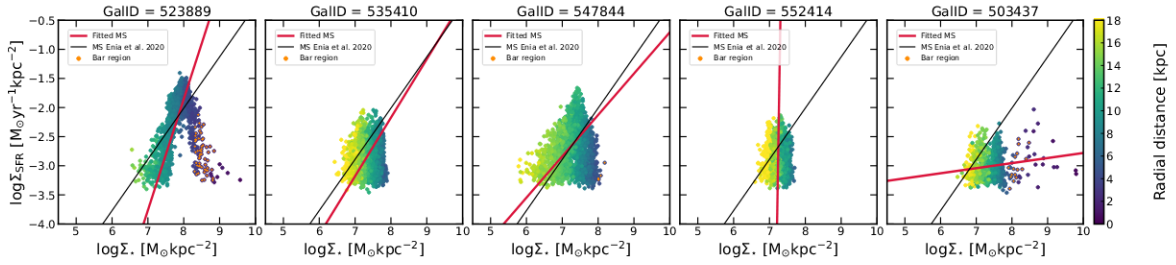

(c) Spatially resolved MS relation

Figure B.2: Sample 2. Results related to five barred galaxies with IDs = 523889, 535410, 547844, 552414, 503437 from left to right. Same format as in Figure 3.3.

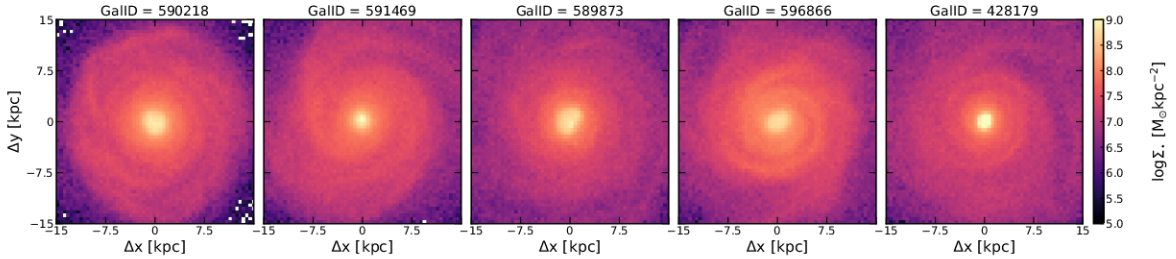

(a) Stellar mass surface density distribution

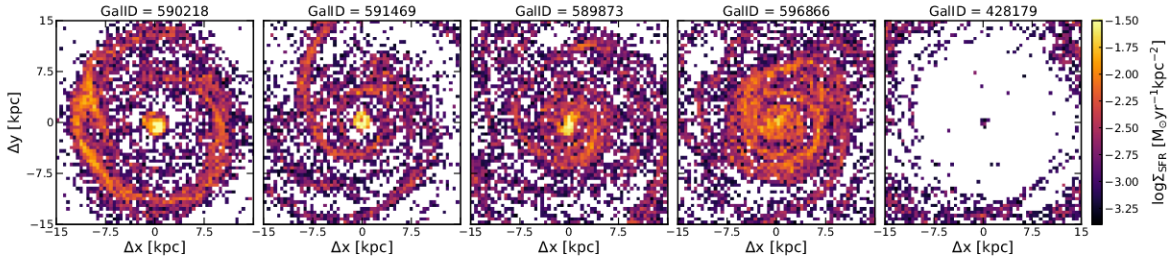

(b) Time-averaged SFR surface density distribution

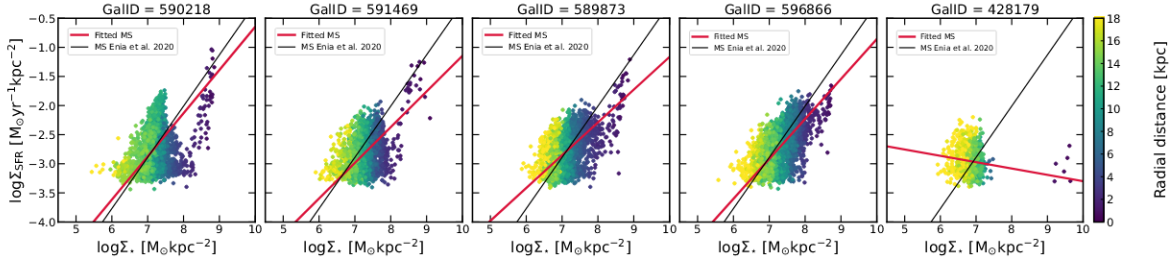

(c) Spatially resolved MS relation

Figure B.3: Sample 1. Results related to five unbarred galaxies with IDs = 590218, 591469, 589873, 596866, 428179 from left to right. Same format as in Figure 3.5

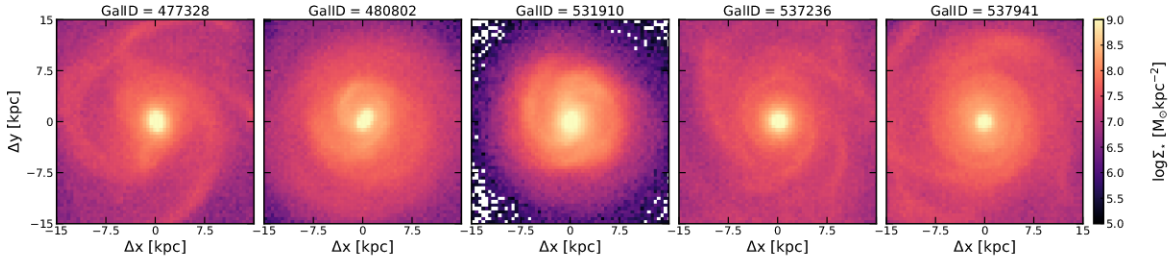

(a) Stellar mass surface density distribution

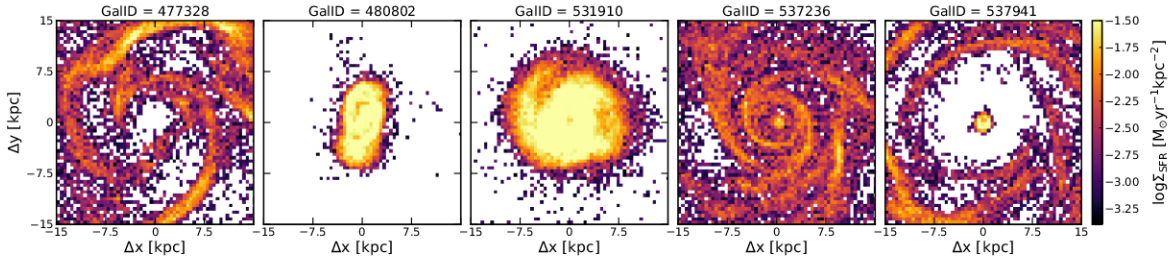

(b) Time-averaged SFR surface density distribution

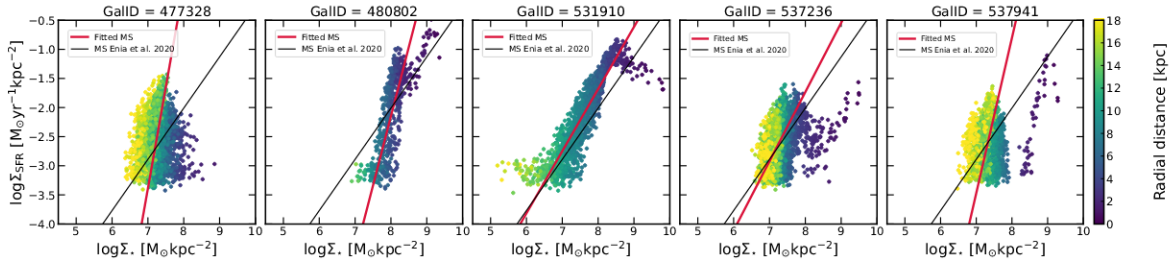

(c) Spatially resolved MS relation

Figure B.4: Sample 2. Results related to five unbarred galaxies with IDs = 477328, 480802, 531910, 537236, 537941 from left to right. Same format as in Figure 3.5.

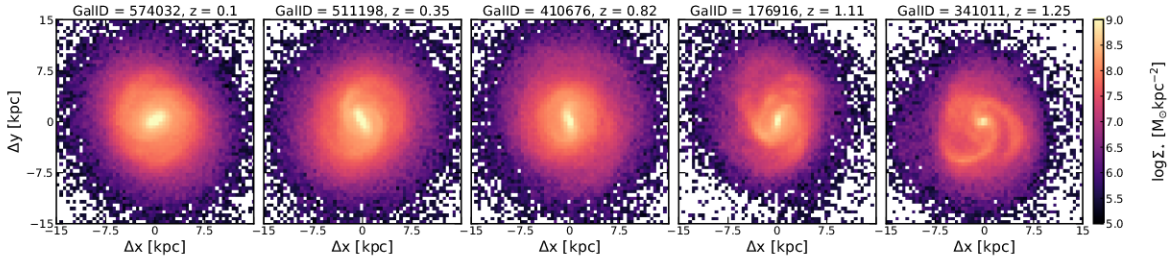

(a) Stellar mass surface density distribution

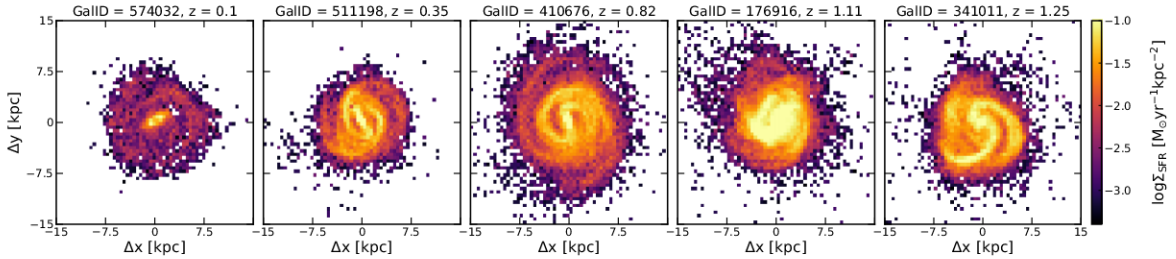

(b) Time-averaged SFR surface density distribution

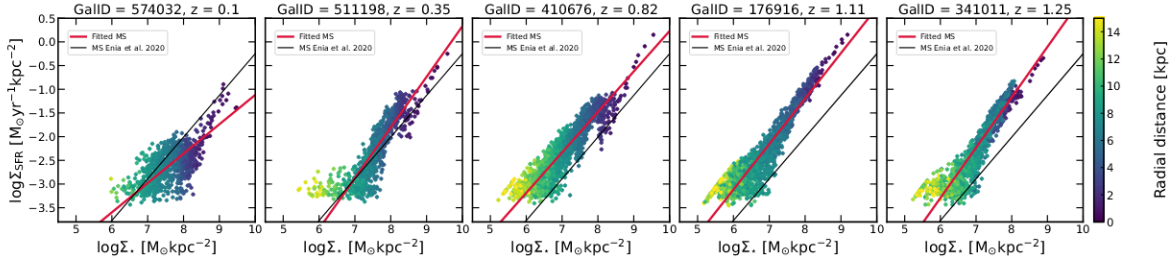

(c) Spatially resolved MS relation

Figure B.5: Time evolution of the main properties of the barred GalID = 603185 belonging to Sample 1. Same format as in Figure 3.3.

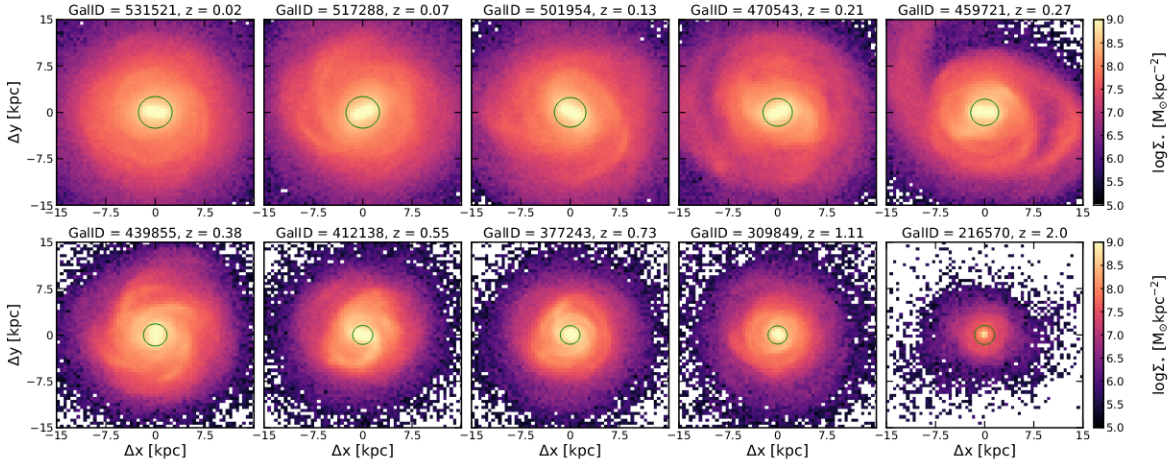

(a) Stellar mass surface density distribution

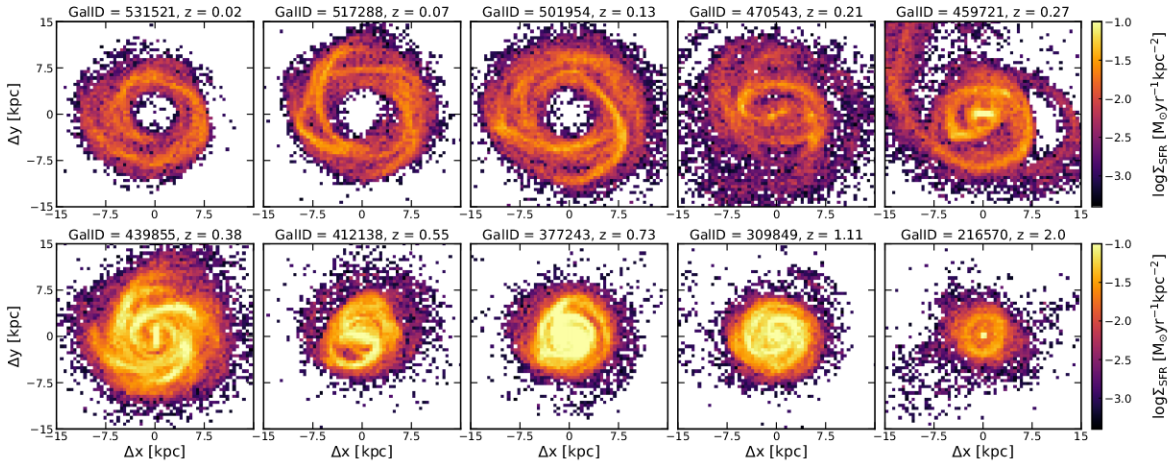

(b) Time-averaged SFR surface density distribution

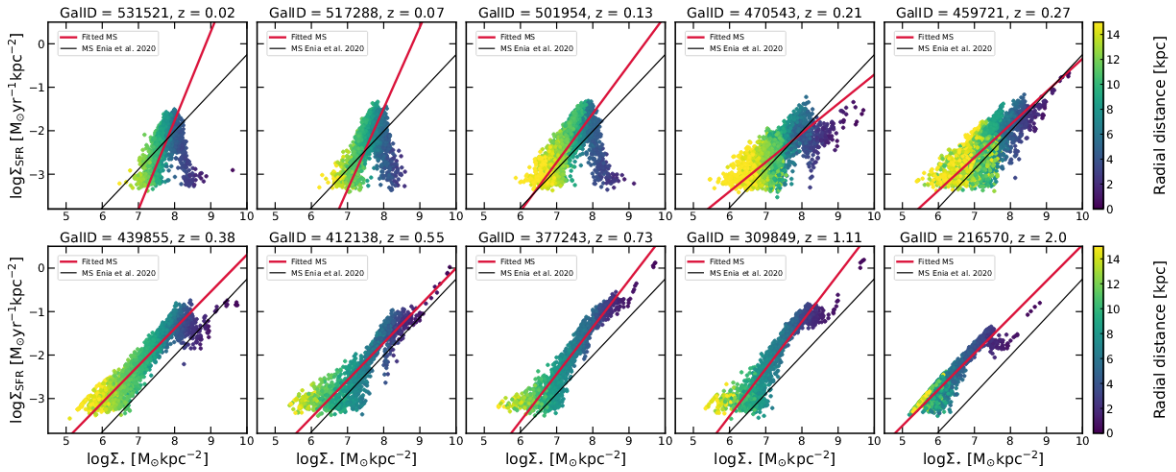

(c) Spatially resolved MS relation

Figure B.6: Time evolution of the main properties of the barred GalID = 523889 belonging to Sample 2. Same format as in Figure 3.3. The green circles shown in the stellar mass maps presented in panel (a) enclose the regions of radius equal to the stellar half mass radius at the various epochs.

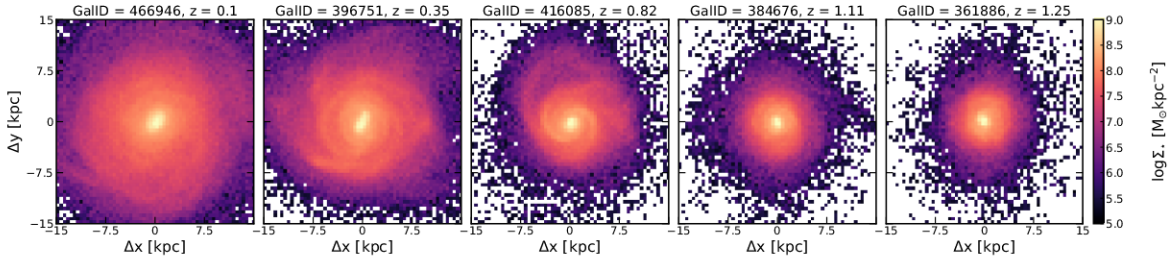

(a) Stellar mass surface density distribution

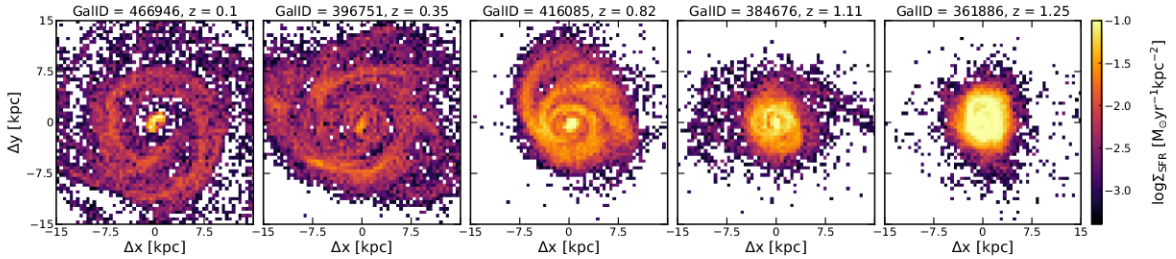

(b) Time-averaged SFR surface density distribution

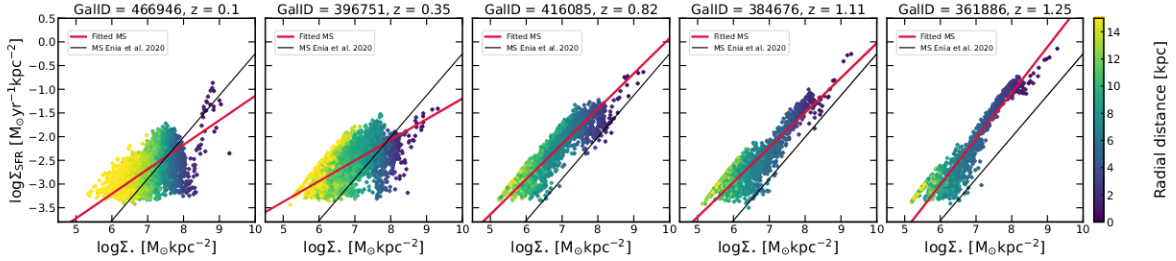

(c) Spatially resolved MS relation

Figure B.7: Time evolution of the main properties of the unbarred GalID = 117266 belonging to Sample 1. Same format as in Figure 3.5.

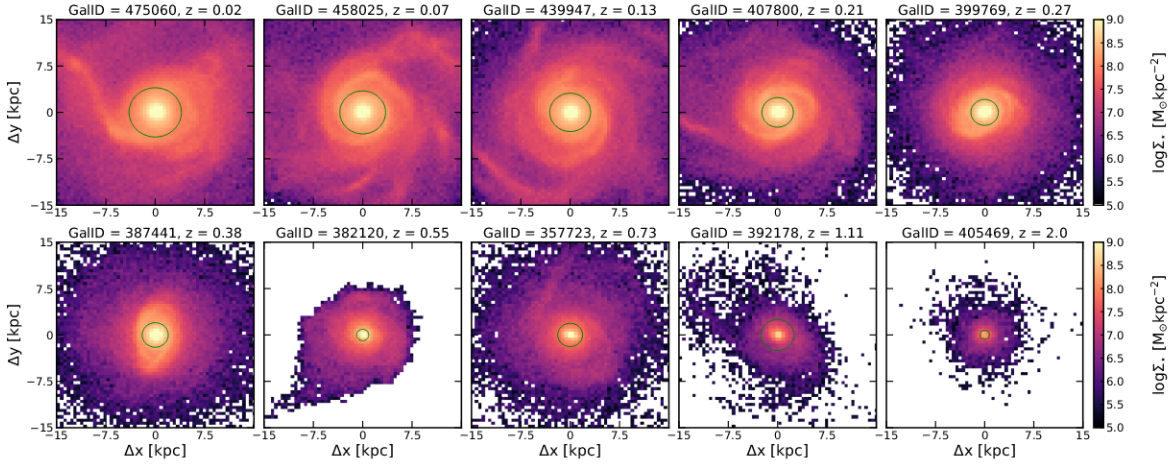

(a) Stellar mass surface density distribution

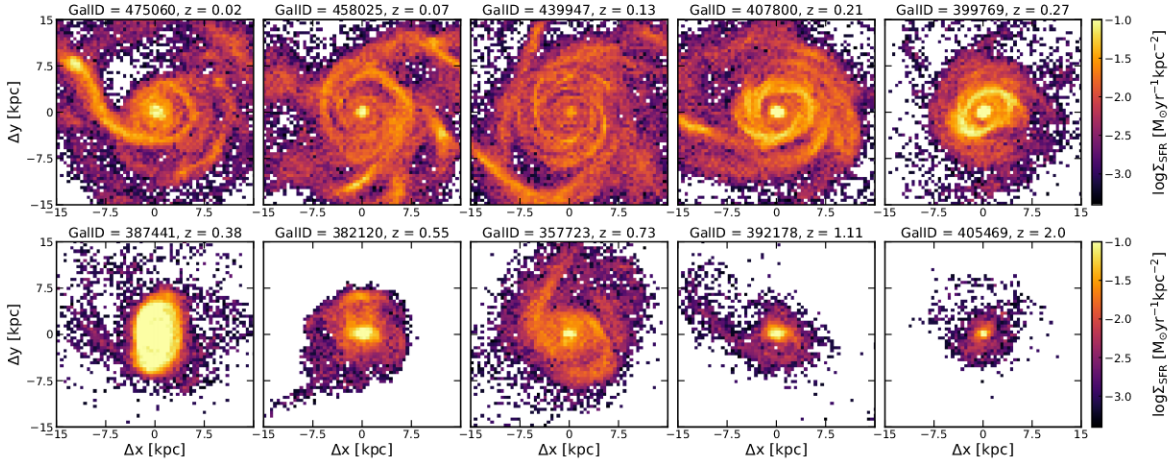

(b) Time-averaged SFR surface density distribution

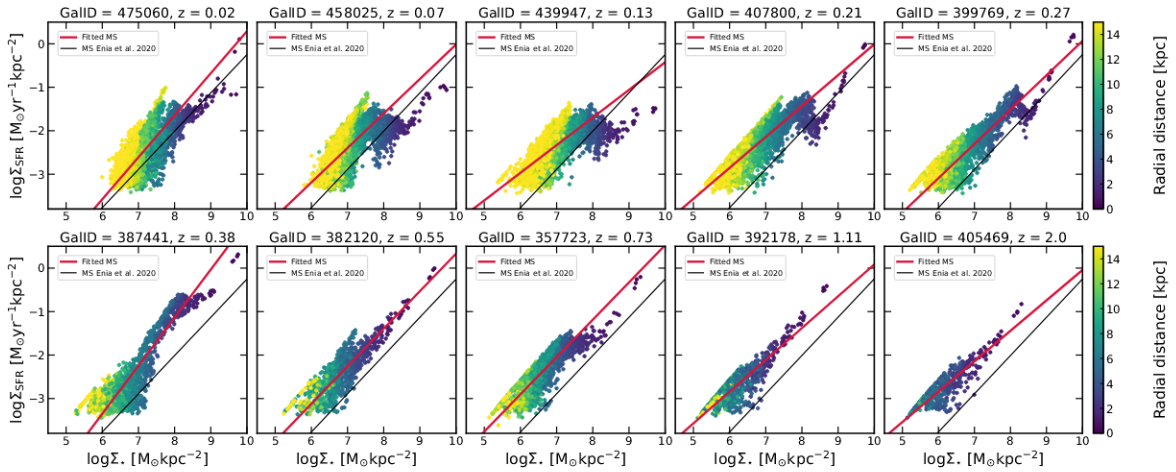

(c) Spatially resolved MS relation

Figure B.8: Time evolution of the main properties of the unbarred GalID = 479938 belonging to Sample 2. Same format as in Figure 3.5. The green circles shown in the stellar mass maps presented in panel (a) enclose the regions of radius equal to the stellar half mass radius at the various epochs.

Bibliography

[Abadi et al., 1999] Abadi, M. G., Moore, B., and Bower, R. G. (1999). Ram pressure stripping of spiral galaxies in clusters. *MNRAS*, 308:947–954.

[Abdurro'uf and Akiyama, 2017] Abdurro'uf and Akiyama, M. (2017). Understanding the scatter in the spatially resolved star formation main sequence of local massive spiral galaxies. *MNRAS*, 469:2806–2820.

[Aguerri et al., 2009] Aguerri, J. A. L., Méndez-Abreu, J., and Corsini, E. M. (2009). The population of barred galaxies in the local universe. *A&A*, 495:491–504.

[Athanassoula and Misiriotis, 2002] Athanassoula, E. and Misiriotis, A. (2002). Morphology, photometry and kinematics of N-body bars — I. Three models with different halo central concentrations. *MNRAS*, 330:35–52.

[Baldry et al., 2004] Baldry, I. K. et al. (2004). Quantifying the Bimodal Color-Magnitude Distribution of Galaxies. *ApJ*, 600:681–694.

[Balogh et al., 2000] Balogh, M. L., Navarro, J. F., and Morris, S. L. (2000). The Origin of Star Formation Gradients in Rich Galaxy Clusters. *ApJ*, 540:113.

[Bell and Kennicutt, 2001] Bell, E. F. and Kennicutt, R. C. J. (2001). A Comparison of Ultraviolet Imaging Telescope Far-Ultraviolet and Hα Star Formation Rates. *ApJ*, 548:681–693.

[Bongiorno et al., 2016] Bongiorno, A. et al. (2016). AGN host galaxy mass function in COSMOS - Is AGN feedback responsible for the mass-quenching of galaxies? *A&A*, 588:A78.

[Brinchmann et al., 2004] Brinchmann, J. et al. (2004). The physical properties of star forming galaxies in the low redshift universe. *MNRAS*, 351:1151–1179.

[Calzetti et al., 2010] Calzetti, M. et al. (2010). The Calibration of Monochromatic Far–Infrared Star Formation Rate Indicators. *ApJ*, 714:1256–1279.

[Cano-Díaz et al., 2016] Cano-Díaz, M. et al. (2016). Spatially-Resolved Star Formation Main Sequence of Galaxies in the CALIFA Survey. *ApJ*, 821:L26.

[Carles et al., 2016] Carles, C. et al. (2016). The mass dependence of star formation histories in barred spiral galaxies. *MNRAS*, 463:1074–1087.

[Chabrier, 2003] Chabrier, G. (2003). Galactic Stellar and Substellar Initial Mass Function. *PASP*, 115:763–795.

[Cimatti et al., 2019] Cimatti, A., Fraternali, F., and Nipoti, C. (2019). Introduction to Galaxy Formation and Evolution. From Primordial Gas to Present-Day Galaxies.

[Clark et al., 2018] Clark, C. J. R. et al. (2018). DustPedia: Multiwavelength photometry and imagery of 875 nearby galaxies in 42 ultraviolet-microwave bands. *A&A*, 609:A37.

[Consolandi et al., 2017] Consolandi, G. et al. (2017). Bars as seen by Herschel and Sloan. *A&A*, 598:A114.

[da Cunha et al., 2008] da Cunha, E., Charlot, S., and D., E. (2008). A simple model to interpret the ultraviolet, optical and infrared emission from galaxies. *MNRAS*, 388:1595–1617.

[Davies et al., 2017] Davies, J. I. et al. (2017). DustPedia: A Definitive Study of Cosmic Dust in the Local Universe. *PASP*, 129:044102.

[Debattista et al., 2006] Debattista, V. P. et al. (2006). The Secular Evolution of Disk Structural Parameters. *ApJ*, 645:209.

[Donnari et al., 2019] Donnari, M. et al. (2019). The star formation activity of IllustrisTNG galaxies: main sequence, UVJ diagram, quenched fractions, and systematics. *MNRAS*, 485:4817–4840.

[Dressler, 1980] Dressler, A. (1980). Galaxy morphology in rich clusters: implications for the formation and evolution of galaxies. *ApJ*, 236:351–365.

[Du et al., 2020] Du, M. et al. (2020). Kinematic decomposition of IllustrisTNG disk galaxies: morphology and relation with morphological structures. *ApJ*, 895:139.

[Eisenstein et al., 2011] Eisenstein, D. J. et al. (2011). SDSS-III: Massive Spectroscpic Surveys Of The Distant Universe, The Milky Way, And Extra-Solar Planetary Systems. *AJ*, 142:72.

[Elbaz et al., 2007] Elbaz, D. et al. (2007). The reversal of the star formation-density relation in the distant universe. *A&A*, 468:33–48.

[Enia et al., 2020] Enia, A. et al. (2020). A panchromatic spatially resolved analysis of nearby galaxies – I. Sub-kpc-scale main sequence in grand-design spirals. *MNRAS*, 493:4107–4125.

[Fraser-McKelvie et al., 2020] Fraser-McKelvie, A. et al. (2020). SDSS-IV MaNGA: The link between bars and the early cessation of star formation in spiral galaxies. *MNRAS*, 499:1116–1125.

[Galliano et al., 2018] Galliano, F. et al. (2018). The Interstellar Dust Properties of Nearby Galaxies. *ARA&A*, 56:673–713.

[Gavazzi et al., 2010] Gavazzi, G. et al. (2010). A snapshot on galaxy evolution occurring in the Great Wall: the role of Nurture at z. *A&A*, 517:A73.

[Gavazzi, 2015] Gavazzi, G. o. (2015). Hα3: an Hα imaging survey of HI selected galaxies from ALFALFA - VI. The role of bars in quenching star formation from z = 3 to the present epoch. *A&A*, 580:A116.

[George et al., 2019] George, K., Subramanian, S., and Paul, K. T. (2019). Significance of bar quenching in the global quenching of star formation. *A&A*, 628:A24.

[Géron et al., 2021] Géron, T. et al. (2021). Galaxy zoo: stronger bars facilitate quenching in star-forming galaxies. *MNRAS*, 507:4389–4408.

[Guo et al., 2022] Guo, Y. et al. (2022). First Look at z > 1 Bars in the Rest-Frame Near-Infrared with JWST Early CEERS Imaging.

[Hubble, 1926] Hubble, E. P. (1926). Extragalactic nebulae. *ApJ*, 64:321–369.

[Ilbert et al., 2015] Ilbert, O. et al. (2015). Evolution of the specific star formation rate function at z < 1.4 Dissecting the mass-SFR plane in COSMOS and GOODS. *A&A*, 579:A2.

[Izquierdo-Villalba et al., 2022] Izquierdo-Villalba, D. et al. (2022). Disc instability and bar formation: a detailed view from the IllustrisTNG. *MNRAS*, 514:1006–1020.

[Karim et al., 2011] Karim, A. et al. (2011). The star formation history of mass-selected galaxies in the COSMOS field. *ApJ*, 730:61.

[Kelkar et al., 2019] Kelkar, K. et al. (2019). The time delay between star formation quenching and morphological transformation of galaxies in clusters: a phase–space view of EDisCS. *MNRAS*, 486:868–884.

[Kennicutt, 1998a] Kennicutt, R. C. J. (1998a). Star formation in galaxies along the hubble sequence. *ARA&A*, 36:189–231.

[Kennicutt, 1998b] Kennicutt, R. C. J. (1998b). The Global Schmidt Law in Star-forming Galaxies. *ApJ*, 498:541–552.

[Kim et al., 2017] Kim, E. et al. (2017). Star Formation Activity of Barred Spiral Galaxies. *ApJ*, 845:93.

[Madau and Dickinson, 2014] Madau, P. and Dickinson, M. (2014). Cosmic Star-Formation History. *ARA&A*, 52:415–486.

[Maeda et al., 2022] Maeda, F. et al. (2022). Statistical Study of the Star Formation Efficiency in Bars: Is Star Formation Suppressed in Gas-Rich Bars?

[Magdis et al., 2012] Magdis, G. E. et al. (2012). The Evolving Interstellar Medium of Star Forming Galaxies Since z=2 as Probed by Their Infrared Spectral Energy Distributions. *ApJ*, 760:6.

[Makarov et al., 2014] Makarov, D. et al. (2014). HyperLEDA. III. The catalogue of extragalactic distances. *A&A*, 570:A13.

[Martig et al., 2009] Martig, M. et al. (2009). Morphological quenching of star formation: making early-type galaxies red. *ApJ*, 707:250–267.

[Masters et al., 2011] Masters, K. L. et al. (2011). Galaxy Zoo: Bars in Disk Galaxies. *MNRAS*, 411:2026–2034.

[Melvin et al., 2014] Melvin, T. et al. (2014). Galaxy Zoo: An independent look at the evolution of the bar fraction over the last eight billion years from HST-COSMOS. *MNRAS*, 438:2882–2897.

[Morrissey et al., 2007] Morrissey, P. et al. (2007). The Calibration and Data Products of GALEX. *ApJS*, 173:682–697.

[Morselli et al., 2020] Morselli, L. et al. (2020). A panchromatic spatially resolved analysis of nearby galaxies – II. The main sequence – gas relation at sub-kpc scale in grand-design spirals. *MNRAS*, 496:4606–4623.

[Nair and Abraham, 2010] Nair, P. B. and Abraham, R. G. (2010). On the fraction of barred galaxies. *ApJL*, 714:L260–L264.

[Nelson et al., 2019] Nelson, D. et al. (2019). The illustristng simulations: public data release. *ComAC*, 6:2.

[Nersesian et al., 2019] Nersesian, A. et al. (2019). Old and young stellar populations in DustPedia galaxies and their role in dust heating. *A&A*, 624:A80.

[Noeske et al., 2007] Noeske, K. et al. (2007). Star Formation in AEGIS Field Galaxies since z = 1.1: The Dominance of Gradually Declining Star Formation, and the Main Sequence of Star-forming Galaxies. *ApJ*, 660:L43–L46.

[Pandey and Sarkar, 2020] Pandey, B. and Sarkar, S. (2020). Exploring galaxy colour in different environments of the cosmic web with SDSS. *MNRAS*, 498:6069–6082.

[Pessa et al., 2022] Pessa, I. et al. (2022). Variations in the $\Sigma_{\rm SFR} - \Sigma_{\rm mol} - \Sigma_{\star}$ plane across galactic environments in PHANGS galaxies. *A&A*, 663:A61.

[Pilbratt et al., 2010] Pilbratt, G. L. et al. (2010). Herschel Space Observatory - An ESA facility for far-infrared and submillimetre astronomy. *A&A*, 518:L1.

[Pillepich et al., 2019] Pillepich, A. et al. (2019). First results from the TNG50 simulation: the evolution of stellar and gaseous discs across cosmic time. *MNRAS*, 490:3196–3233.

[Planck Collaboration et al., 2011] Planck Collaboration et al. (2011). Planck early results. I. The Planck mission. *A&A*, 536:A1.

[Planck Collaboration et al., 2016] Planck Collaboration et al. (2016). Planck 2015 results. XIII. Cosmological parameters. *A&A*, 594:63.

[Popesso et al., 2019] Popesso, P. et al. (2019). The main sequence of star-forming galaxies - I. The local relation and its bending. *MNRAS*, 483:3213–3226.

[Popesso et al., 2022] Popesso, P. et al. (2022). The Main Sequence of star forming galaxies across cosmic times. *MNRAS*.

[Read et al., 2006] Read, J. I. et al. (2006). The tidal stripping of satellites. *MNRAS*, 366:429–437.

[Renzini and Peng, 2015] Renzini, A. and Peng, Y. (2015). An objective definition for the main sequence of star-forming galaxies. *ApJL*, 801:L29.

[Rodighiero et al., 2011] Rodighiero, G. et al. (2011). The lesser role of starbursts for star formation at z=2. *ApJ*, 739:L40.

[Rodighiero et al., 2014] Rodighiero, G. et al. (2014). A multiwavelength consensus on the main sequence of star-forming galaxies at z$\sim$2. *MNRAS*, 443:19–30.

[Rosas-Guevara et al., 2020] Rosas-Guevara, Y. et al. (2020). The buildup of strongly barred galaxies in the TNG100 simulation. *MNRAS*, 491:2547–2564.

[Rosas-Guevara et al., 2022] Rosas-Guevara, Y. et al. (2022). The evolution of the barred galaxy population in the TNG50 simulation. *MNRAS*, stac816.

[Salim and Narayanan, 2020] Salim, S. and Narayanan, D. (2020). The Dust Attenuation Law in Galaxies. *ARA&A*, 58:529–575.

[Schmidt, 1959] Schmidt, M. (1959). The rate of star formation. *ApJ*, 129:243.

[Simmons et al., 2014] Simmons, B. D. et al. (2014). Galaxy Zoo: CANDELS Barred Disks and Bar Fractions. *MNRAS*, 445:3466–3474.

[Skrutskie et al., 2006] Skrutskie, M. F. et al. (2006). The Two Micron All Sky Survey (2MASS). *AJ*, 131:1163.

[Smith and Hayward, 2018] Smith, D. J. B. and Hayward, C. C. (2018). Panchromatic SED modelling of spatially resolved galaxies. *MNRAS*, 476:1705–1725.

[Sparre et al., 2015] Sparre, M. et al. (2015). The star formation main sequence and stellar mass assembly of galaxies in the Illustris simulation. *MNRAS*, 447:3548–3563.

[Spinoso et al., 2016] Spinoso, D. et al. (2016). Bar-driven evolution and quenching of spiral galaxies in cosmological simulations. *MNRAS*, 465:3729–3740.

[Stinson et al., 2006] Stinson, G. et al. (2006). Star formation and feedback in smoothed particle hydrodynamic simulations – I. Isolated galaxies. *MNRAS*, 373:1074–1090.

[Tacchella et al., 2016] Tacchella, S. et al. (2016). The confinement of star-forming galaxies into a main sequence through episodes of gas compaction, depletion and replenishment. *MNRAS*, 457:2790–2813.

[Tacchella et al., 2022] Tacchella, S. et al. (2022). Fast, Slow, Early, Late: Quenching Massive Galaxies at z $\sim$ 0.8. *ApJ*, 926:134.

[Trussler et al., 2020] Trussler, J. et al. (2020). The weak imprint of environment on the stellar populations of galaxies. *MNRAS*, 500:4469–4490.

[Werner et al., 2004] Werner, M. W. et al. (2004). The spitzer space telescope mission. *ApJS*, 154:1–9.

[Woo et al., 2017] Woo, J. et al. (2017). Satellite quenching, Galaxy inner density and the halo environment. *MNRAS*, 464:1077–1094.

[Wright et al., 2010] Wright, E. L. et al. (2010). The Wide-Field Infrared Survey Explorer (WISE): Mission Description And Initial On-Orbit Performance. *AJ*, 140:1868.

[York et al., 2000] York, D. G. et al. (2000). The Sloan Digital Sky Survey: Technical Summary. *AJ*, 120:1579–1587.

[Zhao et al., 2020] Zhao, D. et al. (2020). Barred galaxies in the IllustrisTNG Simulation. *ApJ*, 904:170.

Web resources

[1] HyperLEDA Database for physics of galaxies
http://leda.univ-lyon1.fr
last access 28.11.2022.

[2] The IllustrisTNG project
http://www.tng-project.org
last access 2.12.2022.

[3] The DustPedia Archive
http://dustpedia.astro.noa.gr
last access 28.11.2022.

[4] The James Webb Space Telescope
https://webb.nasa.gov
last access 5.12.2022.